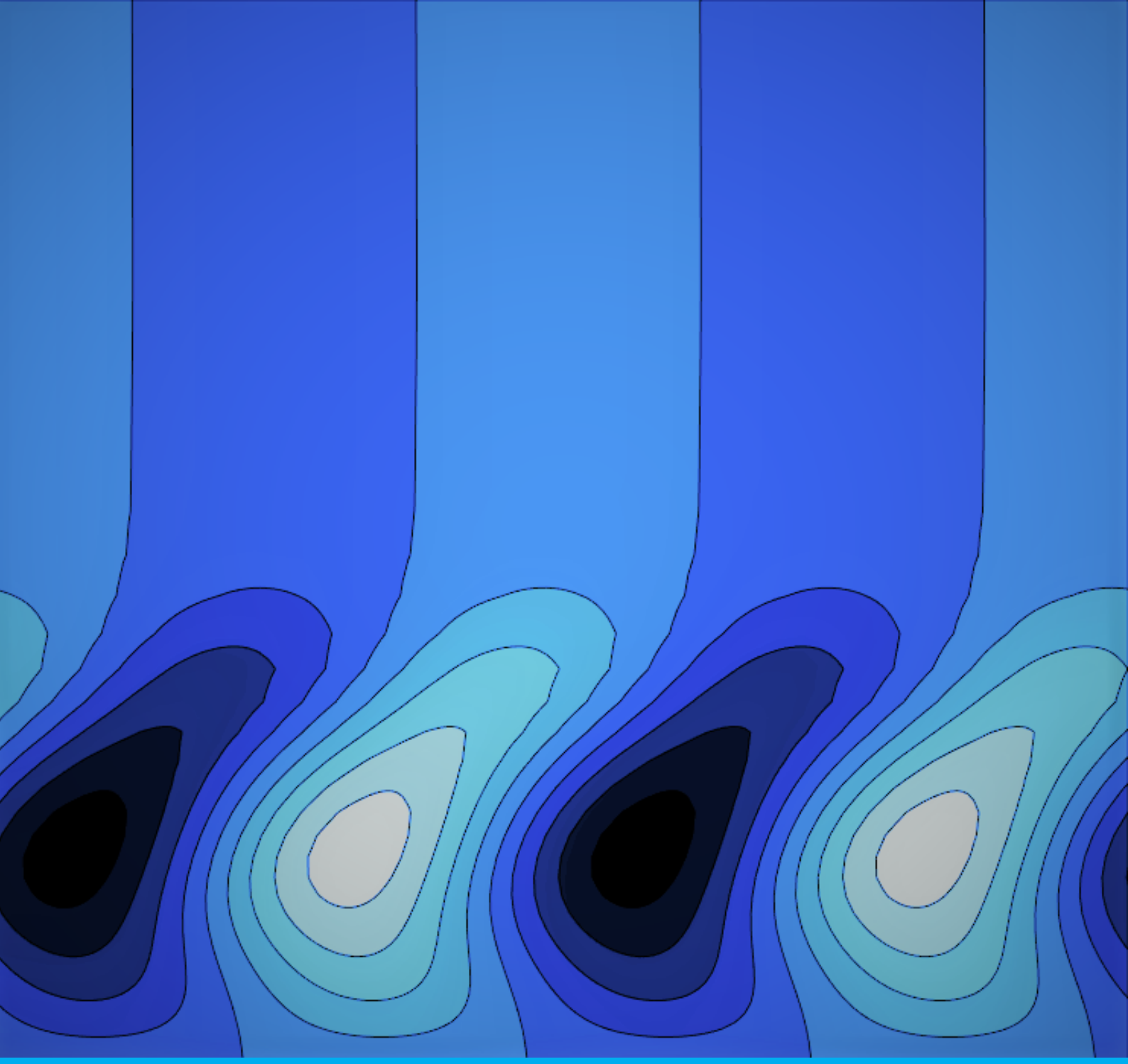

Development of a Nonlinear Parabolized Stability Equation (NPSE) Analysis Tool for Spanwise Invariant Boundary Layers

S.H.J. Westerbeek

Technische Universiteit Delft

TU Delft

Development of a Nonlinear Parabolized Stability Equation (NPSE) Analysis Tool for Spanwise Invariant Boundary Layers

by

S.H.J. Westerbeek

to obtain the degree of Master of Science
at the Delft University of Technology,
to be defended publicly on Thursday January 16, 2020 at 10:00 AM.

Student number:	4350693	
Project duration:	Feb 4, 2019 – January 16, 2020	
Supervisors:	Dr. M. Kotsonis	
	Ir. J. Casacuberta Puig	
Thesis committee:	Dr. M. Kotsonis,	Aerodynamics
	Dr. H.M. Schuttelaars,	Applied Mathematics
	Dr. S.J. Hulshoff,	Aerodynamics
	Ir. J. Casacuberta Puig,	Aerodynamics

TU Delft

Preface

The thesis before you describes the development of a nonlinear stability analysis tool for crossflows at the Delft University of Technology. The research group under Dr. Marios Kotsonis that specializes in flow transition and control contains a numerical department that aims to deliver a transition analysis tool. This thesis contributes to this goal by developing a nonlinear solver to be used in further research and development of laminar airfoils.

This thesis is also a depiction of my development as a person and a researcher as it can be considered my first deep dive into the physics of a specific phenomenon. During this dive, I was given opportunities to follow my instinct and try new solution methods on many occasions, which I consider a blessing. This thesis carries my name first and foremost, however, I have to thank many people without whom its realization would have been impossible.

I would like to thank my supervisors Marios Kotsonis and Jordi Casacuberta Puig for their openness, excitement and their seemingly infinite knowledge of boundary layer transition, stability, and flow control. In addition, I would like to thank Alberto Rius Vidales, Koen Groot and Theo Michelis for the discussions we had concerning boundary layer stability. It is a blessing to be a part of the team and discuss the complicated problems we encounter in stability analyses. It is truly inspiring to see the physics at play in a wind tunnel while working on the code and simultaneously be able to see a DNS simulation of that same flow with incredible detail. I want to thank Marios and Jordi especially for not just helping me in this journey that is the thesis, but also investing time in my personal development as a scientist and supporting my ideas. The time and effort you put in this project is greatly appreciated. I have learned so much over the past year through working with you. The words in this thesis could not possibly comprise all of it. For the first time, I felt like time was moving faster than I wanted it to. Working in this team and on the topic of boundary layer transition has sparked much more excitement in me than I ever thought possible.

On the road to this thesis, I spent many weekends of my first year in the library to study extensively the many books available there. Accompanied by the library boys Sid, Tomàs, Robert and many more. Thank you for making these weekends so much more than just studying. And thank you to the friends I have known for longer than I can remember. Roeland, Jessica, Jeroen, Bart, Dave, Laurens, Bryan, Sicco, Rahul, Jill, Janiek and Inge thank you for all the joy and laughter you bring. I appreciate you so much and I enjoyed clearing our minds through hard work at the gym, a night at the club, a movie night or a relaxing holiday.

I must also thank the coffee ambassadors Joey, Emmy, Boaz and Angelica, and my second family Timara, Arthur, Shané, Logan and Robin who took a complete stranger in for four months during my internship. You are wonderful individuals and every one of you is such a breath of fresh air. Thank you for being you.

Finally, I want to thank Peter, Jacqueline, and Elise, my family who has always supported, cared for and inspired me. My father is the most hardworking man I have ever met and I can only admire his loyalty, dedication, and strength in everything he does. The hard work, positive attitude, witty remarks of my mother are equally inspiring and I could not have wished for better parents. My sister has received the best of both, being strong, determined and intelligent. She should soon be a Bachelor of Science in her own right. Over dinner, they would listen to my findings of phenomena they had hardly any clue existed before I decided to spend a good part of the past year trying to model it. Still, they would, each in their own way, be able to help and support me. Coming home and being able to reset is something I do not take for granted and want to thank you for. It was your support and love that made this project a success. Thank you.

S.H.J. Westerbeek
Delft, January 8, 2020

Summary

The laminar-to-turbulent transition of boundary layers is associated with a significant increase in friction drag. To reduce fuel costs of airliners, a laminar boundary layer over the wing surface is preferred. Laminar airfoil technology shows promising results in delaying the laminar-turbulent transition in order to reduce the friction drag of wings. With this technology, the instabilities present in the boundary layer are manipulated to delay or prevent transition. For further research into flow control, a computationally efficient method is required that allows for the prediction of nonlinear growth of perturbations in swept wing boundary layers. For this purpose, a nonlinear stability analysis tool was developed and improved in this thesis.

The nonlinear evolution of stationary crossflow instabilities was simulated using the Nonlinear Parabolized Stability Equations (NPSE). The NPSE, due to their accumulative nature, are sensitive to minor changes in base flow variations, boundary conditions and initial conditions. This thesis therefore also investigated the importance of primary and forced mode introduction. In this investigation, several different introduction methods were examined in addition to a newly introduced method that accounts for the history of a forced mode through a first-order backward derivative of its amplitude while neglecting a possible change in shape function which is of a significantly smaller order.

An NPSE solver was set up and its application was validated through the simulation of Tollmien-Schlichting waves in a flat plate Blasius boundary layer. The literature shows two different results for this case. Both cases could be matched closely by varying the primary mode introduction method with either Orr-Sommerfeld or Weakly Nonparallel Local (WNL) stability techniques. Both cases were validated in their respective literature with a Direct Numerical Simulation (DNS) which are hypothesized to be initiated using the same initial condition as the NPSE; hence, both studies were able to match their DNS results. From this study, the sensitivity of the NPSE to the primary mode introduction was found to be caused by the duality of eigenvalues resulting from the direct solution of the WNL stability problem. Although results closely match the ILST simulation, the initially stable state of the primary mode following WNL initial conditions results in a lower amplitude of forced modes. This reduces the strength of nonlinear forcing downstream of the inflow. The initially stable state is hypothesized to be the cause of this mismatch.

The new forced mode introduction method that is presented for nonlinear mode introductions using an Inhomogeneous Linear Parabolized Stability Equation (ILPSE) solver was applied to both cases using different assumptions for the amplitude at the stage prior to introduction. This method accounts for nonparallel effects of the base flow, nonlinear forcing and amplitude growth for a newly forced mode. A reduction of initial transients can be seen as a result, which is indicative of physical introduction. For the cases examined in this thesis, however, this introduction always resulted in lower amplitudes of all harmonics introduced through this method downstream of their introduction compared to modes initiated with an assumed zero amplitude at the introduction, as is often presented in the literature. Far downstream results with the newly introduced mode show more transient behaviour as nonlinear interactions strengthen which is hypothesized to be a delayed effect of this introduction.

The NPSE tool was able to simulate the linear and nonlinear growth of crossflow and Tollmien-Schlichting instabilities in a spanwise invariant crossflow or Blasius boundary layer respectively. For very small perturbation amplitudes, the results match with the LPSE. As the amplitudes of all harmonics in the system grow, a deviation from the linear result, due to increased nonlinear interactions, can be seen. The nonlinear interactions lead to nonlinear saturation of all modes in the system. The results were tested to have converged in streamwise and wall-normal direction and the importance of including higher harmonics for the convergence of the primary mode was investigated and proven.

A DNS comparison was performed that confirmed the accuracy of the NPSE in the prediction of stationary crossflow instabilities until the far nonlinear regime. It cannot be said with certainty whether the mismatch near the end of the domain was a result of harmonic convergence, grid convergence or that it is a delayed

effect of initial conditions. The difference in amplitude of the second harmonic shortly after its introduction is hypothesized to be caused by the fact that the DNS is elliptical and can correct for an introduction error in time. The NPSE can only correct for the error while marching. The forced mode introduction presented in this thesis proved accurate as higher harmonics were generated in the NPSE simulation at an amplitude and growth rate that matches the DNS. A minor mismatch of the forced mode introduction amplitude of the third harmonic is caused by an overestimation of the second harmonic's amplitude at that location.

A second DNS was performed to validate the new technique at the inflow. The introduction of the second harmonic was imposed at the inflow of the DNS following NPSE calculations. The presence of the third harmonic affects the second harmonic which results in an initial transient in the DNS. The more stable introduction in the NPSE results in very different amplitudes downstream, while the DNS matches the simulation in which only the primary mode was introduced due to its elliptic nature. The lack of an overshoot in the second harmonic for this case resulted in lower amplitudes and more transient behaviour far downstream in the NPSE. It is hypothesized that the overshoot for the second harmonic allows it to converge to the correct relative amplitude. This gives more accurate results sufficiently far from this inflow despite initial errors. Higher harmonics can be introduced accurately using the new technique, although further experimental and numerical research is required into the generation of physical initial conditions.

Nomenclature

Abbreviations

BL	Boundary Layer
CF	Crossflow
CFD	Computational Fluid Dynamics
CFI	Crossflow Instability
DNS	Direct Numerical Simulation
$ILPSE$	Inhomogeneous Linear Parabolized Stability Equations
$LPSE$	Linear Parabolized Stability Equations
$NPSE$	Nonlinear Parabolized Stability Equations
OS	Orr-Sommerfeld
PSE	Parabolized Stability Equations
TS	Tollmien-Schlichting

Markers

$*$	Integration variable
$-$	Nondimensional quantity
0	Value at the inflow plane
$\dagger$	Complex conjugate
$\prime$	Perturbation
$\wedge$	Shape function
e	Freestream value
i	Stage indicator

Number Sets

$\mathbb{C}$	Complex Numbers
$\mathbb{R}$	Real Numbers

Other Symbols

α	Streamwise wavenumber
β	Spanwise wavenumber
δ	Blasius length scale
∇	Vector differential operator
ν	Kinematic viscosity

Ω	Truncated spectral domain
ω	Angular frequency
ρ	Density
$\vec{q}$	Total velocity vector
A	Amplitude
F	Nondimensional frequency
L	Total number of modes
l, m, n, g, j, h, k	Mode counters
M	Spectral domain in z
M	Spectral truncation in z
m	Harmonic counter in x
N	N-factor
N	Spectral domain in x
N	Spectral truncation in x
n	Harmonic counter in x
t	time
U	Base flow velocity in x
u	Total velocity in x
u'	Perturbation velocity in x
V	Base flow velocity in y
v	Total velocity in y
v'	Perturbation velocity in y
W	Base flow velocity in z
w	Total velocity in z
w'	Perturbation velocity in z
x	Leading edge orthogonal axis
y	Wall-normal axis
z	Spanwise axis

Contents

1 Introduction

1.1. Historical background

Osborne Reynolds' paper "An Experimental Investigation of the Circumstances which Determine whether the Motion of Water shall be Direct or Sinuous, and of the Law of Resistance in Parallel Channels." in 1883 initiated the interest in laminar-turbulent transition of flows that is still ongoing today. Reynolds, performing an experiment where the flow of fluids through tubes was analyzed, reasoned that four factors influence the nature of a flow: the velocity, U_t, density, ρ, viscosity, μ, and a characteristic length, e.g., the tube radius c_t. Combining these factors to arrive at the dimensions of the critical velocity where turbulence is first observed, allows a division of the factors to define a dimensionless number known nowadays as the Reynolds number, $Re = \frac{c_t \rho U_t}{\mu}$. This number is the ratio of inertial and viscous forces. Reynolds showed that, for different tube diameters, this number was always approximately the same when laminar-turbulent transition was detected, indicating that this number correctly characterizes the state of the flow [47].

Theoretical work in fluid mechanics had long neglected viscosity effects in the theory. The discrepancy found between theory and reality was likely caused by this even though technically important fluids, e.g. water and air, had small viscosity [40]. Ludwig Prandtl introduced the concept of the viscous boundary layer as presented in his paper in 1904. He showed that two flow regions exist when considering the flow past a body. A thin region close to the body, where viscous effects are important, and the region outside this layer where the effect of viscosity can be neglected [40]. Realizing that it was unfeasible to describe the phenomenon of the boundary layer with the full Navier-Stokes equations, he simplified the equations after an order of magnitude analysis [22]. This lead to much simpler equations that describe the behaviour of fluid flow in the boundary layer.

Laminar transition of boundary layers is the process through which a laminar boundary layer evolves toward a turbulent one, as shown by Prandtl in 1914 by considering the flow about a sphere. Transition prediction is important for the design of hydrodynamic and aerodynamic bodies as the aforementioned boundary layer states greatly affect their respective hydrodynamic or aerodynamic performance. Predicting transition, however, is not yet fully understood and requires combined physical and mathematical insight. Stability analysis forms the basis for theoretical and numerical prediction of transition.

In 1907 and 1908 respectively, William McFadden Orr and Arnold Sommerfeld independently studied and found an eigenvalue equation describing the local stability of disturbances in boundary layers. The later named Orr-Sommerfeld (OS) equation, starts from the Navier-Stokes equations and assumes a known parallel base flow on which infinitesimal disturbances are superimposed. The local evolution of any disturbance imposed on this flow can be described by the OS equation where the eigenvalue and eigenfunction represent the linear growth rate and shape of said disturbance.

Neglecting flow nonparallelism in the OS-equation introduces limitations to the model. The neglected streamwise derivatives were not of smaller order than some terms still present in the equation, see Herbert [15]. Bertolotti et al.[4] improved the method by maintaining the nonparallelism of the flow, leading to the Linear

Parabolized Stability Equations (LPSE) and Nonlinear Parabolized Stability Equations (NPSE). These equations were not eigenproblems and required a marching solution algorithm, using a local OS solution as initial condition, which could be performed after the parabolization of the equations. This process neglects downstream influence after an order of magnitude analysis of the second-order streamwise derivatives. Although both equations have similar solution algorithms, the nonlinear terms present in the NPSE significantly complicate the required steps to find a solution. The NPSE forms the main topic of this thesis.

Bertolotti et al. [4] used an NPSE approach to predict the growth of Tollmien-Schlichting instabilities in a Blasius boundary layer. Chang et al. [8] performed the same case and did not match the results from Bertolotti et al. Herbert mentions the amplitude found by Chang et al. is greater and that matching is difficult due to the sensitivity of the NPSE [16]. Since the base flow for this case, a Blasius boundary layer, is well-defined. The differences are hypothesized to be in the initial condition for either or both the primary mode and forced mode introduction. Therefore, aside from being a reference, this case will also serve as an investigation into the importance of introduction techniques. A new technique will be introduced that increases the physical accuracy of mode introduction by accounting correctly for mode history, nonparallel and nonlinear effects.

In this thesis, additionally, swept-wing boundary layers are considered that give rise to a very different base flow topology than that found on a flat plate aligned with the flow. A crossflow boundary layer features a crossflow component, orthogonal to the external streamline that gives rise to crossflow instabilities. This will be explained in more detail in section 2.1.1. The favorable pressure gradient that is stabilizing for streamwise instabilities has the opposite effect on the crossflow instabilities [38]. On laminar airfoils, following the leading edge of a swept wing, a crossflow with a favorable pressure gradient is found in which crossflow instabilities (CFI's) can grow and cause transition.

The simulation of stationary crossflow vortices was first performed by Paredes et al. in [34] and traditional PSE results were matched, although no comparison with DNS or experiments was done. In addition, strong transients can be found in the results around harmonic introductions. Haynes and Reed [14], in their nonlinear crossflow simulation, compared to experimental results and accounted for geometry curvature. Haynes attempted to reduce the uncertainty in the initial condition of forced modes through an iterative scheme. Starting the simulations upstream and match the primary mode amplitude at some point downstream. In this thesis the spanwise invariant NPSE are used to predict the growth of TS waves and stationary CFI's and an investigation into correct mode introductions is performed to increase the accuracy of NPSE simulations. DNS simulations also suffer from mode introduction techniques, although no mention of this is found in the literature. Results are compared with DNS for different initial conditions for both simulation techniques.

1.2. Motivation

Substantial improvements in economy and ecology of air travel can be provided by laminar flow technology [36]. However, despite great efforts in increasing the computational speed and efficiency of modern computers, the costs of running a full-scale Direct Numerical Simulation (DNS) are very often still unfeasible for engineering purposes. As a result, contemporary research has set its sights on computationally efficient methods to predict flow stability and transition. Such computationally efficient methods often neglect lower-order interactions or flow aspects that would significantly increase their computational costs. Depending on the flow transition scenario, some interactions cannot be neglected. Nonlinear interactions between perturbations play a non-negligible role in the evolution of stationary crossflow vortices, as shown experimentally by Dagenhart et al. [44], present in swept wings under low freestream turbulence intensities [14]. Riedel and Sitzmann [36] measured the turbulence intensities for the still air atmosphere in flight-conditions which proved to be less than 0.05%. Stationary crossflow instabilities (CFI) therefore dominate the transition scenario in airliners. To correctly predict the growth of the aforementioned, a method that accounts for nonlinear interactions must be exploited. The evolution of stationary crossflow will therefore be simulated using an NPSE approach as perturbations in a nonlinear setting are coupled through wave-triad interactions [41].

A nonlinear stability analysis tool must be developed that is capable of simulating perturbations in a crossflow setting since such a code is not widely available. The three-dimensional spanwise invariant Nonlinear Parabolized Stability Equations (NPSE) are able to do this. Haynes and Reed [14] performed an NPSE simulation of swept-wing vortices using an NPSE approach and compared with experimental results to validate

its application. The use of the NPSE, both in crossflow specifically and otherwise, is not as common in the industry due to its sensitivity to the numerical description of the flow. The NPSE is known to be sensitive to small changes in flow topology, pressure gradient, initial condition and harmonics present in the system [8, 14, 16]. Haynes aimed to solve the initial condition sensitivity by starting the simulation upstream and matching the mode amplitude at an arbitrary point downstream of the actual NPSE simulation in the linear regime. This takes an average of three iterations [14]. It is uncertain how accurate this method is downstream of the inflow, however, as higher harmonics could still contain errors in this initial condition estimation.

In addition to providing a set reference crossflow test case, proving convergence of the results and disclosing the contents of an NPSE solver down to coding level, we will also set out to show the effect of initial condition and nonlinear nonparallel forced mode introductions. This thesis will introduce a new method for nonlinear forced mode introduction to increase the accuracy of NPSE simulations.

Proving the application and accuracy of the NPSE framework for the prediction of nonlinear growth of CFI's can aid in further research on transition in swept-wing boundary layers. In addition, the NPSE could prove to be the next industry standard in swept-wing transition prediction. Reducing the inaccuracy of mode introductions ensures that the NPSE are a trustworthy and unique tool for nonlinear transition prediction.

1.3. Research questions and objectives

An NPSE solver is not widely available. This research aims to develop a solver in Matlab and disclose the difficulties in designing such a tool. Secondly, the research focuses on improving its accuracy before applying it to spanwise invariant boundary layers. The development of the solver and validating its application to spanwise invariant boundary layers are the primary goal of this thesis. The research question, therefore, is:

"Are the Nonlinear Parabolized Stability Equations (NPSE) suitable to model the nonlinear evolution of stationary crossflow instabilities in a swept flat plate boundary layer?".

To improve on the state-of-the-art of NPSE solvers, the second research question reads:

"What changes can be made to the NPSE solution algorithm to improve its accuracy?".

The sub-questions to be able to answer the main research questions are:

1. What is a feasible high-level and low-level architecture of an NPSE solver?
2. How can a filter be used to compare against an unrepresented mode's amplitude to determine its significance for computations?
3. How can the initial condition be generated for the primary mode and what is its effect on the amplitude evolution?
4. How can nonlinearly generated modes be introduced while accounting for nonparallel and nonlinear effects and what is its effect downstream of the introduction?
5. Do the results of the NPSE solver compare to DNS results and what is the cause of possible discrepancies between the two?

In this set, the first three sub-questions relate to the development of the tool. Questions four and five concern the validation and improvement on the state-of-the-art.

The thesis will provide a high-level architecture of the NPSE solver and a detailed explanation of its contents. In addition, this thesis will bring forth improvements to the numerical introduction of modes in the system and validate the use of the NPSE framework in crossflow by comparing the results with a DNS simulation.

1.4. Outline

The thesis commences by providing the reader with the required literature on boundary layers, boundary layer stability and transition in section 2. The equations that govern this stability are tackled in section 3.

The equations that can describe the evolution of instabilities in the boundary layer are then used to design a solution algorithm. The development of the solver is explained in section 4 and considers both coding of the solver and discretization of the NPSE. A problem description is provided in section 5 that describes the flat plate case that will be used to validate the NPSE by simulating the evolution of a Tollmien-Schlichting (TS) wave. The boundary conditions for the crossflow case on which the code will be applied and validated is also presented here. Results from the aforementioned cases are presented and analyzed in section 6. This section also contains a convergence study of the NPSE in the crossflow setting and a study into different initial conditions for primary and forced mode introductions. Closing the section, is a summary of some importance numerical developments that aim to increase the accuracy of the NPSE. They are discussed in more detail and compared to results without these additions. Section 7 concludes the thesis by considering the application of the NPSE for nonlinear prediction of stationary crossflow instability growth and the an evaluation of mode introduction techniques. The conclusions are followed by recommendations for future work.

2

Boundary layer flow and transition

This chapter tackles the properties of laminar and turbulent boundary layers as well as the laminar-turbulent transition by which a laminar boundary evolves toward a turbulent chaotic state. The concepts of crossflow, base flow and boundary layer stability are introduced.

2.1. Boundary layers

The Boundary Layer (BL) is described as the region of a flow close to a solid surface dominated by viscous forces. This flow region develops when a relative velocity exists between the surface and the fluid. The boundary layer arises due to the no-slip condition at the wall as a result of friction as locally, fluid particles are retarded by its effects. A change in streamwise velocity can be found in the wall-normal direction, y, where the streamwise velocity u goes from zero at the wall to the freestream value. We define the velocity profile, $u(y)$, as the variation of velocity with the wall-normal coordinate in a two-dimensional case.

Where the boundary layer stops and the freestream begins is hard to define as the velocity in the boundary layer asymptotically approaches the freestream value. The boundary layer thickness is therefore often defined as the distance from the wall at which the local velocity equals 99% of the freestream value. The boundary layer develops continuously with the streamwise coordinate x [35].

The wall shear stress is proportional to the velocity gradient at the wall, i.e.,

$$\tau_{wall} = \mu \left(\frac{\partial u}{\partial y} \right)_{y=0}, \tag{2.1}$$

where τ is the shear stress, μ the dynamic viscosity and $\left(\frac{\partial u}{\partial y} \right)_{y=0}$ is the velocity gradient at the wall. In equation 2.1, the term $\frac{\partial v}{\partial x}$ is ignored as it is of two orders smaller than the streamwise velocity gradient in wall-normal direction [46]. The surface integration of the shear stress presents the friction drag.

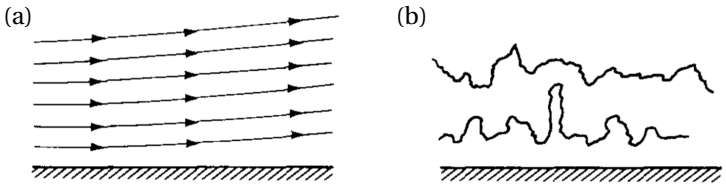

Figure 2.1: Illustration of particle paths in a laminar flow (a) and a turbulent flow (b). Reproduced from Anderson [1].

For a certain dynamic viscosity μ, the boundary layer velocity profile thus determines the friction drag of a body, e.g. a wing. In order to reduce the friction drag, low-momentum particles should thus not be replaced by high-momentum ones as this would increase the velocity gradient at the wall. Laminar flow is smooth and

regular, whereas a turbulent boundary layers feature irregular and chaotic motion [1] as shown in the figures 2.1(a,b) respectively. The chaotic motion found in turbulent boundary layers results in the displacement of particles commonly referred to as mixing. In order to minimize friction drag, a laminar boundary layer is preferred.

A boundary layer that is laminar, is not guaranteed to stay laminar indefinitely. A laminar-turbulent transition can occur via which a smooth laminar boundary layer becomes a chaotic, turbulent one. The process of transition will be examined closer in section 2.4. Predicting the location at which the flow becomes turbulent is the main topic of this thesis.

2.1.1. Crossflow

Crossflow arises, among other places, in swept-wing boundary layers. A jet in a transverse flow is also considered a crossflow, although in this thesis, crossflow will refer to the crossflow boundary layer. Saric et al. [39] state that the inviscid region outside the BL curves through the effect of sweep and pressure gradient. In the boundary layer, however, velocity is reduced while pressure is unchanged and this imbalance gives rise to a secondary flow called crossflow. Through this definition, we know that its contribution must fade in the freestream and, given the no-slip boundary condition at the wall, the velocity profile must contain an inflection point. The presence of an inflection point is clearly visible if the boundary layer is projected onto a coordinate system aligned with the external flow as depicted in figure 2.2.

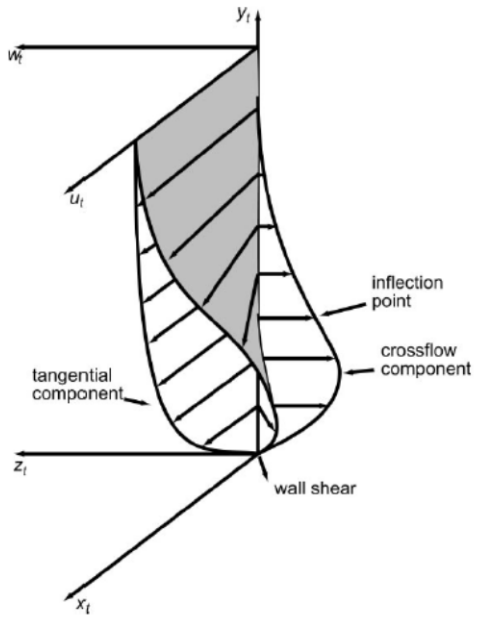

Figure 2.2: Illustration of crossflow velocity components. Reproduced from Serpieri [43].

In this thesis, we will not consider the effects of curvature as is present around wings. Instead the evolution of crossflow instabilities is evaluated on swept flat plates that feature a favorable pressure gradient in the direction orthogonal to its leading edge. The plate is swept, meaning that this leading edge orthogonal direction is angled with respect to the external flow. The aforementioned pressure gradient results in a crossflow boundary layer as presented in figure 2.2.

2.2. Receptivity

Although out of the scope of this thesis, a key element of the transition process is the ability of free-stream disturbances to excite infinitesimal instability waves in a process called receptivity [10, 25]. Through this process, the instabilities are first presented in the flow. Receptivity describes the process by which instability waves are generated through the interaction of external disturbances with local irregularities or the leading edge [20]. These local irregularities might be the result of small roughness discontinuities or joints required to create a surface or plate [9]. The linearized NS equations describe the receptivity problem as a hydrodynamic resonator system, subject to external forces [6]. Figure 2.3 illustrates sources of external disturbances, possible types of instabilities generated as a result and important parameters that complicate the modelling of this problem.

The initial energy and the nature of the instabilities presented in the boundary layer is determined by external factors. In crossflows with low-turbulence freestream conditions, stationary waves dominate, while the transition scenario is dominated by traveling waves dominate in high-turbulence environments [5]. Low-

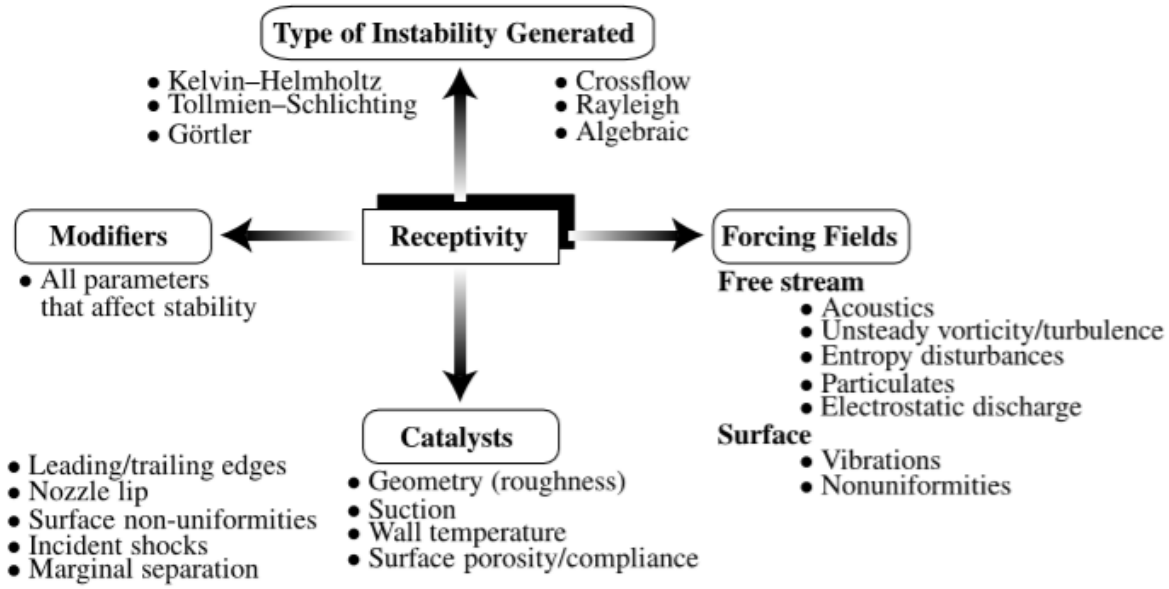

Figure 2.3: Modern view of the receptivity problem [6].

turbulence environments are found on free-flight conditions and thus the growth stationary waves are most relevant to this research.

The stability analysis methods considered in this thesis omit the receptivity problem and model the growth of a perturbation starting from a location downstream of the receptivity region.

2.3. Stability and stability modes

Hydrodynamic stability is concerned with a state's response to a disturbance [41], i.e. the ability or inability of a state to recover from said disturbance. We will follow White [46] and explain the stability of boundary layers through the analogy of a ball initially at rest on various surfaces. Four stability states are depicted in figure 2.4.

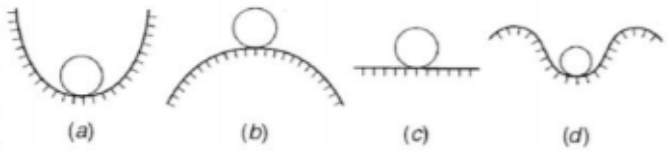

Figure 2.4: Stability analogy as explained in White [46], with (a) stable, (b) unstable, (c) neutral stability, (d) conditional stability.

The ball is at rest in all of the cases presented in figure 2.4. This resting state is considered to be the laminar boundary layer. The ball and corresponding boundary layer are stable if they return to their original state after a disturbance. A disturbance that grows can cause a boundary layer to transition into a different state. This flow is then considered unstable [41]. In 2.4(a), a disturbance will decay over time and the ball will end up at the same location. This situation is therefore stable. In 2.4(b), the ball will roll off the hill after a disturbance, i.e. the disturbance grows. In 2.4(c), the perturbation neither grows nor decays. The ball ends up in a new, perturbed, stable state and the corresponding boundary layer would be neutrally stable to this disturbance. In nonlinear stability frameworks, the energy can affect the stability state. This is represented in figure 2.4(d), where small disturbances decay. However, when a certain energy threshold is met, the response of the boundary layer might be unstable.

Although, formally, the state refers to the stability of the boundary layer, the perturbations in the flow are initially the subject of the analysis. The boundary layer serves as the base flow, i.e. the steady laminar solution to

the problem. Eventually, the boundary layer state can be modified through the nonlinear interaction of finite amplitude modes, justifying the reference to boundary layer stability. The (linear) stability of a base flow can be represented in a stability diagram. This diagram shows the states of a range of perturbation frequencies whose amplitudes are assumed infinitesimal over a range of locations of that base flow. The stability state of a mode propagating through a base flow can be either damped, neutral or amplified [27]. A stable mode is damped, a neutral mode does neither grow nor decay and an unstable mode grows. This stability is pointwise numerically calculated and must be integrated to see the evolution of a perturbation. A mode that is stable at one point in the flow, might be unstable later and vice versa.

Whether a mode is damped, neutral or amplified depends in a linear case on the Reynolds number, the base flow velocity profile and the specifications of the mode whose stability is to be evaluated. In a global approach the Reynolds number can be defined as

$$Re_0 = \frac{\delta_0 U_0}{\nu}, \tag{2.2}$$

with δ_0 the Blasius length at the start of the domain, U_0 the external velocity at the start of the domain and ν the kinematic viscosity of the fluid. A local Reynolds number can also be used that uses the local Blasius length δ_x instead of the inflow value. This local Reynolds number, denoted Re, is therefore dependent on the streamwise coordinate and is used for plotting purposes in this thesis. For low Re, close to the leading edge, a boundary layer is stable and all instability waves are damped [12] until a particular streamwise location denoted by Re_{crit}. From this point on, some perturbations might, instead, be unstable and grow. This growth rate is not uniform among all frequencies or locations. The growth rate corresponding to a certain frequency at a location x, can be found through stability analysis. The result of spatial stability analysis methods is the complex wavenumber $\alpha \in \mathbf{C}$ whose imaginary part describes the local growth of a perturbation.

Stability analysis does not predict the onset of turbulence. The breakdown of a laminar boundary layer through the amplification of modes leads to a sequence of events that result in turbulence [46]. It is the amplification of the superimposed disturbances that we are able to analyze through stability analyses.

2.3.1. Tollmien-Schlichting instabilities

Tollmien-Schlichting (TS) waves are viscous instabilities that were initially hypothesized to be purely two-dimensional [46] after the existence of TS waves and their role in the transition process was experimentally observed for the first time by Schubauer & Skramstad [42] and Liepmann [24]. Liepmann, however, noted spanwise fluctuations that were initially ignored. Klebanoff et al. [21] finally pointed out that there are three stages of development in the evolution of TS waves. The primary stage, where the instabilities are purely two-dimensional and linear, a second stage where finite amplitude perturbations are present and nonlinear behaviour is observed and lastly the birth of turbulent spots. For the first stage, a two-dimensional linear stability framework can thus accurately describe the growth of TS waves. In this linear framework, instabilities do not show any significant interaction and the TS waves remain two-dimensional.

The transition process dominated by TS waves as seen in experiments is illustrated in figure 2.5. The three-dimensionality found in stage three is the result of secondary instabilities [40]. Although secondary instabilities can be modeled via the nonlinear parabolized stability equations, they are out of the scope of this thesis and will not be examined further.

2.3.2. Crossflow instabilities

In three-dimensional flows with a favourable pressure gradient, crossflow instabilities may dominate the transition scenario instead of Tollmien-Schlichting waves. The aforementioned crossflow instabilities feature co-rotating vortices aligned with the streamwise coordinate [43]. In crossflow boundary layers, TS waves can remain the dominant mode for transition until sweep angles of 25-30°are reached. From there onward, crossflow instabilities dominate the transition scenario according to Criminale et al. [9].

Bippes [5] states: "Since crossflow instability is an inflectional instability, it is highly amplified and can occur at very low Reynolds numbers." and that it may lead to transition very close to the leading edge. The flow topology, as explained in section 2.1.1, features an inflection point in the crossflow component that gives rise to these highly amplified crossflow instabilities. The CFI's are aligned with the local streamwise direction and displace the local velocity via a sweeping motion. Low-momentum flow, that originally resides close to the

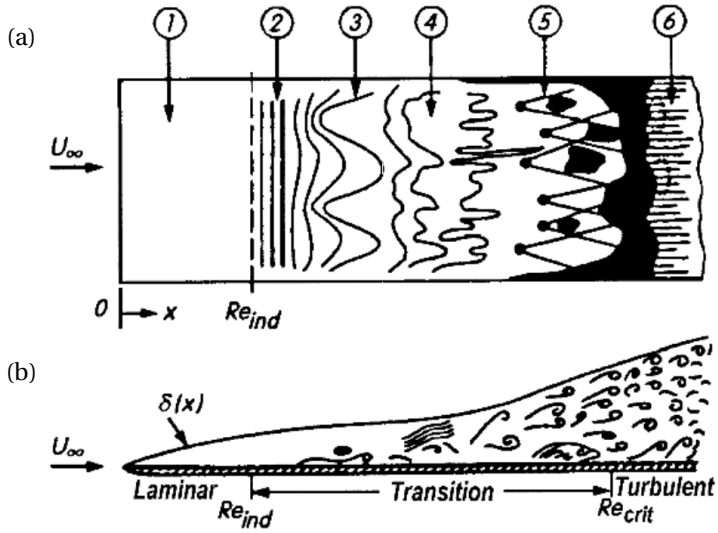

Figure 2.5: Illustration of TS wave dominated transition in a flat plate boundary layer from [40] showing a top view (a) and side view (b) featuring (1) stable laminar flow, (2) unstable TS waves, (3) three-dimensional waves and vortex formation, (4) decay, (5) formation of turbulent spots and (6) fully turbulent flow.

wall, is swept up. Simultaneously, high-momentum flow is swept down into the boundary layer. The result is a modified boundary layer in which strong shears are present where secondary instabilities are unstable [43].

2.4. Transition

Transition is the process by which a laminar boundary layer evolves toward a chaotic turbulent state. Figure 2.6 summarizes possible transition paths from the forcing of instabilities to the growth and interactions of perturbations to three-dimensional breakdown and eventually turbulence. This thesis concerns the modelling of primary instability growth accounting for nonlinear effects. Following figure 2.6, we see that primary instabilities alone do not cause transition to turbulence directly. The growth of secondary instabilities and three-dimensional breakdown eventually lead to turbulence. The stability methods in this thesis will not be used to model secondary instabilities or breakdown. Instead, the nonlinear primary growth of instabilities is correlated to this breakdown via the e^N method as indicated by the red arrow in figure 2.6.

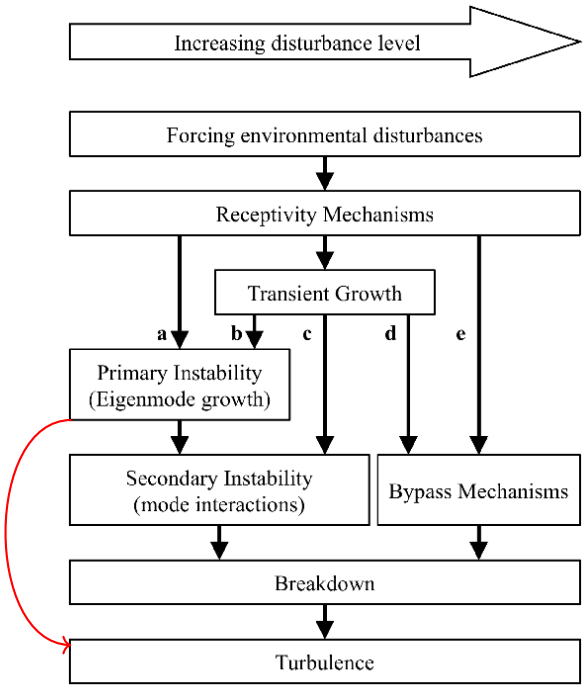

Figure 2.6: Possible transition paths where the red arrow depicts transition prediction based on solely eigenmode growth. Adjusted from [29].

Groot [12] explains how the correlation to transition via only primary mode growth can be used to predict transition nonetheless. He states: "The underlying assumption is that the nonlinear mechanisms set in at an explosive rate, causing the breakdown to turbulence to occur in a relatively small spatial region as opposed to the development of the primary instability." Therefore the

linear methods suffice for predicting this transition. However, nonlinear methods would be more precise in doing so.

2.4.1. e^N method

The e^N method as described by van Ingen [18] is a correlation method to predict transition based on the amplification factor N. This factor follows from the model of exponentially growing eigenmodes, as will be explained in section 3.2.1, and is defined as

$$N = \ln\left(\frac{A}{A_0}\right), \tag{2.3}$$

where A and A_0 are the amplitudes at the location of evaluation and the start of the domain respectively. In this thesis, the amplitude is chosen as the peak absolute streamwise velocity perturbation $|u'|_{max}$. Calculating this N-factor for a range of perturbation frequencies and then evaluating the maximum $N-$factor at every location, provides an N envelope curve that can be correlated to a transition criterion. The value of this criterion is determined through experiments on similar flows. The accuracy of this criterion and the subsequent transition prediction thus relies on the similarity of the flow that was examined in the wind tunnel to that of the simulation. The exact value of the criterion has to be calibrated for every new case [18].

The theory of N-factor growth transition prediction is as strong as the method used to calculate the N-factor. It appears the method, however, contains enough physics to predict the distance to transition accurately [18]. The correlation method relies on the fact that the receptivity problem in a flow is similar. Stability analysis is then used to calculate only the growth rate of the instability waves in the flow subjected to different pressure gradients. The calibration can therefore be seen as a model for the receptivity problem. The use of a nonlinear stability framework would improve the prediction of growth as nonlinear growth can also be accounted for.

3

Governing equations

This chapter concerns the mathematical description of the stability of boundary layers. Different forms of the stability equations are explained and derived through perturbation analysis starting from the Navier-Stokes equations.

3.1. Navier-Stokes equations

The governing equations for a general viscous flow that follow from the application of Newton's second law are given in the Navier-Stokes (NS) equations [1]. By neglecting temperature and compressibility effects the equations reduce to a simpler form that is relevant to boundary layer physics in low-speed aerodynamics. In dimensional form, these equations are

$$\nabla \cdot \vec{q} = 0, \tag{3.1a}$$

$$\rho \frac{\partial \vec{q}}{\partial t} + \rho(\vec{q} \cdot \nabla)\vec{q} = -\nabla p + \mu \nabla^2 \vec{q}, \tag{3.1b}$$

where $\vec{q}$ is the velocity vector $(u, v, w)^T$ containing velocities in streamwise coordinate, x, wall-normal coordinate, y, and spanwise coordinate, z, respectively, t is the time and p is the static pressure. The nabla operator, ∇, in three-dimensional flow is defined as $(\frac{\partial}{\partial x}, \frac{\partial}{\partial y}, \frac{\partial}{\partial z})^T$.

3.2. Perturbation analysis

Perturbation analysis is a method through which the development of disturbances can be described mathematically. A perturbation needs to have a reference flow through which it travels [12]. This reference flow, referred to as the base flow, is the steady laminar solution to the NS equation denoted $\vec{Q}$. The instantaneous flow field is decomposed into the base flow, $\vec{Q}$, and perturbations, $\vec{q}'$, as

$$\vec{q}(x, y, z, t) = \vec{Q}(x, y, z) + \vec{q}'(x, y, z, t). \tag{3.2}$$

Note that the base flow solution is independent of time. Equation 3.2 expressed in vector coordinates x, y and z reads

$$\vec{q} = \begin{bmatrix} u(x, y, z, t) \\ v(x, y, z, t) \\ w(x, y, z, t) \end{bmatrix} = \begin{bmatrix} U(x, y, z) \\ V(x, y, z) \\ W(x, y, z) \end{bmatrix} + \begin{bmatrix} u'(x, y, z, t) \\ v'(x, y, z, t) \\ w'(x, y, z, t) \end{bmatrix}. \tag{3.3}$$

An identical decomposition is performed with regard to the pressure:

$$p(x, y, z, t) = P(x, y, z) + p'(x, y, z, t). \tag{3.4}$$

3.2.1. Stability equations

The stability equations can be used to describe the temporal or spatial evolution of perturbations in a fluid system. Expanding the Navier-Stokes equations, eqs. 3.1, to the momentum equations in x, y and z yields:

$$\frac{\partial u}{\partial x}+\frac{\partial v}{\partial y}+\frac{\partial w}{\partial z}=0, \tag{3.5a}$$

$$\rho\left[\frac{\partial u}{\partial t}+u\frac{\partial u}{\partial x}+v\frac{\partial u}{\partial y}+w\frac{\partial u}{\partial z}\right]=-\frac{\partial p}{\partial x}+\mu\left(\frac{\partial^2 u}{\partial x^2}+\frac{\partial^2 u}{\partial y^2}+\frac{\partial^2 u}{\partial z^2}\right), \tag{3.5b}$$

$$\rho\left[\frac{\partial v}{\partial t}+u\frac{\partial v}{\partial x}+v\frac{\partial v}{\partial y}+w\frac{\partial v}{\partial z}\right]=-\frac{\partial p}{\partial y}+\mu\left(\frac{\partial^2 v}{\partial x^2}+\frac{\partial^2 v}{\partial y^2}+\frac{\partial^2 v}{\partial z^2}\right), \tag{3.5c}$$

$$\rho\left[\frac{\partial w}{\partial t}+u\frac{\partial w}{\partial x}+v\frac{\partial w}{\partial y}+w\frac{\partial w}{\partial z}\right]=-\frac{\partial p}{\partial z}+\mu\left(\frac{\partial^2 w}{\partial x^2}+\frac{\partial^2 w}{\partial y^2}+\frac{\partial^2 w}{\partial z^2}\right). \tag{3.5d}$$

(3.5e)

By introducing the velocity (3.3) and pressure (3.4) decompositions into equations 3.5, we obtain

$$\frac{\partial(U+u')}{\partial x}+\frac{\partial(V+v')}{\partial y}+\frac{\partial(W+w')}{\partial z}=0, \tag{3.6a}$$

$$\begin{aligned}\rho\left[\frac{\partial(U+u')}{\partial t}+(U+u')\frac{\partial(U+u')}{\partial x}+(V+v')\frac{\partial(U+u')}{\partial y}+(W+w')\frac{\partial(U+u')}{\partial z}\right]=\\ -\frac{\partial(P+p')}{\partial x}+\mu\left[\frac{\partial^2(U+u')}{\partial x^2}+\frac{\partial^2(U+u')}{\partial y^2}+\frac{\partial^2(U+u')}{\partial z^2}\right],\end{aligned} \tag{3.6b}$$

$$\begin{aligned}\rho\left[\frac{\partial(V+v')}{\partial t}+(U+u')\frac{\partial(V+v')}{\partial x}+(V+v')\frac{\partial(V+v')}{\partial y}+(W+w')\frac{\partial(V+v')}{\partial z}\right]=\\ -\frac{\partial(P+p')}{\partial y}+\mu\left[\frac{\partial^2(V+v')}{\partial x^2}+\frac{\partial^2(V+v')}{\partial y^2}+\frac{\partial^2(V+v')}{\partial z^2}\right],\end{aligned} \tag{3.6c}$$

$$\begin{aligned}\rho\left[\frac{\partial(W+w')}{\partial t}+(U+u')\frac{\partial(W+w')}{\partial x}+(V+v')\frac{\partial(W+w')}{\partial y}+(W+w')\frac{\partial(W+w')}{\partial z}\right]=\\ -\frac{\partial(P+p')}{\partial z}+\mu\left[\frac{\partial^2(W+w')}{\partial x^2}+\frac{\partial^2(W+w')}{\partial y^2}+\frac{\partial^2(W+w')}{\partial z^2}\right].\end{aligned} \tag{3.6d}$$

The known steady base flow field is also a solution to the Navier-Stokes equations and can thus be subtracted from the problem. The equations of 3.6 then become the disturbance equations:

$$\frac{\partial u'}{\partial x}+\frac{\partial v'}{\partial y}+\frac{\partial w'}{\partial z}=0, \tag{3.7a}$$

$$\begin{aligned}\frac{\partial u'}{\partial t}+U\frac{\partial u'}{\partial x}+u'\frac{\partial u'}{\partial x}+u'\frac{\partial U}{\partial x}+V\frac{\partial u'}{\partial y}+v'\frac{\partial u'}{\partial y}+v'\frac{\partial U}{\partial y}+W\frac{\partial u'}{\partial z}+w'\frac{\partial u'}{\partial z}+w'\frac{\partial U}{\partial z}\\ +\frac{1}{\rho}\frac{\partial p'}{\partial x}-\nu\left[\frac{\partial^2 u'}{\partial x^2}+\frac{\partial^2 u'}{\partial y^2}+\frac{\partial^2 u'}{\partial z^2}\right]=0,\end{aligned} \tag{3.7b}$$

$$\begin{aligned}\frac{\partial v'}{\partial t}+U\frac{\partial v'}{\partial x}+u'\frac{\partial v'}{\partial x}+u'\frac{\partial V}{\partial x}+V\frac{\partial v'}{\partial y}+v'\frac{\partial v'}{\partial y}+v'\frac{\partial V}{\partial y}+W\frac{\partial v'}{\partial z}+w'\frac{\partial v'}{\partial z}+w'\frac{\partial V}{\partial z}\\ +\frac{1}{\rho}\frac{\partial p'}{\partial y}-\nu\left[\frac{\partial^2 v'}{\partial x^2}+\frac{\partial^2 v'}{\partial y^2}+\frac{\partial^2 v'}{\partial z^2}\right]=0,\end{aligned} \tag{3.7c}$$

$$\begin{aligned}\frac{\partial w'}{\partial t}+U\frac{\partial w'}{\partial x}+u'\frac{\partial w'}{\partial x}+u'\frac{\partial W}{\partial x}+V\frac{\partial w'}{\partial y}+v'\frac{\partial w'}{\partial y}+v'\frac{\partial W}{\partial y}+w'\frac{\partial w'}{\partial z}+W\frac{\partial w'}{\partial z}+w'\frac{\partial W}{\partial z}\\ +\frac{1}{\rho}\frac{\partial p'}{\partial z}-\nu\left[\frac{\partial^2 w'}{\partial x^2}+\frac{\partial^2 w'}{\partial y^2}+\frac{\partial^2 w'}{\partial z^2}\right]=0,\end{aligned} \tag{3.7d}$$

which are the basis for all stability methods considered in this thesis.

A Fourier ansatz is introduced in the perturbation variables that assumes all perturbations behave harmonically in space and time. The mathematical description of the perturbations that results from this ansatz

depends on the other assumptions and neglected flow physics. In this report, local Linear Stability Theory (LST) and Parabolized Stability Equations (PSE) formulations are considered, where the PSE formulation takes into account the history of the flow. This fact returns in the description of the perturbations of the PSE, whereas the variation of x does not return in the LST formulation. For now, we will only consider the Linear Parabolized Stability Equations (LPSE) where an isolated mode is analyzed. The perturbations are described as exponentially growing eigenmodes [12] decomposed in a shape function $\hat{q}$ and an exponential wave function. The LST perturbation ansatz reads

$$q'(x,y,z,t) \equiv \hat{q}(y)e^{i(\alpha x+\beta z-\omega t)} + \text{c.c.}, \tag{3.8}$$

whilst the LPSE perturbations ansatz reads

$$q'(x,y,z,t) \equiv \hat{q}(x,y)e^{i\left(\int_{x_0}^{x}\alpha(x^*)dx^*+\beta z-\omega t\right)} + \text{c.c.}, \tag{3.9}$$

where α ($\in \mathbb{C}$) and β ($\in \mathbb{R}$) are the streamwise and spanwise wave numbers respectively. The angular frequency of the wave is given by ω and i is the imaginary number $i = \sqrt{-1}$. The asterisk in the PSE formulation is added to distinguish between the integration variable and the physical variable x. A hat is used to mark a shape function that describes the perturbation profile. The streamwise wavenumber α is complex with the imaginary part describing the perturbation growth rate, see [16]. In this thesis spanwise invariant flow is considered and instabilities can thus only grow in streamwise direction. The spanwise wavenumber β is thus real. The complex conjugates arise due to the description of sinusoidal functions using exponential functions as will be explained in section 4.7.1.

For the PSE, since streamwise changes are accounted for, the shape function $\hat{q}$ and α are functions of x. For α this returns in the ansatz as an integral of α over x rather than a multiplication with x. What the implications of a changing shape function with x are, will be discussed in section 3.5 when considering the PSE specifically.

3.3. Linearity

The Orr-Sommerfeld equation, is a linear method that thus ignores the nonlinear terms present in the equations. For infinitesimally small amplitudes the linear relations can predict the evolution of such perturbations [41]. Small amplitudes imply that the perturbation amplitude is of a much smaller order than the base flow, i.e.,

$$\vec{q}' \ll \vec{Q} \tag{3.10}$$

and similarly

$$\vec{p}' \ll \vec{P}. \tag{3.11}$$

In order to explain mathematically the concept of linearity, we follow Nair and Singh in [31]. Let V and W be vector spaces over the same field $\mathbb{F}$ where a field is a set, .e.g. the real numbers $\mathbb{R}$ or complex numbers $\mathbb{C}$. A function T is then linear if it satisfies the conditions of additivity, i.e.,

$$\forall x, y \in V, \quad T(x+y) = T(x) + T(y), \tag{3.12}$$

and homogeneity, i.e.,

$$\forall x, \alpha \in \mathbb{F}, \quad T(\alpha x) = \alpha T(x). \tag{3.13}$$

Nonlinear terms in the stability equations can therefore be defined as terms that result in functions that do not follow either or both of these conditions and can physically be interpreted as the interaction between the different inputs x and y in equations 3.12 and 3.13. These interactions are multiplications, thus if x and y are small, $\mathcal{O}(\epsilon)$ where $\epsilon \ll 1$, in the previous example, that means their interactions are of an even smaller order and can consequently be neglected. For finite inputs, or amplitudes in stability analysis, these interactions can be significant and affect the results. These terms will therefore not be neglected in the nonlinear formulations.

3.4. Orr-Sommerfeld equation

The Orr-Sommerfeld (OS) equation follows from the disturbance equations after certain flow assumptions and the perturbation anstaz are introduced. Despite the simplifications, the Orr-Sommerfeld equations provide an accurate prediction of transition via the e^N-method.

The OS equation is derived by introducing the following assumptions in equations 3.7:

1. All nonlinear interactions can be neglected.

2. Parallel flow is assumed which entails that the base flow components are functions of the wall-normal coordinate y only, and $V = 0$, i.e., $\vec{Q} = [U(y)\ 0\ W(y)]$.

The wall-normal component is assumed zero because a local technique cannot account for boundary layer growth. As a consequence, there can be no wall-normal velocity component as this implies that the boundary layer is growing, thus breaking the parallel flow assumption.

Forwarding the assumptions and introducing the ansatz of equation 3.8 to the disturbance equations presented in 3.7 results in the following set of linear partial differential equations:

$$i\alpha\hat{u} + \frac{\partial\hat{v}}{\partial y} + i\beta\hat{w} = 0, \tag{3.14a}$$

$$-i\omega\hat{u} + Ui\alpha\hat{u} + \hat{v}\frac{dU}{dy} + Wi\beta\hat{u} = -\frac{1}{\rho}i\alpha\hat{p} + \frac{\mu}{\rho}\left[\frac{\partial^2\hat{u}}{\partial y^2} - (\alpha^2+\beta^2)\hat{u}\right], \tag{3.14b}$$

$$-i\omega\hat{v} + Ui\alpha\hat{v} + Wi\beta\hat{v} = -\frac{1}{\rho}\frac{\partial\hat{p}}{\partial y} + \frac{\mu}{\rho}\left[\frac{\partial^2\hat{v}}{\partial y^2} - (\alpha^2+\beta^2)\hat{v}\right], \tag{3.14c}$$

$$-i\omega\hat{w} + Ui\alpha\hat{w} + \hat{v}\frac{dW}{dy} + Wi\beta\hat{w} = -\frac{1}{\rho}i\beta\hat{p} + \frac{\mu}{\rho}\left[\frac{\partial^2\hat{w}}{\partial y^2} - (\alpha^2+\beta^2)\hat{w}\right], \tag{3.14d}$$

which are called the Incompressible Local Stability Equations (ILST). The ILST can be rewritten, meaning no further assumptions need to be done, to give the Orr-Sommerfeld equation. It is presented here in dimensional form:

$$\left[\left(i\omega - i\alpha U - i\beta W\right)\left(\frac{\partial^2}{\partial y^2} - \alpha^2 - \beta^2\right) + \alpha i\frac{d^2U}{dy^2} + \beta i\frac{d^2W}{dy^2} + \nu\left(\frac{\partial^2}{\partial y^2} - \alpha^2 - \beta^2\right)^2\right]\hat{v} = 0. \tag{3.15}$$

The Orr-Sommerfeld equation is an eigenvalue problem that can be solved to find the eigenvalue α or ω depending on a spatial or temporal approach respectively and the eigenfunction $\hat{v}$ which is the shape function of the wall-normal disturbance velocity. Only the growth rate is necessary to predict transition, however, as it can be used to calculate the growth of the considered instability and correlated to transition as was explained in 2.4.1.

3.5. Linear parabolized stability equations

The local solution provided by the Orr-Sommerfeld equation assumes parallel flow and as such ignores streamwise variations of the base flow and perturbations. The Linear Parabolized Stability Equations (LPSE) predict the evolution of perturbations without assuming parallel flow and allow for a streamwise dependency of the shape function and streamwise wavenumber. The derivation of the LPSE will start from eqs. 3.7.

Two differences with respect to the shape function and wave function of the Orr-Sommerfeld equation should first be noted. The shape is a function of both x and y and the wave function contains an integration of an x-dependent α. This integration accounts for the history of the the mode. The complex conjugate is merely here for mathematical correctness as, again, mode interactions are not considered in a linear framework. We will proceed to use only the real part of the ansatz for computations.

In order to parabolize the equations of 3.7, an additional assumption is required that is related to the rate

of change of the shape and wave function [32]. Without this, the equations would remain of elliptic nature and thus be influenced by downstream effects, severely complicating the solution algorithm. It is assumed that the shape function changes slowly in x, whereas the wave function can change rapidly in x. This allows us to introduce the slowly varying coordinate $\xi = \epsilon x$ with $\epsilon = \mathcal{O}(Re^{-1})$ [32]. Equation 3.9 can then be rewritten as

$$q'(x,y,z,t) = \hat{q}(\xi,y)\, e^{i\left(\int_{\tilde{x}_0}^{\tilde{x}} \alpha(x)_{m,n} dx + \beta_m z - \omega_n t\right)}. \tag{3.16}$$

By, for instance, considering the shape function of the velocity perturbation in x-direction, $\hat{u}$, applying the chain rule yields

$$\frac{\partial \hat{u}}{\partial x} = \frac{\partial \xi}{\partial x}\frac{\partial \hat{u}}{\partial \xi} = \frac{1}{Re}\frac{\partial \hat{u}}{\partial \xi}. \tag{3.17}$$

The first-order streamwise derivative of u' then becomes

$$\frac{\partial u'}{\partial x} = \left(\frac{1}{Re}\frac{\partial \hat{u}}{\partial \xi} + i\alpha\hat{u}\right) e^{i\left(\int_{\tilde{x}_0}^{\tilde{x}} \alpha(x) \partial x + \beta z - \omega t\right)}, \tag{3.18}$$

and the second-order derivative reads

$$\frac{\partial^2 u'}{\partial x^2} = \left(\frac{1}{Re^2}\frac{\partial^2 \hat{u}}{\partial \xi^2} + \frac{i2\alpha}{Re}\frac{\partial \hat{u}}{\partial \xi} + \frac{i\hat{u}}{Re}\frac{\partial \alpha}{\partial \xi} - \alpha^2\hat{u}\right) e^{i\left(\int_{\tilde{x}_0}^{\tilde{x}} \alpha(x) \partial x + \beta z - \omega t\right)}. \tag{3.19}$$

The term $\frac{1}{Re^2}\frac{\partial^2 \hat{u}}{\partial \xi^2}$ is elliptical as it requires downstream information. Following an order of magnitude analysis, it can be seen that this term is much smaller than the other terms in the equation and can thus be neglected [3, 32]. This parabolizes the equations and remains valid if streamwise gradients are small. The use of ξ will be omitted from here on as it was merely introduced to prove the parabolicity of the equations in the case of a slowly varying shape function.

Forwarding this ansatz into the linear disturbance equations results in the following set of linear partial differential equations:

$$i\alpha\hat{u} + \frac{\partial \hat{u}}{\partial x} + \frac{\partial \hat{v}}{\partial y} + i\beta\hat{w} = 0, \tag{3.20a}$$

$$\begin{aligned} -i\omega\hat{u} + Ui\alpha\hat{u} + U\frac{\partial \hat{u}}{\partial x} + \hat{u}\frac{\partial U}{\partial x} + V\frac{d\hat{u}}{dy} + \hat{v}\frac{\partial U}{\partial y} + i\beta W\hat{u} + \frac{i\alpha}{\rho}\hat{p} + \frac{1}{\rho}\frac{\partial \hat{p}}{\partial x} \\ - \nu\left[i2\alpha\frac{\partial \hat{u}}{\partial x} + i\hat{u}\frac{\partial \alpha}{\partial x} + \frac{\partial^2 \hat{u}}{\partial y^2} - (\alpha^2+\beta^2)\hat{u}\right] = 0, \end{aligned} \tag{3.20b}$$

$$\begin{aligned} -i\omega\hat{v} + Ui\alpha\hat{v} + U\frac{\partial \hat{v}}{\partial x} + u'\frac{\partial V}{\partial x} + V\frac{\partial \hat{v}}{\partial y} + \hat{v}\frac{\partial V}{\partial y} + i\beta W\hat{v} + \frac{1}{\rho}\frac{\partial \hat{p}}{\partial y} \\ - \nu\left[i2\alpha\frac{\partial \hat{v}}{\partial x} + i\hat{v}\frac{\partial \alpha}{\partial x} + \frac{\partial^2 \hat{v}}{\partial y^2} - (\alpha^2+\beta^2)\hat{v}\right] = 0, \end{aligned} \tag{3.20c}$$

$$\begin{aligned} -i\omega\hat{w} + Ui\alpha\hat{w} + U\frac{\partial \hat{w}}{\partial x} + u'\frac{\partial W}{\partial x} + V\frac{\partial \hat{w}}{\partial y} + \hat{v}\frac{\partial W}{\partial y} + i\beta W\hat{w} + \frac{i\beta}{\rho}\hat{p} \\ - \nu\left[i2\alpha\frac{\partial \hat{w}}{\partial x} + i\hat{w}\frac{\partial \alpha}{\partial x} + \frac{\partial^2 \hat{w}}{\partial y^2} - (\alpha^2+\beta^2)\hat{w}\right] = 0. \end{aligned} \tag{3.20d}$$

3.6. Normalization condition

In the PSE framework, that includes both the Linear PSE and Nonlinear PSE (NPSE), $\hat{q}$ can vary in x resulting in an additional degree of freedom in the system. This means the ansatz currently contains two functions that can capture growth. An additional equation is required to reduce this freedom and enforce merely shape change of $\hat{q}$. This is done through the normalization condition:

$$\int \hat{q}^\dagger \frac{\partial \hat{q}}{\partial x} dy = 0, \tag{3.21}$$

where the † symbol denotes the complex conjugate of that respective mode. This formulation removes the dependency of the local wavenumber on the wall-normal coordinate [16]. Therefore, equation 3.21 performs a weighted integral of the modal growth, i.e., more change is allowed for greater relative velocities. The formulation ensures that the integral of the shape function cannot change rapidly from one discrete station to the next.

This condition is used to make the kinetic energy of the shape function independent of the streamwise coordinate [15]. It does not, however, put a restriction on the change of the maximum value which is often used to plot the amplitude of the wave in literature. Over time, this maximum amplitude of the wave might therefore change. A correction can be made for this, that registers all amplitudes based on the maximum value of the streamwise component of the shape function u' over x. The amplitude appointed to a mode is corrected by multiplication with the maximum value of the shape function, which deviates only slightly from 1, to ensure consistency in the plots. This correction is explained when considering the solution algorithm in section 4.6.

3.7. Nonlinear parabolized stability equations

The Nonlinear Parabolized Stability Equations (NPSE) are derived from the disturbance equations presented in section 3.2.1. This set of partial differential equations will, in contrast to the LPSE and OSE, not neglect the nonlinear terms.

The disturbance equations presented in 3.7 contain terms on the left-hand side that are products of perturbation quantities. They will be placed on the right-hand side of the equations. The base flow is assumed to be spanwise invariant. This means all base flow derivatives with respect to z are zero. Due to periodicity in spanwise direction, the perturbation derivatives with respect to this direction do not equal zero. Forwarding the assumptions to the equations yields

$$\frac{\partial u'}{\partial x} + \frac{\partial v'}{\partial y} + \frac{\partial w'}{\partial z} = 0 \tag{3.22a}$$

$$\frac{\partial u'}{\partial t} + U\frac{\partial u'}{\partial x} + u'\frac{\partial U}{\partial x} + V\frac{\partial u'}{\partial y} + v'\frac{\partial U}{\partial y} + W\frac{\partial u'}{\partial z} + \frac{1}{\rho}\frac{\partial p'}{\partial x} - \nu\left[\frac{\partial^2 u'}{\partial x^2} + \frac{\partial^2 u'}{\partial y^2} + \frac{\partial^2 u'}{\partial z^2}\right] = -u'\frac{\partial u'}{\partial x} - v'\frac{\partial u'}{\partial y} - w'\frac{\partial u'}{\partial z}, \tag{3.22b}$$

$$\frac{\partial v'}{\partial t} + U\frac{\partial v'}{\partial x} + u'\frac{\partial V}{\partial x} + V\frac{\partial v'}{\partial y} + v'\frac{\partial V}{\partial y} + W\frac{\partial v'}{\partial z} + \frac{1}{\rho}\frac{\partial p'}{\partial y} - \nu\left[\frac{\partial^2 v'}{\partial x^2} + \frac{\partial^2 v'}{\partial y^2} + \frac{\partial^2 v'}{\partial z^2}\right] = -u'\frac{\partial v'}{\partial x} - v'\frac{\partial v'}{\partial y} - w'\frac{\partial v'}{\partial z}, \tag{3.22c}$$

$$\frac{\partial w'}{\partial t} + U\frac{\partial w'}{\partial x} + u'\frac{\partial W}{\partial x} + V\frac{\partial w'}{\partial y} + v'\frac{\partial W}{\partial y} + W\frac{\partial w'}{\partial z} + \frac{1}{\rho}\frac{\partial p'}{\partial z} - \nu\left[\frac{\partial^2 w'}{\partial x^2} + \frac{\partial^2 w'}{\partial y^2} + \frac{\partial^2 w'}{\partial z^2}\right] = -u'\frac{\partial w'}{\partial x} - v'\frac{\partial w'}{\partial y} - w'\frac{\partial w'}{\partial z}. \tag{3.22d}$$

The inserted perturbations in a nonlinear setting cannot be the monochromatic waves used in linear solution methods. The disturbance must account for the complete set of modes such that its interactions can be calculated through the nonlinear terms. The decomposition of the waves into a slowly varying shape function and a rapidly varying wave function remains. The slowly varying shape function again serves as the key to arrive at governing partial differential equations of parabolic type [4]. Accordingly, a perturbation quantity is expressed as a truncated sum of modes, i.e.,

$$q'(x,y,z,t) = \sum_{m=0}^{M}\sum_{n=0}^{N} \underbrace{\hat{q}_{m,n}(x,y)}_{\text{shape function}} \underbrace{e^{i\left(\int_{x_0}^{x_e}\alpha(x)_{m,n}dx + \beta_m z - \omega_n t\right)}}_{\text{wave function}} + \text{c.c}, \tag{3.23}$$

in which the steady zero-mode, for which both n and m are zero, represents the mean flow distortion and N and M represent the highest harmonic of α and ω captured in the truncation. Respectively, the wavenumbers

are defined as multiplications of the first harmonic, i.e.,

$$\beta_m = m\beta_1, \tag{3.24}$$

and

$$\omega_n = n\omega_1. \tag{3.25}$$

The a priori unknown complex wavenumber α depends on n and m as well, although both its real and imaginary part are to be calculated through solving the NPSE. The summation of 3.23 is truncated for implementation purposes as it is computationally unfeasible to describe the perturbation using an infinite sum.

Despite the complex conjugates not being physical, they can interact with and have an effect on physical modes and must therefore be included. The complex conjugate of a wave, $q'^{\dagger}$, manifests itself as the negative counterpart of the wavelength and frequency, i.e., $q'_{-n,-m} = q'^{\dagger}_{n,m}$ [16]. This means the decomposition can also be written as the sum from $-N$ to N and $-M$ to M, omitting the addition of the complex conjugates, as follows:

$$q'(x,y,z,t) = \sum_{m=-M}^{M}\sum_{n=-N}^{N} \underbrace{\hat{q}_{m,n}(x,y)}_{\text{shape function}} \underbrace{e^{i\left(\int_{x_0}^{x_e}\alpha(x)_{m,n}dx+\beta_m z-\omega_n t\right)}}_{\text{wave function}}. \tag{3.26}$$

This formulation includes the zero-mode, which represents the mean flow distortion that arises from the interaction of modes with their own complex conjugate.

A slowly varying shape function is again required to be able to parabolize the equations. The elliptic term is neglected based on an order of magnitude analysis following the description presented earlier in equation 3.19. The parabolization of the NPSE follows the same process.

Introducing the ansatz of 3.26 into equations 3.22 yields the nonlinear parabolized stability equations:

$$i\alpha\hat{u} + \frac{\partial\hat{u}}{\partial x} + \frac{\partial\hat{v}}{\partial y} + i\beta\hat{w} = 0, \tag{3.27a}$$

$$\begin{aligned} &-i\omega\hat{u} + Ui\alpha\hat{u} + U\frac{\partial\hat{u}}{\partial x} + \hat{u}\frac{\partial U}{\partial x} + V\frac{d\hat{u}}{dy} + \hat{v}\frac{\partial U}{\partial y} + i\beta W\hat{u} + \frac{i\alpha}{\rho}\hat{p} + \frac{1}{\rho}\frac{\partial\hat{p}}{\partial x} \\ &\quad - \nu\left[i2\alpha\frac{\partial\hat{u}}{\partial x} + i\hat{u}\frac{\partial\alpha}{\partial x} + \frac{\partial^2\hat{u}}{\partial y^2} - (\alpha^2+\beta^2)\hat{u}\right] = -i\alpha\hat{u}^2 - \hat{u}\frac{\partial\hat{u}}{\partial x} - \hat{v}\frac{\partial\hat{u}}{\partial y} - i\beta\hat{w}\hat{u}, \end{aligned} \tag{3.27b}$$

$$\begin{aligned} &-i\omega\hat{v} + Ui\alpha\hat{v} + U\frac{\partial\hat{v}}{\partial x} + u'\frac{\partial V}{\partial x} + V\frac{\partial\hat{v}}{\partial y} + \hat{v}\frac{\partial V}{\partial y} + i\beta W\hat{v} + \frac{1}{\rho}\frac{\partial\hat{p}}{\partial y} \\ &\quad - \nu\left[i2\alpha\frac{\partial\hat{v}}{\partial x} + i\hat{v}\frac{\partial\alpha}{\partial x} + \frac{\partial^2\hat{v}}{\partial y^2} - (\alpha^2+\beta^2)\hat{v}\right] = -i\alpha\hat{u}\hat{v} - \hat{u}\frac{\partial\hat{v}}{\partial x} - \hat{v}\frac{\partial\hat{v}}{\partial y} - i\beta\hat{w}\hat{v}, \end{aligned} \tag{3.27c}$$

$$\begin{aligned} &-i\omega\hat{w} + Ui\alpha\hat{w} + U\frac{\partial\hat{w}}{\partial x} + u'\frac{\partial W}{\partial x} + \hat{v}\frac{\partial W}{\partial y} + V\frac{\partial\hat{w}}{\partial y} + i\beta W\hat{w} + \frac{i\beta}{\rho}\hat{p} \\ &\quad - \nu\left[i2\alpha\frac{\partial\hat{w}}{\partial x} + i\hat{w}\frac{\partial\alpha}{\partial x} + \frac{\partial^2\hat{w}}{\partial y^2} - (\alpha^2+\beta^2)\hat{w}\right] = -i\alpha\hat{u}\hat{w} - \hat{u}\frac{\partial\hat{w}}{\partial x} - \hat{v}\frac{\partial\hat{w}}{\partial y} - i\beta\hat{w}^2. \end{aligned} \tag{3.27d}$$

The equations of 3.27 form a set of inhomogeneous partial differential equations subjected to the no-slip boundary condition at the wall and the condition of disturbances fading out in the freestream, i.e.,

$$\hat{u}|_{y=0} = 0, \quad \hat{v}|_{y=0} = 0, \quad \hat{w}|_{y=0} = 0,$$

$$\hat{u}|_{y\to\infty} = 0, \quad \hat{v}|_{y\to\infty} = 0, \quad \hat{w}|_{y\to\infty} = 0,$$

The mean flow distortion requires different boundary conditions as its effect does not fade in the freestream. The mean flow distortion increases the boundary layer thickness and its velocity contribution in the wall-normal direction, v', is therefore not set to zero at the top boundary, i.e.,

$$\hat{u}|_{y=0} = 0, \quad \hat{v}|_{y=0} = 0, \quad \hat{w}|_{y=0} = 0,$$

$$\hat{u}|_{y\to\infty} = 0, \quad \hat{w}|_{y\to\infty} = 0.$$

This leaves the top boundary condition free for the zero-mode, however, the continuity equation should still hold. The continuity equation thus provides the boundary condition for the wall-normal component of the mean flow distortion.

Analogous to the LPSE derivation presented in section 3.5, the ambiguity in the formulation of a growing shape function has to be removed from the equations. The NPSE is therefore also subject to the normalization condition of equation 3.6.

3.7.1. Nondimensionalization of the NPSE

The nonlinear parabolized stability equations derived in section 3.7 are in dimensional form. This section tackles the nondimensionalization of the NPSE for comparison purposes.

The freestream velocity at the inflow, U_0, and the Blasius length at the inflow, δ_0, are chosen as the characteristic velocity and length respectively. All relevant quantities are consequently nondimensionalized as follows:

$$U = \bar{U}U_0, \quad W = \bar{W}U_0, \quad \alpha = \frac{\bar{\alpha}}{\delta_0}, \quad \beta = \frac{\bar{\beta}}{\delta_0}, \quad y = \eta\delta_0, \quad x = \bar{x}\delta_0, \quad \omega = \frac{\bar{\omega}U_0}{\delta_0},$$
$$\nu = \frac{U_0\delta_0}{Re}, \quad \hat{u} = \bar{u}U_0, \quad \hat{v} = \bar{v}U_0, \quad \hat{w} = \bar{w}U_0 \quad \texttt{and} \quad \hat{p} = \bar{p}\rho U_0^2.$$

By introducing the nondimensional quantities into equation 3.27, we obtain

$$\frac{U_0}{\delta_0}\left(i\bar{\alpha}\bar{u} + \frac{\partial\bar{u}}{\partial\bar{x}} + \frac{\partial\bar{v}}{\partial\eta} + i\bar{\beta}\bar{w}\right) = 0, \tag{3.28a}$$

$$\frac{U_0^2}{\delta_0}\left(-i\bar{\omega}\bar{u} + \bar{U}i\bar{\alpha}\bar{u} + \bar{U}\frac{\partial\bar{u}}{\partial\bar{x}} + \bar{u}\frac{\partial\bar{U}}{\partial\bar{x}} + \bar{V}\frac{d\bar{u}}{d\eta} + \bar{v}\frac{\partial\bar{U}}{\partial\eta} + i\bar{\beta}\bar{W}\bar{u} + i\bar{\alpha}\bar{p} + \frac{\partial\bar{p}}{\partial\bar{x}}\right)$$
$$- \frac{U_0^2\delta_0}{Re\delta_0^2}\left[i2\bar{\alpha}\frac{\partial\bar{u}}{\partial\bar{x}} + i\bar{u}\frac{\partial\bar{\alpha}}{\partial\bar{x}} + \frac{\partial^2\bar{u}}{\partial\eta^2} - (\bar{\alpha}^2+\bar{\beta}^2)\bar{u}\right] = \frac{U_0^2}{\delta_0}\left(-i\bar{\alpha}\bar{u}^2 - \bar{u}\frac{\partial\bar{u}}{\partial\bar{x}} - \bar{v}\frac{\partial\bar{u}}{\partial\eta} - i\bar{\beta}\bar{w}\bar{u}\right), \tag{3.28b}$$

$$\frac{U_0^2}{\delta_0}\left(-i\bar{\omega}\bar{v} + \bar{U}i\bar{\alpha}\bar{v} + \bar{U}\frac{\partial\bar{v}}{\partial\bar{x}} + \bar{u}\frac{\partial\bar{V}}{\partial\bar{x}} + \bar{V}\frac{\partial\bar{v}}{\partial\eta} + \bar{v}\frac{\partial\bar{V}}{\partial\eta} + i\bar{\beta}\bar{W}\bar{v} + \frac{\partial\bar{p}}{\partial\eta}\right)$$
$$- \frac{U_0^2\delta_0}{Re\delta_0^2}\left[i2\bar{\alpha}\frac{\partial\bar{v}}{\partial\bar{x}} + i\bar{v}\frac{\partial\bar{\alpha}}{\partial\bar{x}} + \frac{\partial^2\bar{v}}{\partial\eta^2} - (\bar{\alpha}^2+\bar{\beta}^2)\bar{v}\right] = \frac{U_0^2}{\delta_0}\left(-i\bar{\alpha}\bar{u}\bar{v} - \bar{u}\frac{\partial\bar{v}}{\partial\bar{x}} - \bar{v}\frac{\partial\bar{v}}{\partial\eta} - i\bar{\beta}\bar{w}\bar{v}\right), \tag{3.28c}$$

$$\frac{U_0^2}{\delta_0}\left(-i\bar{\omega}\bar{w} + \bar{U}i\bar{\alpha}\bar{w} + \bar{U}\frac{\partial\bar{w}}{\partial\bar{x}} + \bar{u}\frac{\partial\bar{W}}{\partial\bar{x}} + \bar{v}\frac{\partial\bar{W}}{\partial\eta} + \bar{V}\frac{\partial\bar{w}}{\partial\eta} + i\bar{\beta}\bar{W}\bar{w} + i\bar{\beta}\bar{p}\right)$$
$$- \frac{U_0^2\delta_0}{Re\delta_0^2}\left[i2\bar{\alpha}\frac{\partial\bar{w}}{\partial\bar{x}} + i\bar{w}\frac{\partial\bar{\alpha}}{\partial\bar{x}} + \frac{\partial^2\bar{w}}{\partial\eta^2} - (\bar{\alpha}^2+\bar{\beta}^2)\bar{w}\right] = \frac{U_0^2}{\delta_0}\left(-i\bar{\alpha}\bar{u}\bar{w} - \bar{u}\frac{\partial\bar{w}}{\partial\bar{x}} - \bar{v}\frac{\partial\bar{w}}{\partial\eta} - i\bar{\beta}\bar{w}^2\right). \tag{3.28d}$$

or, alternatively,

$$i\bar{\alpha}\bar{u}+\frac{\partial\bar{u}}{\partial\bar{x}}+\frac{\partial\bar{v}}{\partial\eta}+i\bar{\beta}\bar{w}=0, \tag{3.29a}$$

$$\begin{aligned}-i\bar{\omega}\bar{u}+\bar{U}i\bar{\alpha}\bar{u}+\bar{U}\frac{\partial\bar{u}}{\partial\bar{x}}+\bar{u}\frac{\partial\bar{U}}{\partial\bar{x}}+\bar{V}\frac{d\bar{u}}{d\eta}+\bar{v}\frac{\partial\bar{U}}{\partial\eta}+i\bar{\beta}\bar{W}\bar{u}+i\bar{\alpha}\bar{p}+\frac{\partial\bar{p}}{\partial\bar{x}}\\ -\frac{1}{Re}\left[i2\bar{\alpha}\frac{\partial\bar{u}}{\partial\bar{x}}+i\bar{u}\frac{\partial\bar{\alpha}}{\partial\bar{x}}+\frac{\partial^2\bar{u}}{\partial\eta^2}-(\bar{\alpha}^2+\bar{\beta}^2)\bar{u}\right]=-i\bar{\alpha}\bar{u}^2-\bar{u}\frac{\partial\bar{u}}{\partial\bar{x}}-\bar{v}\frac{\partial\bar{u}}{\partial\eta}-i\bar{\beta}\bar{w}\bar{u},\end{aligned} \tag{3.29b}$$

$$\begin{aligned}-i\bar{\omega}\bar{v}+\bar{U}i\bar{\alpha}\bar{v}+\bar{U}\frac{\partial\bar{v}}{\partial\bar{x}}+\bar{u}\frac{\partial\bar{V}}{\partial\bar{x}}+\bar{V}\frac{\partial\bar{v}}{\partial\eta}+\bar{v}\frac{\partial\bar{V}}{\partial\eta}+i\bar{\beta}\bar{W}\bar{v}+\frac{\partial\bar{p}}{\partial\eta}\\ -\frac{1}{Re}\left[i2\bar{\alpha}\frac{\partial\bar{v}}{\partial\bar{x}}+i\bar{v}\frac{\partial\bar{\alpha}}{\partial\bar{x}}+\frac{\partial^2\bar{v}}{\partial\eta^2}-(\bar{\alpha}^2+\bar{\beta}^2)\bar{v}\right]=-i\bar{\alpha}\bar{u}\bar{v}-\bar{u}\frac{\partial\bar{v}}{\partial\bar{x}}-\bar{v}\frac{\partial\bar{v}}{\partial\eta}-i\bar{\beta}\bar{w}\bar{v},\end{aligned} \tag{3.29c}$$

$$\begin{aligned}-i\bar{\omega}\bar{w}+\bar{U}i\bar{\alpha}\bar{w}+\bar{U}\frac{\partial\bar{w}}{\partial\bar{x}}+\bar{u}\frac{\partial\bar{W}}{\partial\bar{x}}+\bar{v}\frac{\partial\bar{W}}{\partial\eta}+\bar{V}\frac{\partial\bar{w}}{\partial\eta}+i\bar{\beta}\bar{W}\bar{w}+i\bar{\beta}\bar{p}\\ -\frac{1}{Re}\left[i2\bar{\alpha}\frac{\partial\bar{w}}{\partial\bar{x}}+i\bar{w}\frac{\partial\bar{\alpha}}{\partial\bar{x}}+\frac{\partial^2\bar{w}}{\partial\eta^2}-(\bar{\alpha}^2+\bar{\beta}^2)\bar{w}\right]=-i\bar{\alpha}\bar{u}\bar{w}-\bar{u}\frac{\partial\bar{w}}{\partial\bar{x}}-\bar{v}\frac{\partial\bar{w}}{\partial\eta}-i\bar{\beta}\bar{w}^2.\end{aligned} \tag{3.29d}$$

Equation 3.29 is the nondimensional form of the NPSE.

On the left-hand side of equation 3.29, terms can be recognized that contain either $\bar{q}$, $\frac{\partial\bar{q}}{\partial\bar{x}}$ or $\frac{\partial\bar{\alpha}}{\partial\bar{x}}\bar{q}$. Grouping these terms allows for the set of partial differential equations to be written in matrix form:

$$\mathbb{L}\bar{q}+\mathbb{M}\frac{\partial\bar{q}}{\partial\bar{x}}+\mathbb{N}\frac{\partial\bar{\alpha}}{\partial\bar{x}}\bar{q}=\bar{r}, \tag{3.30}$$

as suggested by Herbert [16]. The right-hand side in equation 3.30 acts as a source term containing the nonlinear terms. The continuity equation is homogeneous and the respective contents of vector $\bar{r}$ remain zero. The left-hand side of equation 3.30 is identical to equation 3.20, representing the LPSE system.

Additionally, a common term can be found in the momentum equations present in $\mathbb{L}$. This term is the so-called common convective-diffusion term $i\bar{\alpha}\bar{U}-i\bar{\omega}+\frac{1}{Re}(\bar{\alpha}^2+\bar{\beta}^2)+i\bar{\beta}\bar{W}-\frac{1}{Re}\frac{\partial^2}{\partial\eta^2}+\bar{V}\frac{\partial}{\partial\eta}$ which will hereafter be denoted as `"DEL"`. The contents of matrices $\mathbb{L}$, $\mathbb{M}$ and $\mathbb{N}$, as well as vector $\bar{r}$, can be found in appendix A.

3.8. Weakly nonparallel local stability solutions

In between the methods that assume parallel or nonparallel base flows, lies the Weakly Nonparallel Local (WNL) stability method. Herbert [15] states that previous linear stability methods, such as the Orr-Sommerfeld equation, neglect the nonparallel terms of the flow even though this cannot be done based on an order of magnitude analysis. The WNL equations incorporate the nonparallel terms in a first-order Taylor expansion around a known point. This method is of interest to the NPSE code as it can be used to generate an initial condition for the primary mode at the inflow.

In crossflows, this method has not been validated and requires additional care to select the physical solution among the eigenvalues that follow from the direct solution. It is out of the scope of this thesis and is recommended future work. The WNL formulation will thus only be used in the TS wave simulations.

The derivation of a direct solution to the weakly nonparallel local stability problem starts from the linear stability equations depicted in the equations of 3.7. Omitting the nonlinear forcing term, as this concerns a linear method, in the matrix system of equation 3.30, we find

$$\mathbb{L}\bar{q}+\mathbb{M}\frac{\partial\bar{q}}{\partial\bar{x}}+\mathbb{N}\frac{\partial\bar{\alpha}}{\partial\bar{x}}\bar{q}=0. \tag{3.31}$$

In order to account for changes in streamwise direction, we will approximate $\bar{\alpha}$, $\bar{q}$ and the base flow by a first-order Taylor expansion around some known point $\bar{x}_0$ and introducing $\bar{\alpha}_1$ and $\bar{q}_1$ that represent the streamwise derivative of $\bar{\alpha}$ and $\bar{q}$ respectively evaluated at $\bar{x}_0$, i.e.,

$$\begin{aligned}\bar{\alpha}(\bar{x}) &= \bar{\alpha}(\bar{x}_0) + (\bar{x}-\bar{x}_0)\frac{d\bar{\alpha}}{d\bar{x}}|_{\bar{x}_0} \\ &= \bar{\alpha}_0 + (\bar{x}-\bar{x}_0)\bar{\alpha}_1 = \bar{\alpha}_0 + \bar{\zeta}\bar{\alpha}_1,\end{aligned} \tag{3.32a}$$

$$\begin{aligned}\bar{q}(\bar{x}) &= \bar{q}(\bar{x}_0,\bar{y}) + (\bar{x}-\bar{x}_0)\frac{\partial\bar{q}}{\partial\bar{x}}|_{\bar{x}_0} \\ &= \bar{q}_0 + (\bar{x}-\bar{x}_0)\bar{q}_1 = \bar{q}_0 + \bar{\zeta}\bar{q}_1,\end{aligned} \tag{3.32b}$$

where $\bar{\zeta}$ is a translated coordinate defined as $(\bar{x}-\bar{x}_0)$. The expansion is performed locally and thus $\bar{\zeta}$ is small. The expansions of 3.32 are applied to the base flow components present in the system as well. Matrix $\mathbb{N}$ contains no base flow components and thus cannot be expanded. The expansion of equation 3.31 around a point $\bar{x}_0$ is

$$\left(\mathbb{L}_0+\bar{\zeta}\mathbb{L}_1\right)\left(\bar{q}_0+\bar{\zeta}\bar{q}_1\right)+\left(\mathbb{M}_0+\bar{\zeta}\mathbb{M}_1\right)\bar{q}_1+\mathbb{N}\bar{\alpha}_1\left(\bar{q}_0+\bar{\zeta}\bar{q}_1\right)=0. \tag{3.33}$$

Further manipulation leads to:

$$\mathbb{L}_0\bar{q}_0+\bar{\zeta}\mathbb{L}_1\bar{q}_0+\mathbb{L}_0\bar{\zeta}\bar{q}_1+\bar{\zeta}^2\mathbb{L}_1\bar{q}_1+\mathbb{M}_0\bar{q}_1+\bar{\zeta}\mathbb{M}_1\bar{q}_1+\mathbb{N}\bar{\alpha}_1\bar{q}_0+\bar{\zeta}\mathbb{N}\bar{\alpha}_1\bar{q}_1=0. \tag{3.34}$$

This expansion must hold at any location, including x_0, which allows us to write the equations for $x=x_0$ and for any arbitrary x. In addition, we can neglect some terms of smaller orders, leading to

$$(\zeta=0): \quad \mathbb{L}_0\bar{q}_0+\mathbb{M}_0\bar{q}_1=0, \tag{3.35a}$$

$$(\zeta\neq 0): \quad \mathbb{L}_1\bar{q}_0+\mathbb{L}_0\bar{q}_1=0. \tag{3.35b}$$

This problem can be rewritten in the shape $\mathbb{A}V=\mathbb{B}VD$, where D contains the eigenvalues of the system and V contains the eigenvectors. The eigenvector is not suited for this reformulation and thus the system must be rewritten using an extended eigenvector containing all powers of the eigenvalues $[\bar{q}_0,\alpha\bar{q}_0,\bar{q}_1,\alpha\bar{q}_1]^T$. The matrices $\mathbb{L}_0$, $\mathbb{L}_1$ and $\mathbb{M}_0$ must also be split accordingly by separating the terms that contain the powers α^0,α^1 and α^2 respectively. This will be denoted using a second subscript corresponding to the power of the eigenvalue with which it will be multiplied in the companion matrix method. For example, all the terms in $\mathbb{L}_0$ that do not contain any multiplications with α will be denoted $\mathbb{L}_{00}$. The system can be rewritten as:

$$\begin{bmatrix}\mathbb{L}_{00} & \mathbb{L}_{01} & \mathbb{M}_{00} & \mathbb{M}_{01}\\ 0 & I & 0 & 0\\ \mathbb{L}_{10} & \mathbb{L}_{11} & \mathbb{L}_{00} & \mathbb{M}_{01}\\ 0 & 0 & 0 & I\end{bmatrix}\begin{bmatrix}\bar{q}_0\\ \bar{\alpha}\bar{q}_0\\ \bar{q}_1\\ \bar{\alpha}\bar{q}_1\end{bmatrix}=\bar{\alpha}\begin{bmatrix}0 & -\mathbb{L}_{02} & 0 & 0\\ I & 0 & 0 & 0\\ 0 & 0 & 0 & -\mathbb{L}_{02}\\ 0 & 0 & I & 0\end{bmatrix}\begin{bmatrix}\bar{q}_0\\ \bar{\alpha}\bar{q}_0\\ \bar{q}_1\\ \bar{\alpha}\bar{q}_1,\end{bmatrix} \tag{3.36}$$

where the second and fourth row are necessary to close the system and I is the identity matrix. Solving this system gives the eigenvalue α and eigenfunctions $\bar{q}_0$ and $\bar{q}_1$ although the latter will not serve any purpose in the NPSE marching procedure.

4

Solution algorithm

This chapter tackles the numerical solution algorithm of the NPSE and aims to provide the reader with a thorough explanation of all required steps in programming the NPSE for spanwise invariant boundary layers. High and low-level architectures are provided as well as required corrections due to modelling and numerical errors.

4.1. Program architecture

Before going in-depth on the specific functions that are required to develop an NPSE solver, a high-level architecture will be presented that serves as a map for future explanations. The program architecture aims to show the dependency, order and general layout of the code without going into depth on what the contents of certain blocks are. The high-level architecture of the code is presented in appendix B.1.

The NPSE requires three initialization codes. The harmonic balancing matrices are generated to be able to look up the nonlinear interactions as will be explained in section 4.4. The spectral differentiation matrices are also generated which are used to differentiate in y-direction. The initial condition is generated using linear techniques for the primary mode and the results are normalized.

The outputs of these initialization scripts are fed into the initialization of the NPSE. An estimate is made here for the next step from which the code can converge to the correct solution of that step in the subsequent converging loop using a predictor-corrector approach. At the start of every iteration, mode interactions are calculated and compared against an introduction threshold to determine whether new modes should be introduced to the system. For these modes, an initial condition is generated using the mean flow. The results include the wavenumber α, amplitude A and shape function q. If no additional modes are expected to be significant, this part of the code is skipped.

Afterward, the equations of the NPSE are solved in parts by solving a system of coupled Inhomogeneous LPSE equations. All the nonlinear interactions are represented as source terms in these ILPSE equations. The results are used as an input for the Inhomogenous LPSE solver that calculates the new shape functions. The normalization condition redirects the growth present in this shape function to the amplitude and updates the growth rate. These steps are repeated until the maximum difference in all wavenumbers between two consecutive steps falls below a threshold. In future work, an optimization of this condition should be performed as the convergence of the highest harmonic is hardest to achieve. The primary mode converges rapidly and does not need to be recalculated. Currently, however, all modes are reconsidered when there is at least one mode that has not yet converged below the threshold.

4.2. Discretization

The NPSE are solved for point-wise values following a spectral method in wall-normal direction for discrete stages in the streamwise direction. The relevant domain for stability calculations is only a part of the total flow field. The start of the flat plate, and thus the origin of the boundary layer and its perturbations, is not inside this domain. The boundary layer, therefore, starts with a finite thickness in NPSE calculations. This is visualized in figure 4.1.

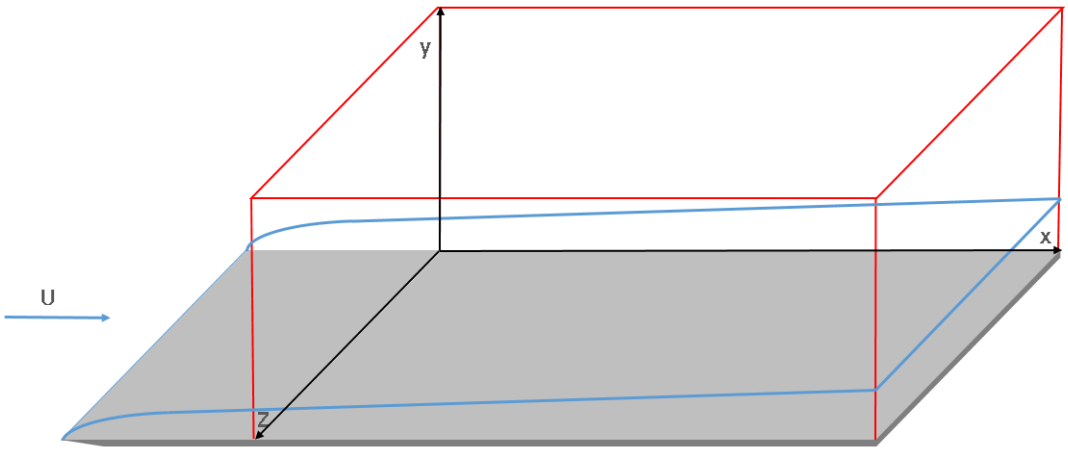

Figure 4.1: Computational domain (red box) for the NPSE in the leading edge orthogonal coordinate system x-y-z, and inflow velocity U showing a schematic boundary layer (blue lines) that originated upstream of the computational domain.

Here, the x, y and z-direction are the leading edge orthogonal, wall-normal and spanwise direction respectively. The marching direction is thus in the direction orthogonal to the leading edge. The freestream velocity can have an arbitrary angle with respect to the leading edge in this simulation.

The inflow plane already thus contains a developed boundary layer. It is in this plane that the initial condition is given in terms of superimposed modes and their amplitudes. The height of the domain is approximately five times greater than the boundary layer height. An optimization of the wall-normal discretization has to be performed manually. A limitation of the current code is that only one discretization type can be chosen that is maintained over the entire domain. This can cause problems in convergence and numerical stability as the discretization requirements might differ over the domain. This happens due to growth of the boundary layer and the presented modes as well as the introduction of higher harmonics that may require a more refined wall-normal discretization to be resolved.

The domain, shown in three dimensions, only contains two dimensions that are important for the calculations: x and y. Since the simulation concerns a spanwise invariant flow, a discretization in z is not required. In x, the domain is discretized using nx evenly spaced nodes.

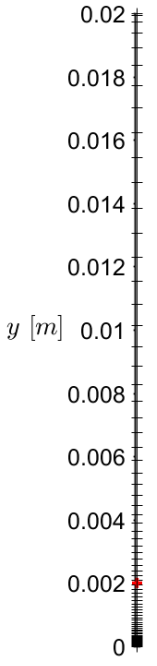

Figure 4.2: Wall-normal discretization example with the Chebyshev median indicated in red.

In the wall-normal direction, an adjusted discretization is performed aiming to increase the number of nodes close to the wall where shears are greatest. Both for the known base flow as for the superimposed instabilities, the strongest transients are found

inside the boundary layer. It is thus required that more nodes are present inside the boundary layer region to be able to capture and accurately represent the boundary layer itself and the instabilities. An example of the wall-normal discretization is shown in figure 4.2. Taking $H = 0.02[m]$ as the domain height, it is divided into ny number of nodes. It is important that this domain height H is much greater than the boundary layer in order to allow the shape functions to decay exponentially to zero in the freestream. Numerically the top boundary condition will be set to zero precisely for oscillatory modes, although, given the nature of exponential decay, a shape function will never actually reach zero. Therefore, increasing the domain height reduces this numerical boundary condition error. Then, the input of the location y_i is required, as presented in red in figure 4.2, which is the Chebyshev node coordinate median. An equal number of nodes is present under and above this location. This is exploited to result in a greater precision in the boundary layer than in the freestream where disturbances fade out slowly and wall-normal gradients are severely reduced. This significantly decreases the minimum required number of nodes to accurately represent the shape functions in the boundary layer. Consequently, this reduces the overall computational requirements.

4.3. Initial condition

The PSE framework exploits a marching scheme to solve the stability problem. This marching scheme requires an initial condition for the first stage that the mode is deemed relevant for computations that consists of an amplitude A, a shape function $\hat{q}$ and the initial wavenumber α. Three cases can be distinguished that require an initial condition:

1. Pre-defined modes.
2. Nonlinearly generated oscillatory modes.
3. Nonlinearly generated mean flow distortion.

There can be no mean flow distortion without other perturbations, i.e., the origin of the MFD is purely nonlinear. The mean flow distortion is therefore never introduced in the first stage and will always be generated nonlinearly, i.e. forced, during the NPSE marching.

In the current literature [4, 8, 14, 15, 32] the modeling of mode introductions appears to be varying greatly. Methods include combinations of OS, WNL and wavenumber averaging techniques. Wavenumber averaging is a procedure via which the wavenumber of a new mode is determined as being the average wavenumber from mode interactions. The main problem with a linear technique, for forced mode introductions, is that it fails to accurately predict the initial growth rate of higher harmonics. The growth rate of higher harmonics is often linearly stable while the need for their introduction indicates that they are unstable due to nonlinear effects, i.e., the modal growth is dominated by nonlinear effects. We introduce a new method that accounts for nonlinear introductions by exploiting the wavenumber averaging technique as described by Haynes and Reed [14], followed by an ILPSE marching step for forced oscillatory mode introduction, see section 4.3.2.

4.3.1. NPSE initial condition

At the inflow, an initial condition is generated that presents the instability waves into the flow. Their introduction requires a shape function, $\bar{q}$, wavenumbers and frequency, α, β and ω and an amplitude A; two of which can be generated using linear stability techniques. Those are the shape functions of the velocity components present in $\bar{q}$ and the streamwise wavenumber α. The β, ω and A are thus required user inputs. The techniques covered in this thesis for primary mode introduction are the ILST and WNL as presented in sections 3.4 and 3.8 respectively.

The inflow plane of the NPSE has to be in the linear regime where amplitudes are infinitesimal and nonlinear interactions can be neglected. This is a prerequisite since it is not possible to generate a nonlinear forcing term for this introduction as the components of this forcing term are unknown. Starting the simulation in the nonlinear regime means nonlinear terms are wrongfully neglected resulting in an erroneous state of the primary mode. As a result of the large amplitude of the primary mode, harmonics are hastily introduced based on the linear estimate of the primary mode, increasing the error. The NPSE simulation will therefore always have to be started in the linear regime to allow the use of a linear initial conditions and reduce the accumulation of errors in the system.

Equations 3.35 or 3.14 can be solved directly using a companion matrix method by finding the roots of a polynomial containing all powers of the eigenvalue α in a companion matrix system. A filter is applied to select the correct eigenfunction and corresponding eigenvalue from the results based on the exponential decay of the shape function in the freestream, see [19].

The weakly nonparallel solutions are accompanied by a duality in the eigenvalues as a result of the powers of the eigenvalues in the system. An example for this in the Tollmien-Schlichting case is presented in [3] and will be closer examined in section 6.1.1. For a linear TS case, the two eigenvalues do not significantly affect the results and either solution can be picked [4]. In crossflow cases the eigenvalues were distinctly different and presented significant differences downstream of the inflow. To reduce uncertainties, the WNL stability technique was therefore not exploited in crossflow cases and its application will be recommended as future work.

The amplitude does not affect the linear stability techniques used to introduce the modes at the first stage. Instead, the amplitudes are given to the modes afterward for both the physical wave and its complex conjugate. This completes the mode introduction. Table 4.1 summarizes the primary mode introduction scheme where WNL 1 and 2 refer to the first and second solution of the weakly nonparallel local stability equations respectively. Which one, if any, should be picked and what the effects are downstream are investigated later in section 6.1.1.

Table 4.1: Primary mode introduction techniques.

Technique	A, β, ω	α	$\hat{q}$
ILST	User input	ILST	ILST
WNL	User input	WNL 1 or 2	WNL 1 or 2.

4.3.2. Forced mode introduction

Nonlinear mode interactions can force oscillatory modes that are characterized by multitudes of the primary mode wavenumbers and frequency. These harmonics were not yet present in the system and would generally be linearly stable otherwise. The nonlinear forcing is the reason for this mode's introduction and it is thus hypothesized that these effects are non-negligible. If interactions that force this mode are expected to generate an amplitude that exceeds a user-defined threshold, it will be introduced using nonparallel nonlinear techniques.

For oscillatory modes, a similar approach is utilized that exploits the ILPSE framework. As an example, we will introduce a harmonic at an arbitrary stage i. The main problem in applying the (adjusted) PSE framework locally is that it requires an estimate for $\bar{A}_{i-1}\bar{q}_{i-1}$ and $\bar{\alpha}_i$ to solve for $\bar{A}_i\bar{q}_i$. In contrast to the marching of modes already present in the system, the amplitude is now unknown for both stages. Linear techniques, e.g. ILST or WNL, would not be able to provide any information on the amplitudes of newly forced modes. Neither would they be suitable to provide an estimate of the growth rate as nonlinear effects are ignored.

To be able to find an amplitude as well as a shape function of a newly forced mode, the amplitude will be contained in $\bar{q}_i$ and $\bar{q}_{i-1}$ in the numerical scheme. The amplitude will be found through normalization afterward, which enforces that

$$\bar{q}(\bar{x}_i, \bar{y}_m) = 1, \tag{4.1}$$

where $\bar{x}_i$ denotes the location of introduction and $\bar{y}_m$ is the location at which the shape function is maximum. Formulation 4.1 is in line with later choices to plot the amplitude of a mode as the peak amplitude. The amplitude subtracted from this normalization can be defined as

$$\bar{A}_i = \bar{q}_{\texttt{max}}(\bar{x}_i, \bar{y}_m). \tag{4.2}$$

A nonlinear estimate for $\bar{\alpha}$ is generated using the average of the wavenumbers from the mode interactions as suggested in [14]. Since this harmonic is forced in a nonlinear manner, its growth can be expected to depend on the growth of the nonlinear forcing term. The growth of which, in turn, depends on the growth of its components described by the wavenumbers. This motivates the use of the average interaction wavenumber as an

estimate for $\bar{\alpha}$.

The wavenumber, $\bar{\alpha}$, is used in the ILPSE solver to generate a streamwise dependent nonlinear shape function by describing $\bar{A}_{i-1}\bar{q}_{i-1}$ in terms of $\bar{A}_i\bar{q}_i$. Starting from the ILPSE system of equations for a stage i,

$$\mathbb{L}\bar{A}_i\bar{q}_i + \mathbb{M}\frac{\partial(\bar{A}\bar{q})}{\partial\bar{x}}\bigg|_i + \mathbb{N}\frac{\partial\bar{\alpha}}{\partial\bar{x}}\bar{A}_i\bar{q}_i = \bar{r}, \tag{4.3}$$

where both the amplitude and shape function are now present in the formulation. We can write $A_{i-1}q_{i-1}$ in terms of A_iq_i under the assumption that the shape function did not change locally over a small step $\Delta\bar{x}$. This assumption holds as the shape function is slowly varying by definition in the PSE framework. The oscillatory motion and growth of the mode are captured in the wave function. Given the estimate of α and the ansatz (3.9) of exponentially growing eigenmodes, we can write for a constant shape function $\bar{q}$,

$$\frac{\partial(\bar{A}\bar{q})}{\partial\bar{x}}\bigg|_i = \frac{\bar{A}_i\bar{q}_i - \bar{A}_{i-1}\bar{q}_{i-1}}{\Delta\bar{x}} = \frac{\bar{A}_i\bar{q}_i - \bar{A}_ie^{-\bar{\alpha}_i(-\Delta\bar{x})}\bar{q}_i}{\Delta\bar{x}} = \frac{\bar{A}_i\left(1-e^{\bar{\alpha}_i\Delta\bar{x}}\right)\bar{q}_i}{\Delta\bar{x}}, \tag{4.4}$$

by exploiting a first-order backwards Euler approximation of growth in $\bar{A}$. The step size $\Delta\bar{x}$ enters the equation for the numerical approximation of this derivative. Equation 4.4 can be introduced into equation 4.3, leading to

$$\mathbb{L}\bar{A}_i\bar{q}_i + \mathbb{M}\frac{\bar{A}_i\left(1-e^{\bar{\alpha}_i\Delta\bar{x}}\right)\bar{q}_i}{\Delta\bar{x}} + \mathbb{N}\frac{\partial\bar{\alpha}}{\partial\bar{x}}\bar{A}_i\bar{q}_i = \bar{r}, \tag{4.5}$$

where $\bar{A}_i\bar{q}_i$ is the only unknown in this equation. Equation 4.5 is named ILPSE3 and accounts for nonparallelism, amplitude history of the mode and nonlinear interactions, only neglecting shape change, which is of a significantly smaller order. Assuming that the amplitude was zero or the same as in stage i would lead to the methods ILPSE1 and ILPSE2 respectively. The use for and derivation of ILPSE2 will be presented in section 4.3.3. Assuming that the amplitude was initially zero is an approximation of the modelling found in open literature forced mode introduction and will be compared to ILPSE2 and ILPSE3 in 6.1.2. A normalization of the shape function presents us with the amplitude of this mode and ensures the shape function does not contribute to the amplitude. A summary of forced mode introduction methods one to three is presented in table 4.2.

Table 4.2: Forced mode introduction techniques.

Technique	A_{i-1}	A_i	β, ω	α	$\hat{q}$
ILPSE1	0	ILPSE1	user input	wavenumber averaging	ILPSE1
ILPSE2	A_i	ILPSE2	user input	wavenumber averaging	ILPSE2
ILPSE3	$A_ie^{-\alpha_i(-\Delta x)}$	ILPSE3	user input	wavenumber averaging	ILPSE3

The nonlinear forcing is accounted for in the right-hand side and the solution provides both the amplitude and shape function. Note that, since the shape function now results from a nonlinear method, its relative phase distribution is also physical, rather than arbitrary as is the case for linear techniques. One mode, the steady zero-mode, cannot be accounted for in the forcing as its interaction would be with the mode that is to be forced itself, which is a priori unknown. Why this interaction can be felt by the mode itself is explained in section 4.4. The mean flow distortion, however, adheres to the boundary layer equations and can be added to the base flow to end up at the local mean flow. To account for the mean flow distortion's effect on any newly introduced mode, this distortion is therefore added to the base flow. This means that its effect, in contrast to the other modal interactions, is present in the left-hand side.

4.3.3. Mean flow introduction

The Mean Flow Distortion (MFD) arises through the sum of interaction of a mode and their complex conjugate. The MFD is purely real, i.e. it has no complex conjugate, as it is not an oscillatory mode. The associated forcing term, that is the result of the aforementioned interaction of modes and their complex conjugate, is therefore also purely real. The growth rate of this mode cannot be described in terms of the imaginary part

of the wavenumber as it does not have a wavenumber. Introducing and evaluating this mode, therefore, requires some special care.

The mean flow distortion is, however, a mode that can be calculated through the same set of disturbance equations presented in 3.7, although its boundary conditions are different. The mean flow distortion has an unbounded wall-normal velocity component that represents the possibility for this mode to increase the boundary layer thickness. Its non-oscillatory behavior implies that α, β and ω are zero. This is important for later as it will complicate the mode introduction scheme presented in this thesis in section 4.3.2.

The MFD is introduced using an adapted Inhomogeneous Linear Parabolized Stability Equation (ILPSE) that is similar to the LPSE code, aside from a non-zero right-hand side that contains the forcing of this mode. For the mean flow distortion, an extra equation for the freestream condition is present as it is not constraint by a Dirichlet condition. Rather, it only adheres to continuity. Solving the ILPSE requires an initial condition, however, as the history of the mode should be accounted for. This is a problem, given that the mode was previously not present in the system, as is with all forced mode introductions. Numerically, its amplitude is cut-off to zero and no shape function is known.

The formulation for nonlinear nonparallel introduction of modes presented in equation 4.5 is inapplicable to the mean flow distortion as it does not have a wavenumber. Another option is to neglect this wavenumber effect and assume that the state of the mode was exactly the same in both cases. This means nonparallel effects of the mode are neglected, resulting in

$$\mathbb{L}\bar{A}_i\bar{q}_i = \bar{r}, \tag{4.6}$$

since all streamwise derivatives with respect to the perturbation quantities are now zero. Matrix $\mathbb{L}$ can be found in appendix A.1, although in this formulation all entries that contain the wavenumbers $\bar{\alpha}$ or $\bar{\beta}$ are zero. This system is ill-posed as a result and cannot be inverted to find a solution for the amplitude and shape function. The system is therefore solved assuming that the mode was of amplitude zero in the previous stage and the amplitude is maintained in the solution. The system that is solved for the introduction of the mean flow distortion is therefore

$$\mathbb{L}\bar{A}_i\bar{q}_i + \mathbb{M}\frac{\bar{A}_i\bar{q}_i}{\Delta\bar{x}} = \bar{r}, \tag{4.7}$$

since the streamwise derivative can be rewritten as

$$\left.\frac{\partial(\bar{A}\bar{q})}{\partial\bar{x}}\right|_i = \frac{\bar{A}_i\bar{q}_i}{\Delta\bar{x}}, \tag{4.8}$$

when the results at stage $i-1$ are assumed zero and the streamwise step size is $\Delta\bar{x}$. Forwarding the numerical cut-off as a given to the formulation results in a seemingly inevitable error that results in the amplitude of the mode being too small. The MFD now has to come up from zero, rather than evolve from a physical state in the previous stage.

The normalization condition, as explained in 3.6, cannot be applied to the MFD. The redirection of the growth into a wavenumber is impossible as the non-oscillatory zero-mode has no wavenumber. The ansatz of equation 3.9 is not broken by maintaining the amplitude in the shape function as the primary cause for rapid changes in the shape function is oscillatory behaviour and not growth. The mean flow distortion is thus never normalized and maintains the amplitude in the shape function.

4.4. Harmonic balancing

Harmonic balancing is the key to solving the NPSE that describes the evolution of all present perturbation modes. Harmonic balancing describes the wave-triad interaction of harmonics in the system. The goal of harmonic balancing is to end up with a system of LPSE's with a source term that is calculated through the nonlinear interaction of all relevant eigenmodes. Which interactions are relevant and why, will be tackled in this section.

The right-hand side of 4.3 contains the sum over all the products of the eigenmodes that appear as a source-term. It is only possible for a source term to force a spectral equivalent as sinusoidal components have to match on both sides of the equation, i.e., β and α and ω are equal. An example of this can be shown by writing out the quadruple sum of the first term in the x-momentum equation of equation 3.29. The right-hand side reads

$$-i\bar{\alpha}\bar{u}^2 - \bar{u}\frac{\partial \bar{u}}{\partial \bar{x}} - \bar{v}\frac{\partial \bar{u}}{\partial \eta} - i\bar{\beta}\bar{w}\bar{u}. \tag{4.9}$$

As an example, we consider the first term which contains a multiplication of two $\bar{u}$-components of the shape function. To be able to distinguish between the two sums of 3.26, the resulting modes will be subscripted (m,n) for their respective harmonics and the components will be subscripted (g,h) and (j,k). Rewriting the first term of expression 4.9 in this manner and omitting the $-i\alpha$ multiplication, we obtain

$$\sum_{g=-G}^{G}\sum_{h=-H}^{J}\sum_{j=-J}^{J}\sum_{k=-K}^{K} \bar{u}_{g,h}\bar{u}_{j,k}\bar{A}_{g,h}\bar{A}_{j,k}\, e^{i\left(\int_{\bar{x}_0}^{\bar{x}} \bar{\alpha}(x^*)_{g,h}dx^* + g\bar{\beta}\bar{z} - h\bar{\omega}t\right)} e^{i\left(\int_{\bar{x}_0}^{\bar{x}} \bar{\alpha}(x^*)_{j,k}dx^* + j\bar{\beta}_0\bar{z} - k\bar{\omega}_0\bar{t}\right)} \tag{4.10a}$$

$$= \sum_{g=-G}^{G}\sum_{h=-H}^{H}\sum_{j=-J}^{J}\sum_{k=-K}^{K} \bar{u}_{g,h}\bar{u}_{j,k}\bar{A}_{g,h}\bar{A}_{j,k}\, e^{i\left(\int_{\bar{x}_0}^{\bar{x}} \bar{\alpha}(x^*)_{g+h,j+k}dx^* + (g+h)\bar{\beta}_0\bar{z} - (j+k)\bar{\omega}_0\bar{t}\right)} \tag{4.10b}$$

$$= \sum_{m=g+h=-M}^{M}\sum_{n=j+k=-N}^{N} \bar{u}_{m,n}\bar{A}_{m,n}\, e^{i\left(\int_{\bar{x}_0}^{\bar{x}} \bar{\alpha}(x^*)_{m,n}dx^* + (m)\bar{\beta}_0\bar{z} - n\bar{\omega}_0\bar{t}\right)}, \tag{4.10c}$$

where x^* is an integration variable and the condition $m = g + h$ and $n = j + k$ ensures that only permutations of (g,h,j,k) that result in the mode combination (m,n) are included in the right-hand side of the equation. The shape function is thus calculated through $\bar{u}_{g,h}\bar{u}_{j,k}$ and its amplitude is the product of $A_{g,h}A_{j,k}$. As such, equation 4.10c is still a quadruple sum, though it has the additional requirement that only certain permutations contribute. This additional requirement is the essence of harmonic balancing, which states that only modes can be excited through sources operating in the same harmonic spectrum. This means that the equation can be split in a system of $(2M+1)\times(2N+1)$ inhomogeneous partial differential equations where the contributing interactions of other modes are present in a forcing term on the right-hand side. This is a key element of the design of a solution algorithm for the NPSE as it will allow us to converge to a solution instead of having to solve the combined system at once.

4.4.1. Source term selection

At every streamwise station of the NPSE marching algorithm, the amplitude of any mode currently not in the system can be estimated through an order of magnitude analysis. By first multiplying the amplitudes of the waves whose interaction would force this unrepresented mode and then summing the contributions of all those interactions, the amplitude of any mode can estimated. If the amplitude exceeds a previously determined threshold, it is concluded this mode needs to be introduced and thus a forcing term needs to be determined.

To determine which modes affect an arbitrary mode (m,n), first, a matrix is set up that contains the mode interaction results, following an interaction between modes (g,h) and (j,k). In the matrix, the resulting mode can be found that is described by $(g+j, h+k)$ as shown in equation 4.10c.

To visualize this, first, let us define a new "mode counter", l, that counts the permutations of m and n. It starts from the conjugate modes and counts up through m and n in that order. An example for the spectral domain, $\Omega = 1$, i.e. $N = M = 1$, is shown in table 4.3.

Table 4.3: Mode number, counter and mathematical notation for N=M=1.

Mode number	-4	-3	-2	-1	0	1	2	3	4
Mode count	1	2	3	4	5	6	7	8	9
$l_{m,n}$	$l_{-1,-1}$	$l_{0,-1}$	$l_{1,-1}$	$l_{-1,0}$	$l_{0,0}$	$l_{1,0}$	$l_{-1,1}$	$l_{0,1}$	$l_{1,1}$

The mode counter is important for understanding the numerical implementation of the NPSE and we will therefore use this counter in the following example.

The general formula for the total number of entries is $[2M+1] \times [2N+1]$. In this case, for $M = N = 1$, that results in a spectral domain Ω with nine permutations for possible modes. A matrix can be constructed to contain the mode that is affected by every interaction between the waves present in this roster. For this set of modes the interactions can be represented using the mode numbers from table 4.3. This results in table 4.4.

Table 4.4: Mode interactions showing modes outside of the spectral domain, Ω, in red.

	1	2	3	4	5	6	7	8	9
1	$l_{-2,-2}$	$l_{-1,-2}$	$l_{0,-2}$	$l_{-2,-1}$	$l_{-1,-1}$	$l_{0,-1}$	$l_{-2,0}$	$l_{-1,0}$	$l_{0,0}$
2	$l_{-1,-2}$	$l_{0,-2}$	$l_{1,-2}$	$l_{-1,-1}$	$l_{0,-1}$	$l_{1,-1}$	$l_{-1,0}$	$l_{0,0}$	$l_{1,0}$
3	$l_{0,-2}$	$l_{1,-2}$	$l_{2,-2}$	$l_{0,-1}$	$l_{1,-1}$	$l_{2,-1}$	$l_{0,0}$	$l_{1,0}$	$l_{2,0}$
4	$l_{-2,-1}$	$l_{-1,-1}$	$l_{0,-1}$	$l_{-2,0}$	$l_{-1,0}$	$l_{0,0}$	$l_{-2,1}$	$l_{-1,1}$	$l_{0,1}$
5	$l_{-1,-1}$	$l_{0,-1}$	$l_{1,-1}$	$l_{-1,0}$	$l_{0,0}$	$l_{1,0}$	$l_{-1,1}$	$l_{0,1}$	$l_{1,1}$
6	$l_{0,-1}$	$l_{1,-1}$	$l_{2,-1}$	$l_{0,0}$	$l_{1,0}$	$l_{2,0}$	$l_{0,1}$	$l_{1,1}$	$l_{2,1}$
7	$l_{-2,0}$	$l_{-1,0}$	$l_{0,0}$	$l_{-2,1}$	$l_{-1,1}$	$l_{0,1}$	$l_{-2,2}$	$l_{-1,2}$	$l_{0,2}$
8	$l_{-1,0}$	$l_{0,0}$	$l_{1,0}$	$l_{-1,1}$	$l_{0,1}$	$l_{1,1}$	$l_{-1,2}$	$l_{0,2}$	$l_{1,2}$
9	$l_{0,0}$	$l_{1,0}$	$l_{2,0}$	$l_{0,1}$	$l_{1,1}$	$l_{2,1}$	$l_{0,2}$	$l_{1,2}$	$l_{2,2}$

The modes presented in red are outside of the spectral domain and are thus excluded from the calculations. This part of the code is present in the function Mint.m presented in appendix B.2. In coding, however, it would be easier to split this matrix into two separate matrices. The first one, M_{mat}, contains the m of every entry and the second one, N_{mat}, contains the n of this entry.

4.4.2. Balancing

The code function, Mint.m, provided us with two matrices that contain modes affected by all possible interactions in the system. Every interaction has an amplitude that is the result of a multiplication of the amplitudes of the original modes. To find this source amplitude, all the relevant source term amplitudes are added. To find which terms are relevant, the correct combination of m and n in the matrices M_{mat} and N_{mat} has to be found.

For every mode, m and n are read from the (double) mode array. Let us take the first mode as an example, indicated by green in table 4.5.

Table 4.5: All modes for a system with $N = M = 1$ with the first mode highlighted in green.

Mode count	1	2	3	4	5	6	7	8	9
$l_{m,n}$	$l_{-1,-1}$	$l_{0,-1}$	$l_{1,-1}$	$l_{-1,0}$	$l_{0,0}$	$l_{1,0}$	$l_{-1,1}$	$l_{0,1}$	$l_{1,1}$

The first mode is a combination of $m = -1$ and $n = -1$. This means that the matrix entries must be found that contain the modes $\forall m = -1 \wedge n = -1 \in \Omega$. The modes for which this holds, are highlighted in green in table 4.6.

Table 4.6: Mode interactions for $n = m = -1$ indicated in green and showing modes outside of the spectral domain in red.

	1	2	3	4	5	6	7	8	9
1	$l_{-2,-2}$	$l_{-1,-2}$	$l_{0,-2}$	$l_{-2,-1}$	$l_{-1,-1}$	$l_{0,-1}$	$l_{-2,0}$	$l_{-1,0}$	$l_{0,0}$
2	$l_{-1,-2}$	$l_{0,-2}$	$l_{1,-2}$	$l_{-1,-1}$	$l_{0,-1}$	$l_{1,-1}$	$l_{-1,0}$	$l_{0,0}$	$l_{1,0}$
3	$l_{0,-2}$	$l_{1,-2}$	$l_{2,-2}$	$l_{0,-1}$	$l_{1,-1}$	$l_{2,-1}$	$l_{0,0}$	$l_{1,0}$	$l_{2,0}$
4	$l_{-2,-1}$	$l_{-1,-1}$	$l_{0,-1}$	$l_{-2,0}$	$l_{-1,0}$	$l_{0,0}$	$l_{-2,1}$	$l_{-1,1}$	$l_{0,1}$
5	$l_{-1,-1}$	$l_{0,-1}$	$l_{1,-1}$	$l_{-1,0}$	$l_{0,0}$	$l_{1,0}$	$l_{-1,1}$	$l_{0,1}$	$l_{1,1}$
6	$l_{0,-1}$	$l_{1,-1}$	$l_{2,-1}$	$l_{0,0}$	$l_{1,0}$	$l_{2,0}$	$l_{0,1}$	$l_{1,1}$	$l_{2,1}$
7	$l_{-2,0}$	$l_{-1,0}$	$l_{0,0}$	$l_{-2,1}$	$l_{-1,1}$	$l_{0,1}$	$l_{-2,2}$	$l_{-1,2}$	$l_{0,2}$
8	$l_{-1,0}$	$l_{0,0}$	$l_{1,0}$	$l_{-1,1}$	$l_{0,1}$	$l_{1,1}$	$l_{-1,2}$	$l_{0,2}$	$l_{1,2}$
9	$l_{0,0}$	$l_{1,0}$	$l_{2,0}$	$l_{0,1}$	$l_{1,1}$	$l_{2,1}$	$l_{0,2}$	$l_{1,2}$	$l_{2,2}$

In the code, finding the mode interaction permutations for which this condition holds, is performed separately for N and M. These matrices will have a "1" where the sum of the streamwise and spanwise wavenumber respectively, matches that of the evaluated mode. Afterward, the binary matrices are multiplied, simulating a binary AND function, leaving a "1" only if both conditions hold. This is stored in a collection of matrices, denoted "HB". The result, for this example, would thus be a $[9 \times 9]$ matrix for which all entries are "0" except for the entries at the location indicated by a green square previously: [1,5], [2,4], [4,2] and [5,1]. The function Hbalancing.m, that performs the harmonic balancing, can be found in appendix B.3.

4.5. Source term amplitude

At the first stage, modes are presented to the solver as user-defined initial conditions and their amplitudes are thus known. As they travel downstream, at every stage the amplitude at that point is initially unknown and is derived by a first order upward Euler scheme from the previous stage. The growth rate used for this extrapolation, is the imaginary part of the complex wavenumber α, i.e.

$$\ln\left(\frac{A}{A_0}\right) = \int_{x_0}^{x} -\alpha_i(x^*)\,dx^*. \tag{4.11}$$

A problem arises when a new mode is excited in the boundary layer as no initial amplitude A_0 is known. This receptivity problem is a result of the growing eigenmode model that aims to calculate growth rather than the actual amplitude. For nonlinear purposes, however, quantifiable amplitudes are necessary. This problem also arises in the mathematical formulation in the case of newly excited modes. This is even before its growth factor is known since the growth factor is dependent on the relative amplitude of the wave against the forcing term. The problem thus is equal to

$$A_{m,n}\,\mathbb{LH}\left(q'_{m,n}\right) = \sum_{m=g+h=-M}^{M}\sum_{n=j+k=-N}^{N} A_{g,h}A_{j,k}\,\mathbb{RH}\left(q'_{g,h}, q'_{j,k}\right) \tag{4.12}$$

$$\text{subject to} \quad m = g + j \quad \text{and} \quad n = h + k.$$

In this formulation the operators $\mathbb{LH}$ and $\mathbb{RH}$ represent the left-hand side and right-hand side operators respectively. The focus is on the amplitudes which is why they are not contained in the aforementioned operators. It can be rewritten to

$$\mathbb{LH}\left(q'_{m,n}\right) = \sum_{m=g+h=-M}^{M}\sum_{n=j+k=-N}^{N} \frac{A_{g,h}A_{j,k}}{A_{m,n}}\,\mathbb{RH}\left(q'_{g,h}, q'_{j,k}\right) \tag{4.13}$$

where the fraction $\frac{A_{g,h}A_{j,k}}{A_{m,n}}$ can be seen as the effective forcing. This becomes problematic for newly forced modes, as in that case $A_{m,n}$ is 0 in the numerical model due to the threshold. To solve this problem the amplitude division is not performed for new modes when calculating the forcing term. The amplitude of the new mode is derived from the maximum value of $\tilde{u}_{max}$ after solving the mode introduction system considered in more detail in 4.3.2.

4.6. Amplitude correction

In a parabolized stability framework, the shape function can vary in x. The change of the shape function is, however, not meant to capture growth. Its growth must be captured in the wave function only. As a result, a norm is required that limits the growth of the shape function for both the LPSE and NPSE frameworks as was explained in section 3.6. In a numerical scheme this condition is approximated in a converging loop and causes slight numerical errors. This can be reduced by selecting a smaller convergence threshold.

This condition, however, does not restrict the change of the maximum of the shape function, e.g., $\hat{u}_{max}$. It should therefore be remembered that using the maximum value of a shape function as a measure for the perturbation amplitude can lead to wrong results unless compensated for in the amplitude. The product of $A_i\ q_i$ is consistent for all modes, however, the shape function is expected not to have any contribution to amplitudes. Its contents should only describe the wall-normal dependency of the shape function. A redirection of amplitude should be performed.

In the NPSE, after a successful run, a correction is performed that multiplies local amplitude values by the respective peak amplitude of the normalized shape function at each respective stage. This corrections can be as large as 30% far downstream in the cases considered in this thesis and cannot be neglected. The correction, applied locally for the amplitude at a stage "i", is given as

$$A_i = A_i^{\diamond}\ |\hat{u}|_{i,max}, \tag{4.14}$$

where the $\diamond$ is used to mark the uncorrected output from the solver. The product of the uncorrected amplitude and accompanying shape function represents the total peak amplitude of this mode that is supposed to be captured entirely in A. The peak value of the corrected shape function will therefore be "1" after this redirection of amplitude. This output is consistent in the code and does not result in errors mathematically as the product of $A_i\,\hat{u}_{i,max}$ correctly describes the physical amplitude of the respective mode. It is only when directly plotting A, without this correction, that the errors become apparent.

Similarly and separately, a correction is to be made for the growth rate as it was calculated for the uncorrected amplitude. The growth rate is calculated in a step wise manner, from stage $i-1$ to stage i. The correction therefore follows a similar approach. The correction for the general sense can be found starting from the ansatz of exponentially growing modes, i.e.

$$A_i = A_{i-1} e^{-\alpha_i \Delta x}. \tag{4.15}$$

The output of the code, however, is the local uncorrected amplitude at any stage i. Since every amplitude is uncorrected for the peak amplitude of the shape function, we can write

$$|\hat{u}|_{i,max} A_i^{\diamond} = |\hat{u}|_{i-1,max} A_{i-1}^{\diamond} e^{-\alpha_i \Delta x}, \tag{4.16}$$

with α_i the corrected growth rate that is currently unknown. A correction factor can be formulated from the change in maximum amplitude of the shape function $\bar{u}$ that describes the relation between the correct amplitudes at both stages as

$$A_i = A_{i-1} e^{-\alpha_i^{\diamond} \Delta x} \frac{|\hat{u}|_{i-1,max}}{|\hat{u}|_{i,max}}, \tag{4.17}$$

where a correction factor has now appeared on the right-hand side. This correction factor is to be applied to the wavenumber and is thus rewritten as

$$A_i = A_{i-1}\ e^{-\alpha_i^{\diamond} \Delta x}\ e^{\left(\ln \left[\frac{|\hat{u}|_{i-1,max}}{|\hat{u}|_{i,max}} \right] i \right)}, \tag{4.18a}$$

$$A_i = A_{i-1} e^{-\left(\alpha_i^{\diamond} - \ln \left[\frac{|\hat{u}|_{i-1,max}}{|\hat{u}|_{i,max}} \right] \right) \Delta x}. \tag{4.18b}$$

where the term $-\ln \left[\frac{|\hat{u}|_{i-1,max}}{|\hat{u}|_{i,max}} \right] \frac{i}{\Delta x}$, is the correction applied to the growth rate for peak amplitude plotting conventions. The corrections for growth rate and amplitude are applied separately in post-processing.

4.7. Marching procedure

Parabolization of the stability equations allowed us to neglect downstream influences such that a marching scheme could be exploited to calculate the growth of presented modes. For every station separately, taking into account nonparallel effects and the result from previous stations, the NPSE are solved in a nonlinear converging loop. The marching procedure can be subdivided into four main tasks each of which contains sub-tasks as follows:

1. Initial condition
   - User-generated
   - Forced modes
2. Marching loop
   - Filtering
   - Amplitude correction
3. Convergence scheme
   - Forcing term
   - Shape functions
   - Growth rates

The initial condition and forced mode introduction was considered in section 4.3. During the explanation of the marching scheme in this section we will refer back to the respective sections for details.

Table 4.7: Newton iteration starting point for an arbitrary stage i based on convergence results from the previous stage.

Stage $i-1$ Result	Stage i estimate
$\bar{q}_{(j,i-1)}$	$\bar{q}_{(j,i-1)}$
$\bar{\alpha}_{(j,i-1)}$	$\bar{\alpha}_{(j,i-1)}$
$\bar{A}_{(j,i-1)}$	$\bar{A}_{0(j,i-1)}\, e^{-\int_{\bar{x}_0}^{\bar{x}_i} \bar{\alpha}_{i\ (j)}(\bar{x}^*)d\bar{x}^*}$

Per stage, denoted by (i), a convergence loop is run that aims to find the shape function, forcing term and growth rates for that stage through a newton iteration. The starting point of this iteration is an estimate based on the results in the previous stage, i.e. stage $(i-1)$, for all modes j in the simulation as presented in table 4.7. Note that the integral that calculates the amplitude at every stage contains the growth rate at that stage, making this an implicit scheme.

The growth rate from the previous stage is used to perform a first-order approximation of the amplitude of all the modes in the next stage initially. This growth rate is refined during the convergence loop. All other properties are initially assumed to be unchanged. Starting from this estimation, a nonlinear convergence loop is initiated. The convergence order is arbitrary and was proven not to affect results or computational speed. The most straight-forward convergence scheme that is currently in the solver, is therefore used as an example and can be seen in figure 4.3. Additional solvers that were tested were preferential in nature and aimed to converge one aspect, e.g. α, q or $\vec{r}$, of the loop first, before forwarding the results to the other two. These convergence schemes are shown in figure 4.4. For the convergence scheme shown in 4.4, the convergence measure was the same as all other simulations, i.e. the change of α in two subsequent stages had to be below a threshold. This means α was calculated for all modes, but not forwarded to the subsequent source term and shape function calculations. The primary focus of this scheme was therefore to improve the numerical stability if necessary and not computational efficiency. For the cases presented in this thesis, it had no effect.

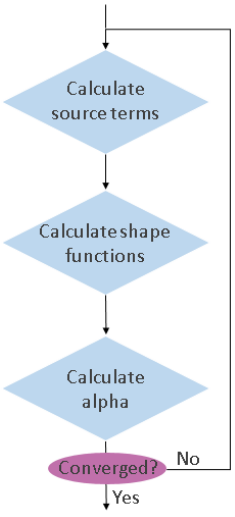

Figure 4.3: Sequential nonlinear convergence loop for the NPSE.

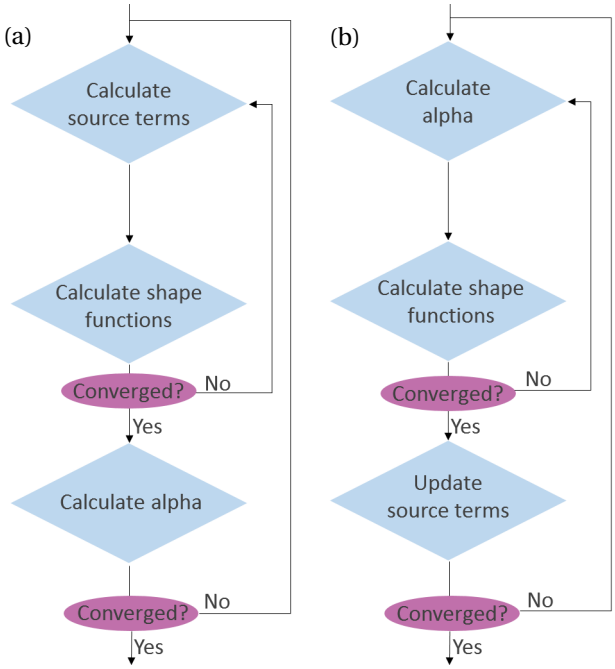

Figure 4.4: Preferential convergence schemes for (a) nonlinear terms and shape functions and (b) growth rate and shape functions.

The nonlinear convergence loop, depicted in figure 4.3, uses the initial estimate to calculate the a new forcing term, $\bar{r}$ for all modes present in the system. Using the harmonic balancing matrices from section 4.4.2, the right-hand side of equation 3.29 is calculated for every active mode using all active mode interaction permutations. The results are summed up following the summation of all modes as shown in the NPSE ansatz of 3.26. The Matlab script that performs this task is named NLT.m and can be found in appendix B.4.

Its result is forwarded to the Inhomogeneous LPSE solver that calculates a new estimate of all present shape functions, i.e. $\bar{q}_{(j,i)}$, accounting for nonlinear interactions via the source terms from NLT.m. Changes in amplitude are maintained in this solution initially. Growth is subsequently subtracted in the calculation of $\bar{\alpha}_{j,i}$. Any growth will be redirected to the complex part of this wavenumber through the normalization condition, equation 3.6. The equation's change due to the new estimation for $\bar{\alpha}$ is threefold. The new estimation for the growth changes the amplitude of the modes after integration, the contents of $\mathbb{M}$ and $\mathbb{N}$ from equation 3.30 change and the right-hand side of the NPSE (equation 3.27) is also dependent on the estimation of $\bar{\alpha}$. The calculations are repeated until the change in the growth rate of all modes falls below a user-determined convergence threshold.

4.7.1. Symmetry

The NPSE has a symmetry plane Y-Z for both a Blasius boundary layer flow and a spanwise invariant crossflow boundary layer. Every oscillating mode, that excludes the mean flow distortion, is accompanied by an equal and opposite mode that is its complex conjugate [16]. This follows from the description of sinusoidal modes using complex exponential powers, e.g.

$$\cos\phi = \frac{e^{i\phi} + e^{-i\phi}}{2}, \tag{4.19}$$

with ϕ an arbitrary argument. The wavenumbers thus are negative for the complex conjugates imposed at the inflow. The nonlinear PSE ansatz, presented in equation 3.23, thus includes modes that carry a negative wavenumber to represent these complex conjugates. For the negative wavenumber mode, all mode interactions that nonlinearly force this mode are the negative counterpart of the modes that force the real mode. This symmetry can be seen in the harmonic balancing matrix presented in table 4.6 where either side of the upward diagonal, that displays the mean flow distortion forcing, shows the equal and opposite forcing of the modes and their conjugates.

The equal and opposite forcing results in the same growth rate for the complex conjugate. Since the growth rate is equal to its physical counterpart, it is not necessary to subject this mode to the same numerical process. The total computation time can be reduced to approximately half when the conjugate modes' evolution is mirrored from its physical counterpart. Therefore, instead of treating conjugates as any other mode, it is calculated by mirroring its physical counterpart.

4.8. Solver limitations

The previously described solution algorithm is subject to physical and numerical limitations. It is important to know the limitations and modeling assumptions of the tool beforehand so that the tool can be used appropriately.

The NPSE equations assumed the following flow and perturbation properties:

1. The base flow is steady and known.
2. The base flow and shape function are slowly varying in the streamwise coordinate x. This allows for the parabolization of the stability equations.
3. The base flow is spanwise invariant and thus β is real; Growth only occurs in the streamwise direction.
4. Disturbances develop in streamwise direction and do not grow as a function of time at any fixed location. This is the case for convectively unstable wall-bounded shear layers [13].
5. Compressibility effects are negligible.
6. Temperature effects are negligible.
7. Curvature effects are negligible.

Neglecting curvature effects does not induce any errors in this case as the crossflow is generated on a flat plate. When comparing with experiments, however, the result could significantly differ as shown by Haynes and Reed [14]. In the future, to ensure accuracy when comparing with experiments, its effect should be included.

Solving the NPSE is performed through marching which is allowed after parabolization. However, marching with a too small spatial step ($\Delta x_{\min} > |\alpha_r|^{-1}$), results in residual ellipticity making the system ill-posed [23]. The solver is therefore limited in spatial resolution. In addition, the use of a marching solution limits the physical modeling of the PSE framework. The solver does not simulate a wave traveling through the boundary layer as it does not consider the passing of time. Rather, it is able to calculate the growth for a set of disturbances, given that this set is present at the same instance while interacting with each other and the base flow. It is therefore inherently assumed that the waves in this set, or packet, coexist at certain stages in the boundary layer.

Breakdown to turbulence is preceded by three-dimensionality and growth of secondary disturbances [26]. An NPSE simulation does not capture either of these phenomena and thus the code can only accurately predict nonlinear growth of primary instabilities until these effects start to affect the present perturbations significantly. The breakdown occurs rapidly [12] and therefore the NPSE are a viable tool for nonlinear transition prediction.

5

Problem description

This chapter describes the flows to which the NPSE solver will be applied. First, a Tollmien-Schlichting (TS) case will be presented that is imposed at the inflow of a Blasius boundary layer on a flat plate. Afterward, a case is shown in which the application of the NPSE is tested for the prediction of nonlinear crossflow instability growth.

5.1. Tollmien-Schlichting wave development

This study aims to validate the developed NPSE solver through the simulation of a Tollmien-Schlichting wave and its harmonics. The TS wave is characterized by the nondimensional frequency F = 86(e-6), defined as

$$F = \frac{2\pi f \nu}{U_0^2}, \tag{5.1}$$

by Bertolotti et al. [4]. This TS wave is superimposed on a Blasius boundary layer on a flat plate. The flow over this flat plate is characterized by the global Reynolds number defined at the inflow of $Re = 400$ following equation 2.2 for a kinematic viscosity of $\nu = 1.5188 \times 10^{-5} [m^2/s]$. The initial amplitude for this mode is defined by its peak velocity in the streamwise direction with respect to the freestream value, U_0 at the inflow. The peak amplitude u'_{max} for the primary mode is 2.5% of U_0. Note that this is the amplitude of the physical wave and that, in nonlinear simulations, half of this amplitude is presented to the real mode and half is presented to its complex conjugate.

All simulations for this flow will be solved on a grid with the discretization presented in table 5.1. The boundary layer is also generated on this grid via the tool that solves the discretized boundary layer equations, see [19].

Table 5.1: Dimensional discretization parameters for the NPSE simulation of a TS wave (F=86) and harmonics.

Parameter	$H\,[m]$	$y_i\,[m]$	$ny\,[-]$	$x\,[m]$	$nx\,[-]$	$\Omega\,[-]$
Value	0.06	0.0012	70	[0.243, 1.51]	185	5

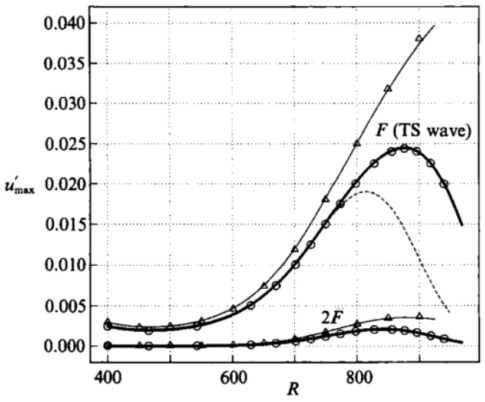

Figure 5.1: TS wave and second harmonic amplitude evolution from [4].

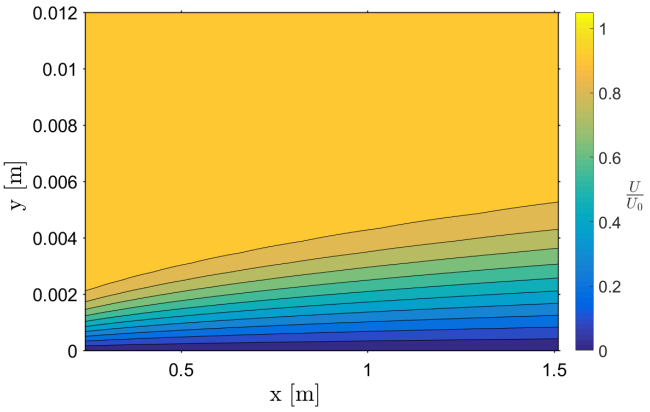

Figure 5.2: Laminar two-dimensional Blasius boundary layer base flow from [45].

Bertolotti presented the linear and nonlinear growth for this case in [4]. This can be seen in figure 5.1 alongside the base flow for this case in figure 5.2. In addition to the results from Bertolotti, Chang et al. [8] performed NPSE and DNS on the same flow and arrived at different results. Chang's results are graphically represented on a semi-logarithmic scale, see figure 5.3, which complicates a visual comparison. Chang et al. performed the simulation in two ways that either allowed a wavenumber update or locked the relative phase of harmonics and proved that differences are small. In their simulation, however, the primary mode reached a greater amplitude compared to Bertolotti's simulation [16]. The extent of this difference will become clear when comparing different initial conditions to match the results presented in the literature in section 6.1.

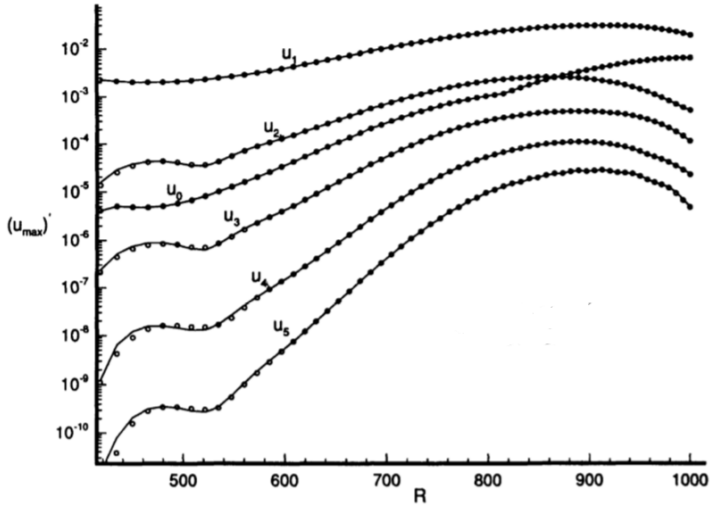

Figure 5.3: Nonlinear TS wave evolution of a fundamental two-dimensional wave characterized by $F = 86(10^{-6})$ in an incompressible Blasius boundary layer for harmonics one to five and the zero-mode with lines showing phase-locked results and symbols include a wavenumber update.

Both Bertolotti's and Chang's results were validated via a DNS and both NPSE's matched their respective DNS accurately. This indicates a systematic difference between the two simulations. It is hypothesized that the cause of this difference is present in the initial condition. The accuracy of the initial condition is crucial for providing physical results both for NPSE and DNS. This case will therefore serve two purposes. Besides being able to validate the implementation of the code through this case, an investigation into the importance and correctness of different initial conditions will be conducted.

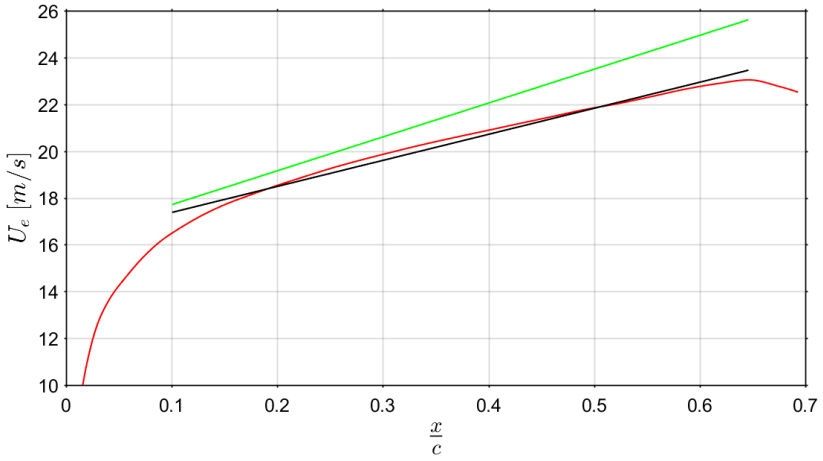

Figure 5.4: Spline interpolated external velocity distribution of the M3J wing (red), first-order polynomial fit (black) and adjusted linear distribution (green).

5.2. Crossflow wave development

After a validation of the NPSE implementation for TS waves in two-dimensional boundary layers, we can extend its application to cross flow boundary layers. This case will not be validated with open literature as no reproducible results are presented for a crossflow case. Instead, results will be validated by convergence studies and a DNS.

Serpieri [43] adjusted a NACA 66018 laminar airfoil to have the position of maximum thickness, delayed to after $\frac{x}{c} = 0.6$. This new symmetric airfoil is named the "66018M3J", or "M3J" for short. The M3J features a favourable pressure gradient up until the point of maximum thickness to suppress the growth of Tollmien-Schlichting instabilities.

Starting from the M3J pressure distribution, an external velocity distribution was derived. Due to the ongoing research in performing a DNS of this flow, we are limited to a linear distribution of the external velocity. In addition, using a linear distribution over the raw data allows for a comparison in the future with other NPSE codes. Since the NPSE are very sensitive to small changes [16], a polynomial external velocity distribution helps reduce the uncertainty in boundary conditions.

A direct first-order polynomial approximation of the velocity distribution was not unstable enough for NPSE simulations. As a consequence, to observe a more significant growth and nonlinear interactions of stationary CFI's, the linear distribution was altered by increasing the streamwise dependency and setting a 30% stronger velocity gradient. The receptivity problem is out of the scope of this thesis. As a result, the external velocity is only given from $\frac{x}{c} = 0.1$ such that simulations can be initiated at a finite amplitude, though still small enough to introduce the primary mode with linear stability techniques. A comparison between the external velocity of the M3J, the first-order polynomial and the adjusted polynomial are presented in figure 5.4.
The linear dependency of the external velocity distribution, $U_e(x)$, is given by:

$$U_e(x) = 16.08x + 16.26, \tag{5.2}$$

in meters per second and x in meters. This polynomial is presented in dimensional quantities as base flow simulations are often performed dimensionally since some normalization parameters, e.g. δ_0, can only be derived after the base flow is known. Afterward, results are nondimensionalized for stability calculations. This polynomial was derived from the M3J airfoil present at the Delft University of Technology (DUT). Therefore a scaling is often used that is based on the chord length of that airfoil $c = 0.9[m]$. The spanwise velocity is constant as this concerns a spanwise invariant simulation and equal to the inflow streamwise velocity, i.e. $W = 17.71[m/s]$. This case results in a base flow that is the boundary layer on a flat plate as shown in figure 5.5.

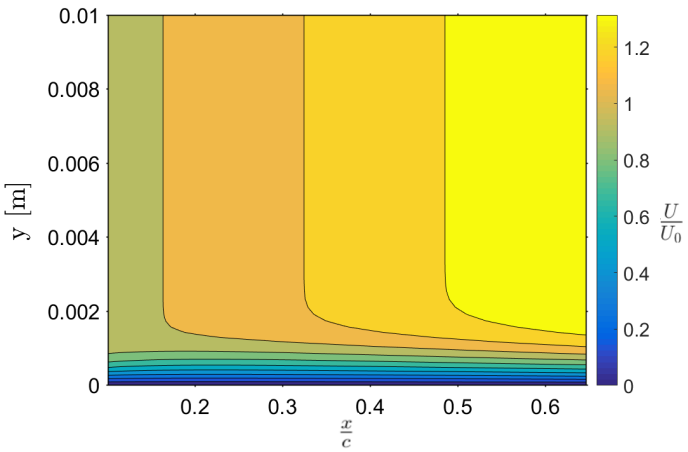

Figure 5.5: Streamwise velocities of the crossflow boundary layer normalized by the freestream velocity at the inflow $U_0 = 17.71[m/s]$.

A stationary crossflow mode is presented at the inflow of this base flow that has a spanwise wavelength of $\lambda_z = 7[mm]$ in spanwise direction. The spanwise wavenumber for this wave, when normalized by $\delta_0 = 2.79 \times 10^{-4}[m]$, the Blasius length at the inflow of the domain, is $\bar{\beta} = 0.2502$, where the bar denotes a nondimensional quantity. All crossflow simulations, aside from the simulation in comparison with the DNS and convergence studies, were performed using the numerical setup presented in table 5.2. The initial peak streamwise amplitude of the primary mode is 3.5‰of the freestream velocity at the inflow $U_0 = 17.71\ [m/s]$. The spectral domain Ω for convergence tests was taken as five, whereas for the DNS comparison eight harmonics were simulated.

Table 5.2: Dimensional discretization parameters for the NPSE simulation of a stationary crossflow instability and harmonics.

Parameter	$H\ [m]$	$y_i\ [m]$	$ny\ [-]$	$x\ [m]$	$nx\ [-]$	$\Omega\ [-]$
Value	0.02	0.002	80	$[0.09, 0.5850]$	275	$5-8$

5.2.1. DNS

For the crossflow case, a three-dimensional DNS will be performed to validate the results. Additionally, a two-dimensional DNS featuring a spanwise velocity component will be performed to provide the NPSE base flow. A DNS base flow is used to exclude the effects of boundary layer equation assumptions in the NPSE. The DNS is capable of resolving the discretized NS equations without relying on the assumptions of the NPSE framework. Therefore, it can provide us with detailed reference data of the instability growth and the nonlinear interactions between modes.

The spanwise invariant base flow and three-dimensional transitional DNS of the crossflow case are performed with the finite-volume method INCA, see [17, 33]. The streamwise domain was previously presented in section 5.2. All DNS and the NPSE for this comparison were performed with a domain height of $H = 0.0198[m]$. The DNS base flow was interpolated for NPSE purposes at 275 linearly spaced streamwise locations. In wall-normal direction, 70 Chebyshev collocation points were used with the median, y_i, at $0.1H$. It was confirmed that the top boundary condition does not affect the DNS or NPSE results through inspection of the mean flow distortion wall-normal velocity profile. The three-dimensional DNS grid contains 300 blocks and is composed of 7×10^6 hexahedral cells guaranteeing $y^+ < 1$ at the wall. The spanwise domain is discretized in 36 cells, allowing for sufficient spanwise harmonic resolution. Although convergence was not proven for the DNS, this grid is sufficient to capture the relevant flow physics and resolve the linear and nonlinear growth of eigenmodes for this case. Matching results were obtained when comparing the results of DNS and NPSE in the linear amplification stage.

In INCA, the incompressible NS equations are marched in time with a third-order explicit Runge-Kutta method [7]. A fifth-order upwind scheme was used for the calculation of the convective terms. A Falker-Skan-Cooke boundary layer profile based on the local pressure gradient is imposed at the inflow. At the outflow, total pres-

sure is prescribed. The spanwise boundaries are periodic. The top boundary condition is assigned a static pressure and velocity is extrapolated such that velocity fluctuations are damped.

A local ILST solution is presented at the inflow for the three-dimensional DNS. All other harmonics are not imposed at the inflow. To test the effect and accuracy of forced mode introductions, a second transitional DNS is performed where the second harmonic is imposed at the inflow boundary as well. This second harmonic is calculated in the NPSE at the second stage and is extrapolated upstream via the assumption present in its calculation as shown in equation 4.5 to arrive at the correct amplitude at the inflow.

6 Results

This chapter provides and analyzes the results from the application of the discretized NPSE framework to a Tollmien-Schlichting wave (F=86) superimposed on a Blasius boundary layer to validate the solver and investigate the importance of mode introductions. Following the validation in the Blasius boundary layer, a stationary crossflow simulation is performed that is subjected to a convergence study and will be compared to DNS results. The section concludes with a recap of numerical developments made in this thesis.

6.1. Tollmien-Schlichting instability case

The nonlinear simulation of a TS wave and its harmonics serves as a reference case for the NPSE solver as well as an investigation in the importance of mode introductions. All simulations were performed with discretization as described in section 5.1 and only mode introduction techniques were varied.

The perturbation at the inflow consists of a primary TS mode and its complex conjugate with a nondimensional peak amplitude of $\bar{u}'_{max} = 0.00125$ such that the physical wave has an initial amplitude of $\bar{u}'_{max} = 0.0025$. All other modes are forced nonlinearly from this initial perturbation during the marching procedure. Multiple nonlinear simulations were performed with varying initial conditions and forced mode introduction schemes. Results will be compared with results available in the open literature ([4, 8]) to validate the tool.

The simulation of TS wave characterized by $F = 86(10^{-6})$ in a Blasius boundary layer was performed by both Bertolotti et al. [4] and Chang et al. [8], although their results do not agree. Herbert states that results from Chang et al. present a greater maximum amplitude of the primary mode and that finding agreement between different PSE codes for virtually the same case is hard as the framework is sensitive to small changes [16]. This fact is amplified for amplitude-growth curves where differences are accumulated. Multiple simulations were performed with varying initial conditions and mode introduction techniques to determine the difference between the two codes until both cases found in the literature could be matched closely. The effect of the initial condition on downstream results will be discussed in more detail later in this section.

Our approximations of the reference results for the TS case are shown over the results from Chang et al. and Bertolotti respectively in figures 6.1 and 6.3.

A close match was achieved with the results of Chang et al. as presented in [8] in terms of primary mode evolution away from the inflow. Mean flow distortion growth is also comparable in this region. At the inflow and far downstream, differences are most apparent. Counter-intuitively, however, the results match more closely downstream of the inflow, than at the introduction itself indicating that nonlinear forcing was able to correct the introduction errors following direct or indirect primary mode forcing. The NPSE marches a solution and can therefore only compensate errors in the dimension of that marching. Still, the results converge around $Re = 630$. The primary mode is, at this point, not affected by nonlinear interactions. An overestimation of the amplitude of a harmonic slightly downstream of the introduction as a result of overshoot reduces the effect of nonlinear forcing, as shown in section 4.5. This results in a match of the amplitudes away from the effect of introductions. The NPSE might therefore be more robust than initially thought, although further testing is required with multiple mode introduction schemes and amplitudes to test this hypothesis.

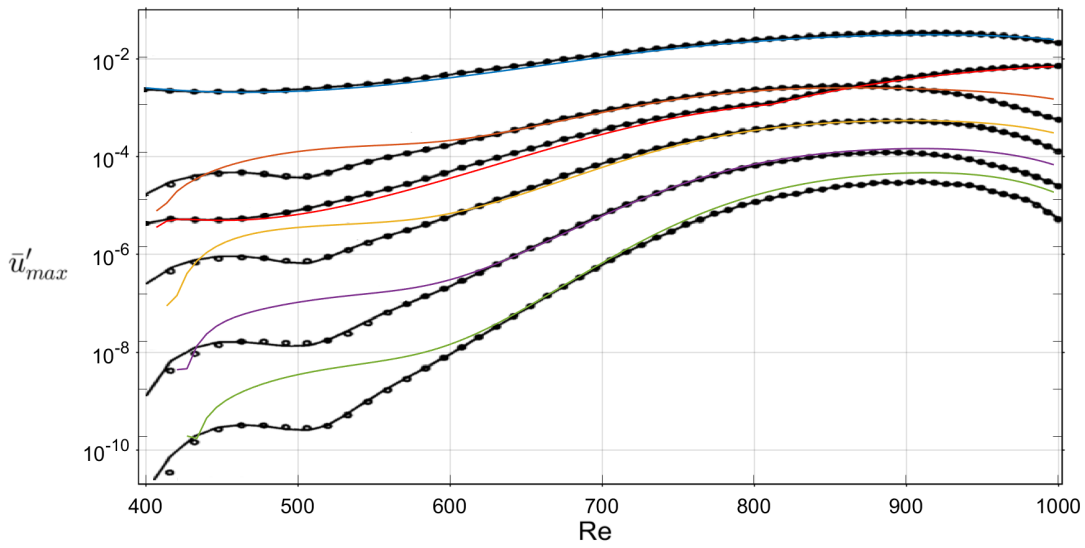

Figure 6.1: Comparison of the f86 wave evolution with Chang et al. from [8] of the harmonics 1 (blue), 2 (orange), 3 (yellow), 4 (purple), 5 (green) and mean flow distortion (red).

The deviation from the reference increases for higher harmonics both at the inflow and when $Re > 900$. A small difference in the primary mode results in a relatively large mismatch of the higher harmonics. Semi-logarithmic plotting in the y-axis visually amplifies the difference in the results as well.

Forced modes in this simulation were initiated using ILPSE1 that accounts for nonlinear forcing and assumes that the previous amplitude was exactly zero, with an initial guess for the wavenumber and growth rate of forced modes from ILST instead of wavenumber averaging. The growth rate presented by linear stability techniques for higher harmonics is stable from the third harmonic up as shown in figure 6.10 which might not represent the nonlinear stability. The importance of forced mode introduction techniques is examined in section 6.1.2. The numerical scheme for forced mode introduction is not presented in [8] and a more accurate match around the introduction could not be achieved. Using ILPSE1 initialization with a zero amplitude assumption, however, shows a similar behavior at the inflow and comparable results in terms of primary mode and mean flow distortion amplitude sufficiently far from the introduction.

The mean flow distortion experiences a discontinuity in the growth rate that appears out of place given the smoothness of the other modes. This occurs at local Reynolds number of $Re = 815$. The reason for this, is a jump in the peak that is being tracked. The shape function of the mean flow distortion contains two local maxima. One maximum overtakes the other at this local Reynolds number. The peak that is tracked after $Re = 815$ grows at a faster rate and this results in a discontinuity in the growth of the mean flow distortion. Continuity in the amplitude is not broken since the jump must occur when both peaks are of approximately equal amplitudes. A contour of the streamwise velocity of the mean flow distortion and the jump are shown in figure 6.2.

The results change significantly when, instead of ILST, a weakly nonparallel stability technique is exploited for the introduction of the primary mode. Its application to the case results in a wave growth as shown by Bertolotti et al. in [4] presented with our results when a direct solution of the WNL equation for primary mode introduction is used in figure 6.3. Forced modes for this analysis are again initiated with ILPSE where a zero amplitude assumption is made for the stage before introduction.

Since the two references for this case used either logarithmic or linear plotting, the differences are not immediately apparent. Therefore, figure 6.4 shows the approximations of their results from the current NPSE code using ILST or WNL initial conditions for comparison purposes. The difference in maximum amplitude is clearly visible now as the peak amplitudes are $\bar{u}'_{max} = 0.024$ and $\bar{u}'_{max} = 0.027$ respectively for the WNL and ILST initial condition. A similar difference can be seen in the second mode and the mean flow distortion

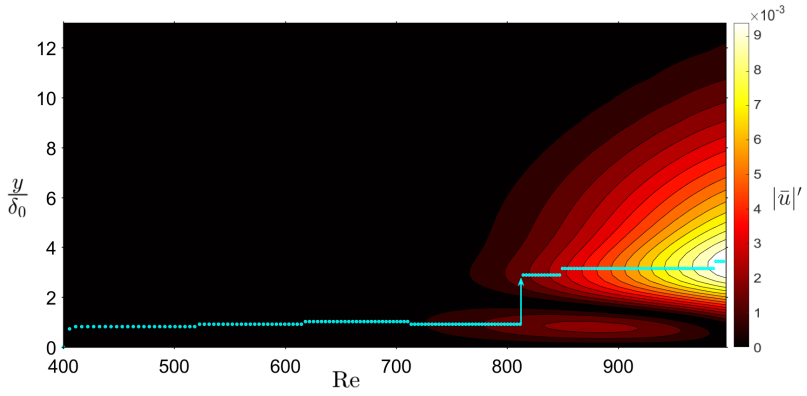

Figure 6.2: Absolute streamwise velocity component of the mean flow distortion contour with cyan dots indicating the peak value location and the arrow indicating its jump.

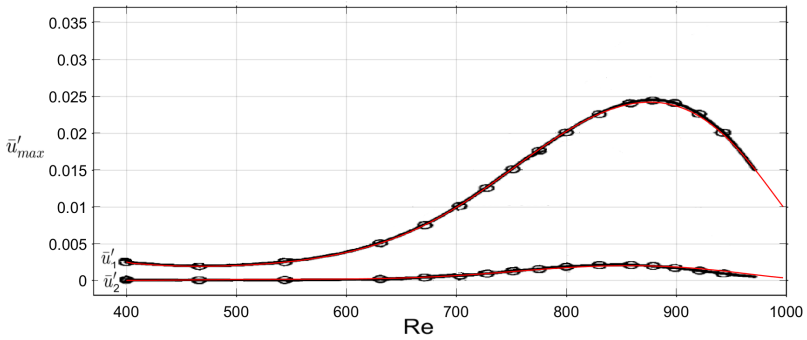

Figure 6.3: Comparison of the Tollmien-Schlichting wave evolution with Bertolotti et al. from [4] (black) and the present code (red) of the primary mode u'_1 and the second mode u'_2.

that are both relatively following WNL primary mode introduction. Nonlinear effects drive the primary mode to a greater amplitude in the Tollmien-Schlichting case with respect to the linear result, see [4]. A relatively smaller amplitude thus be caused by either linear differences or when the harmonics are forced at smaller amplitudes. In addition to the difference in peak amplitude value, the peak location is also slightly different. The peak after ILST introduction occurs roughly at $Re = 875$, whereas the peak amplitude for the ILST introduction occurs at $Re = 895$. A smaller amplitude after WNL introduction is to be expected given the lower amplitude of the harmonics and mean flow distortion and vice versa. From the results so far, it is unclear what the cause was. This will, therefore, be analyzed in section 6.1.1.

The Tollmien-Schlichting wave propagation through a Blasius boundary layer is a case with well-defined boundary conditions. Differences in the NPSE marching algorithm, e.g. the convergence order and data handling, were tested and do not affect the results. The difference between the codes was thus hypothesized and proved to be present in the scheme used for the introduction of modes.

Herbert [16] presents a weakly nonparallel local stability technique (WNL). This eigenvalue problem can be used to introduce modes in a linear nonparallel fashion whereas ILST appears to have been used in the case of Chang et al., although no mention beyond the use of "linear" techniques can be found in [8]. Two simulations were performed using an initial condition based on either ILST or WNL for the primary mode. The introduction of this mode is crucial as all other modes are forced directly through this mode within the first few stages of the simulation. The PSE framework, in addition, prevents fast changes which means that the primary mode as it follows from the introduction is used to generate the harmonics. Accuracy in primary mode introduction is therefore crucial. A seemingly small difference can change the resulting amplitudes in the system significantly. We will investigate the effect of primary mode and forced mode introductions for this case separately in sections 6.1.1 and 6.1.2.

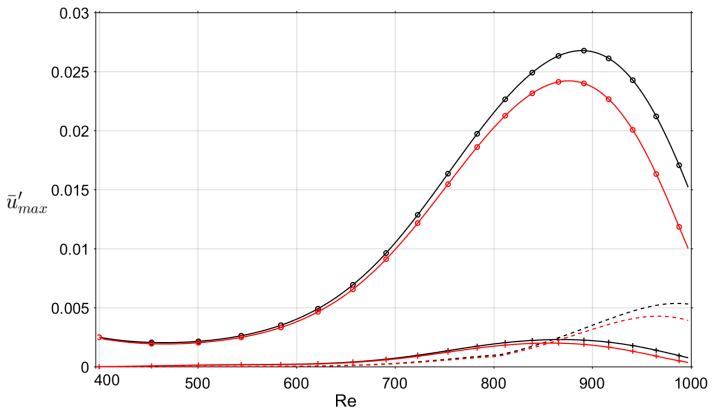

Figure 6.4: Comparison of the Tollmien-Schlichting wave evolution of the first harmonic (o), second harmonic(+) and mean flow distortion (–) using either ILST (black) or WNL (red) primary mode initial condition.

6.1.1. Primary mode introduction

To isolate the effect or primary mode introduction, two studies will be performed. A linear study that aims to see if the linear evolution of the primary mode is affected by the introduction technique and a nonlinear study that aims to quantify the result of harmonic introduction through forcing with different primary modes. The following study will introduce all forced modes with the assumption that the amplitude at the stage before the introduction was precisely zero to remain consistent with the references, i.e. [8] and [4]. Only the primary mode introduction is varied between ILST and WNL.

Although the primary mode is severely affected by other modes in the nonlinear regime, the amplitude evolution is still comparable to the linear trend. The strength of nonlinear interactions affects the peak amplitude value and its streamwise location. To test whether the difference between the simulations is a linear or nonlinear effect, or a combination of the two, LPSE simulations were performed using either ILST or WNL introductions. The results are shown in figure 6.5. The results are shown to deviate also in a linear sense. However, the opposite effect can be seen as linearly both of the WNL introductions result in greater amplitudes than the simulation following an ILST inflow perturbation. The results from either of the weakly nonparallel initial conditions differ. Figure 6.5(b) shows the initial difference from the different eigenvalues from the WNL solution that is the result of the stable or unstable extrapolation from the first stage. The results for the LPSE starting from either WNL solution are similar downstream of the introduction, as was found by Bertolotti et al. [4]. The eigenvalues from the WNL solution, however, do not appear physical and show completely different behavior. In addition, a transient is seen in both cases near the inflow whereas the ILST result provides a smooth curve with an initial growth rate that is in line with the subsequent stages.

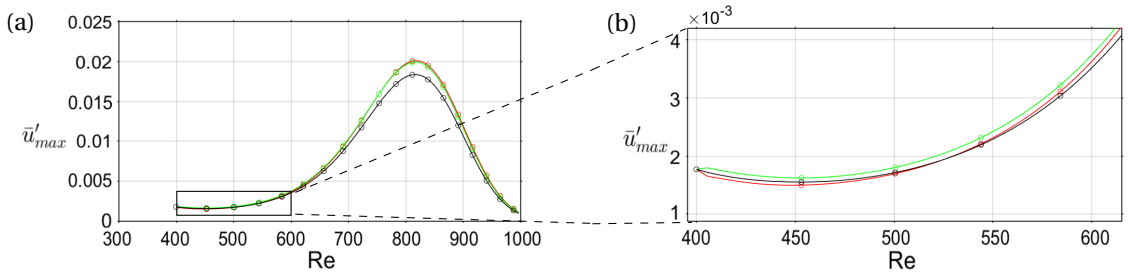

Figure 6.5: Linear evolution of a TS wave (F=86) after introduction by ILST (black), the stable solution to WNL (red) or the unstable solution to WNL (green).

The WNL solution is found directly through equation 3.36. This formulation is physically more accurate than a mode introduction using ILST, as it includes nonparallel effects of the base flow and the shape function. Uncertainty in the WNL simulation, however, originates from the eigenvalue duality in the results from direct solutions. The eigenvalue spectrum for the initial condition is shown in figure 6.6. The duality in the eigen-

values for the WNL introduction is a result of the additional eigenvalue presented for streamwise derivatives. This duality, however, also occurs for the TS mode. The selected eigenvalue for the ILST introduction is accompanied by two WNL solutions that show different behavior. One eigenvalue is stable, while the other is unstable. This is shown in figure 6.5(b) where the WNL solutions grow or decay in the first stage as a result of this introduction. It is hypothesized that neither of the eigenvalues and corresponding eigenfunctions are physical as a result of neglecting $\frac{\partial \alpha}{\partial x}$ and smaller order streamwise derivatives. When finding a direct solution of the WNL stability problem, two equations, rather than one, are solved for $\zeta = 0$ and $\zeta \neq 0$, see equations 3.35a and 3.35b respectively. The additional equation is required since also the streamwise derivative of the eigenfunction is now an unknown resulting in an additional solution to the system.

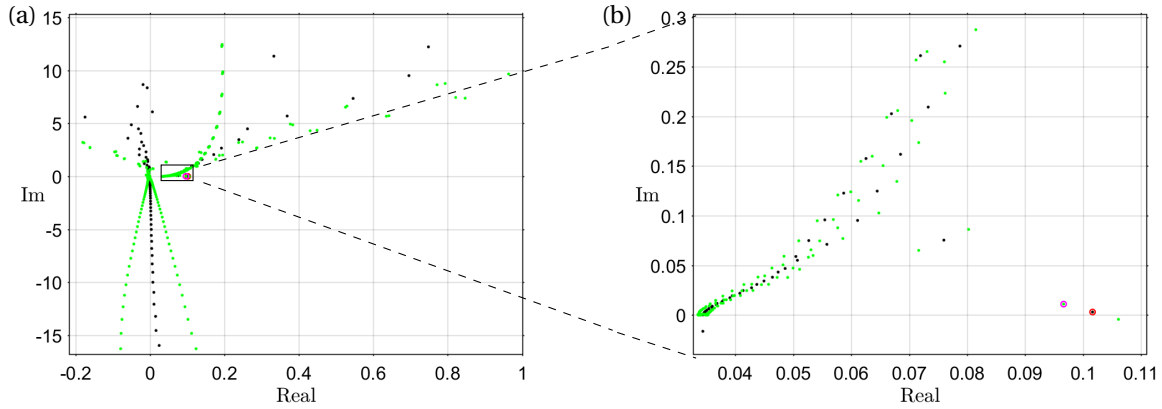

Figure 6.6: Eigenvalue spectrum from WNL (green) and ILST (black) introduction methods with selected eigenvalues for WNL (magenta) and ILST (red).

From the linear results, it was hypothesized that using the unstable eigenvalue solution from the WNL solution would create a significantly greater maximum amplitude of the primary mode in a nonlinear simulation. This would occur since harmonics are introduced at a higher harmonic and generate stronger nonlinear interactions with the primary mode. An additional NPSE simulation was therefore performed using the unstable WNL solution. It can be compared to the reference results presented in [4] and the stable WNL solution in figure 6.7. This simulation proved the hypothesis that the linearly stable or unstable initial condition affects the introduction of harmonics enough to see significant differences downstream. This in spite of the linear results converging over the same streamwise distance as was shown in 6.5(a).

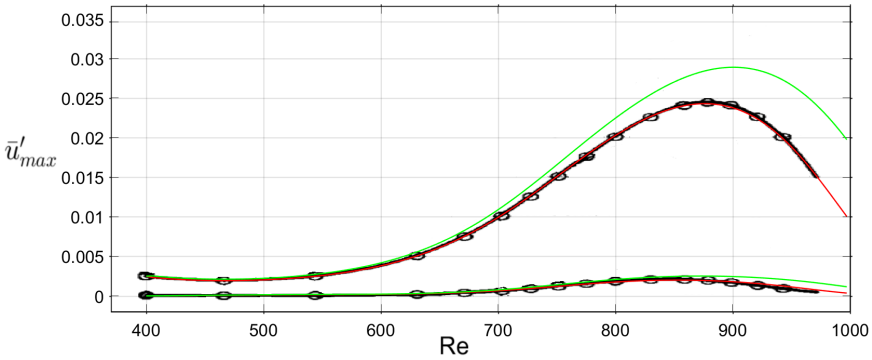

Figure 6.7: TS wave and second harmonic evolution for the stable (red) and unstable (green) solution to the WNL and results from Bertolotti et al. ([4]) (black) .

The transients found in the amplitude evolution graphs should be visible in the wavenumber evolution of the primary mode following ILST or WNL initial conditions. The number of variables was reduced to one: the primary mode introduction technique. Wavenumber averaging was used to determine the α of harmonics. Note that this case, therefore, does not match that of Chang et al. in 5.3 as, to match that case, forced modes were given a wavenumber that followed from linear stability. The wavenumber evolution of the primary mode and its harmonics as a result of using either ILST or WNL for initial mode introduction show no

significant difference for all harmonics. The growth rate and real part of the wavenumber of harmonics one to four can be seen in figure 6.8 and 6.9 respectively. It should be noted that, although no differences are clearly visible away from the inflow in these results, the amplitude can be significantly different due to the integral growth calculation where differences accumulate. The results following a WNL introduction of the primary mode show an initial transient that is corrected in the PSE march within the first four steps. In an NPSE simulation, errors accumulate and harmonics are forced after the first step. The WNL eigenvalue that was used for the nonlinear simulation in the NPSE was shown in 6.6. This eigenvalue is stable and the amplitude of the primary mode is therefore reduced in the first step, see figure 6.5. As a result, in the nonlinear simulation, all harmonics are introduced at a slightly lower amplitude. Since all harmonics are introduced at this lower amplitude, the nonlinear forcing term does not compensate for this. Amplitudes are therefore relatively smaller with respect to ILST introduction and this reduces the strength of nonlinear interactions initially and downstream of the inflow that would otherwise increase primary mode amplitude. Consequently, the nonlinear amplitude following a WNL introduction is slightly smaller than that of the primary mode following an ILST introduction.

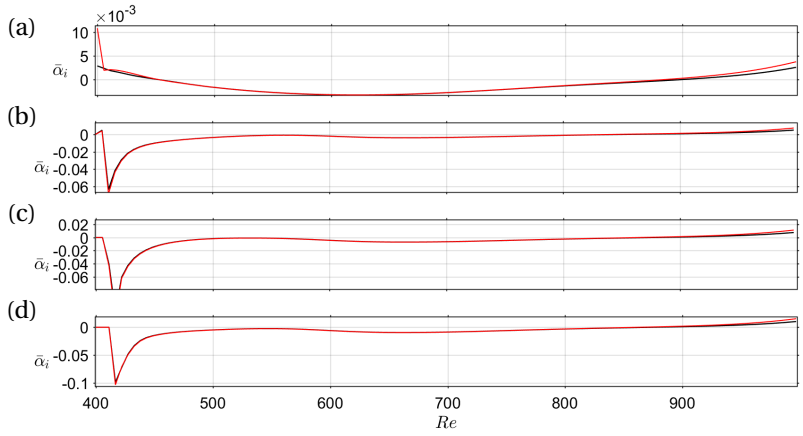

Figure 6.8: Growth rates after introduction with ILST (black) or WNL(red)for the primary mode and wavenumber averaging for forced modes with circles denoting discrete stages of the (a) first harmonic, (b) second harmonic, (c) third harmonic and (d) fourth harmonic.

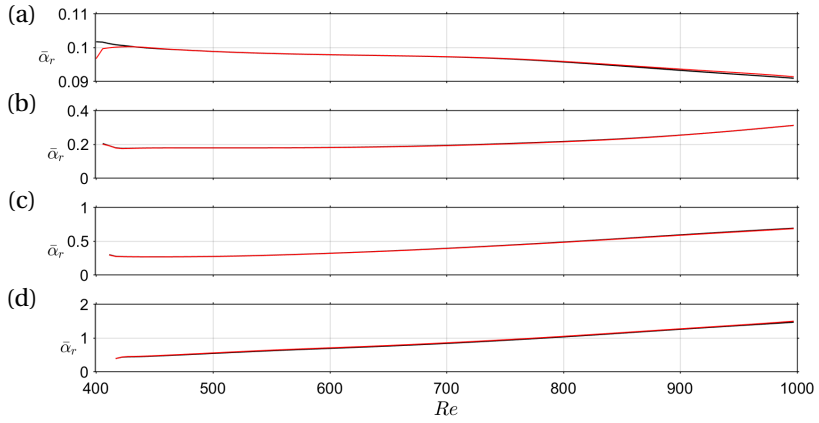

Figure 6.9: Streamwise wavelength after introduction with ILST (black) or WNL(red) for the primary mode and wavenumber averaging for forced modes with circles denoting discrete stages of the (a) first harmonic, (b) second harmonic, (c) third harmonic and (d) fourth harmonic.

The uncertainty in the results from weakly nonparallel introduction techniques lead to the use of ILST for primary mode introductions in the stability analysis of crossflow instabilities in this thesis.

6.1.2. Forced mode introduction

No effects of forced mode introduction schemes can be seen from the previous analysis as the reference cases were approximated with identical forced mode introduction schemes. Nevertheless, an observation can be made while looking at the results that used this introduction method. The primary mode for this case is initially stable while the higher harmonics are introduced in an unstable state. The stable primary mode and the fact that growth for higher harmonics is fully dependent on nonlinear forcing from the interactions of other modes would indicate that all modes should be stable as well. Otherwise, the modes should follow the linear stability indicated by the markers in figure 6.10 respectively. Despite the introduction technique used, the linear stability does not hold for any of the forced modes at any location in the previous simulations, since in the case of higher harmonics, their amplitude is of the same order as its forcing. The often called "linear regime" thus only refers to the state of the primary mode, while simultaneously all higher harmonics behave nonlinearly.

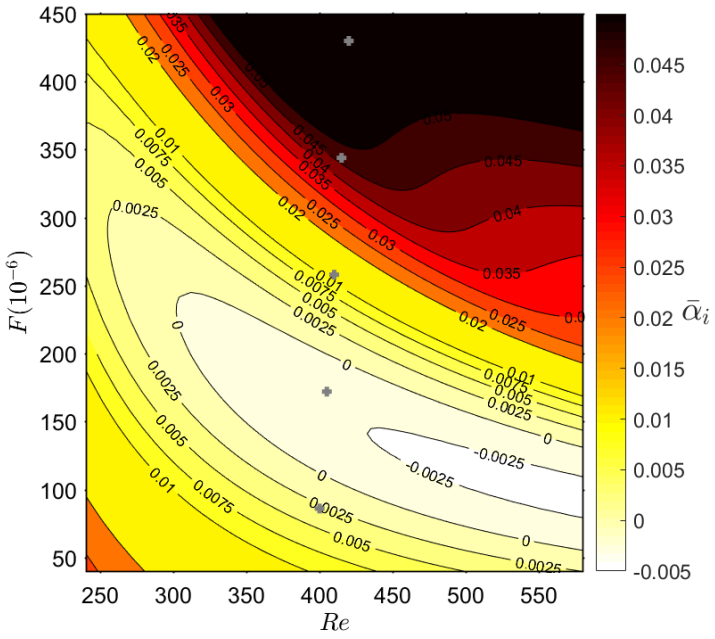

Figure 6.10: Linear stability of the Blasius boundary layer for TS waves. Contourlines indicate growth rates with markers (+) indicating the frequency and local Reynolds number at the introduction of harmonics.

We can say with certainty that correctly introduced modes for this case should be stable following the primary mode's stability. The forcing of harmonics follows the amplitude of the primary mode, which is stable and thus decreasing. Therefore, the harmonics should also be stable. Thus, rather than having a zero amplitude at the stage before the introduction, they should have had a greater amplitude prior to introduction instead. The initial state and subsequent growth of forced modes in the literature, .e.g. [4, 8, 16], are a direct result of the introduction technique that underestimates the initial amplitude. The resulting behavior defies what we would expect to see in nature.

Stability simulations are strongly affected by the assumptions made for mode introductions for both the primary mode and forced mode introductions. Nonlinear forcing is able to correct for the incorrectly estimated initial state of the introduced modes. This results in the strong transients when using a mode introduction technique that fails to accurately estimate a mode's state at that stage. However, the correcting ability of the nonlinear forcing depends completely on the accuracy of the rest of the modes present in the system. In addition, the magnitude of the error made during the introduction should be minimal as an introduction error can affect the other harmonics, reducing their ability to correct the introduced mode. An error is felt directly by the other modes through nonlinear forcing. It is therefore hypothesized that improving the introduction of the mean flow distortion should improve the results significantly. If forced modes are introduced with incorrect properties, the system is unable to converge to the same final state as for a correct introduction. Therefore, the final state is significantly affected.

A visual comparison between the results from Chang [8], our approximation of those results and two simulations where nonlinear nonparallel forced mode introduction is applied using ILPSE2 or ILPSE3, are presented in figure 6.11. Table 6.1 summarizes the forced mode introduction techniques used for the results. All primary modes were initialized identically, using ILST.

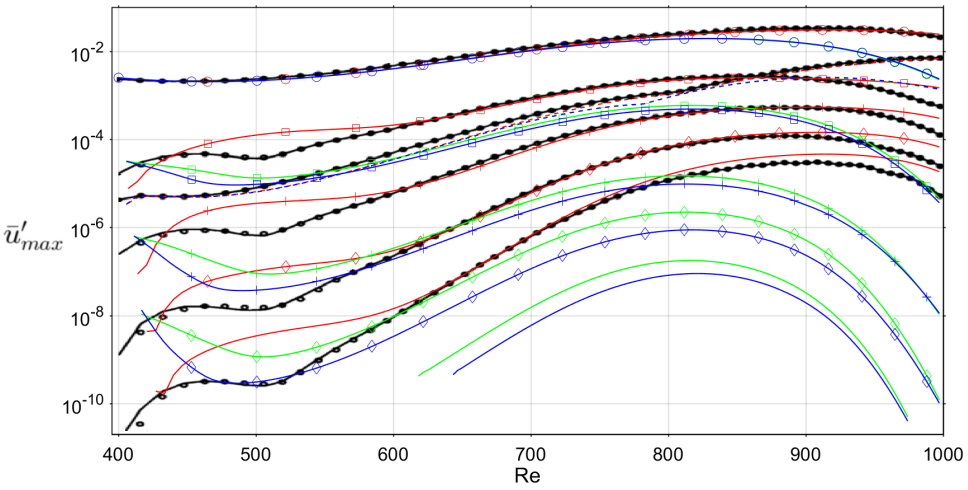

Figure 6.11: TS wave evolution of modes 1 (o), 2 (□), 3 (+), 4 (◇) and 5 (-) and the mean flow distortion (–) with forced modes introduced via ILPSE1 with a linearly determined wavenumber (red), ILPSE2 (green) or ILPSE3 (blue) over results from Chang et al.[8] (black).

Table 6.1: Forced mode introduction techniques in figure 6.11.

Result color	A_{i-1}	α	$\hat{q}$
Black	Unknown	Unknown	Unknown
Red	0	ILST	ILPSE1
Blue	A_i	Wavenumber averaging	ILPSE2
Green	$A_i e^{-\alpha_i \Delta x}$	Wavenumber averaging	ILPSE3

The resulting amplitudes of the harmonics are lower downstream of the introduction when the amplitude before the introduction stage is assumed non-zero following ILPSE2 or ILPSE3. The zero amplitude introduction results in a higher amplitude downstream of the introduction, increasing the strength of nonlinear interactions. As was touched upon previously in this section, that this is not what we would expect see in nature if no modes are forced suddenly via discrete roughness elements. Further research must be done to verify this, however. The result is strongly affected by the inflow condition and marching solution technique of the parabolic system. The ILPSE2 and ILPSE3 introduction techniques agree very closely on the introduction amplitude since the amplitude assumptions in these methods are comparable, although modes are more stable in the case of ILPSE3 since the amplitude prior to the introduction was assumed greater. As will be analyzed later in this section, ILPSE3 overestimates the stability of modes in this case as wavenumber approximations, following wavenumber averaging, lose accuracy when many modes are introduced simultaneously.

The accuracy of the initial growth rate in forced mode introductions is of great importance when a first-order approximation of the amplitude at the previous stage is performed. At $Re = 500$, the effect of the initial growth rate can be seen when comparing the green and blue results against the red results in figure 6.11 as all harmonics have shrunk to amplitudes lower than an otherwise identical simulation. The only difference with respect to the simulation that did not handle the amplitude at the stage preceding introduction, is that $\alpha_i < 0$ as a result of the introduction at a lower amplitude. Note that, for the red results, ILST was used to find the wavenumber of the harmonics and from the third harmonic up, they were all stable. Despite this initially stable wavenumber, the underestimation of their amplitude results in a rapid growth after one stage. The nonlinear effects on the primary mode as shown in figure 5.1, are no longer visible when the modes were introduced with the new ILPSE method. The stable introduction of higher harmonics means that the amplitude is significantly smaller after this introduction and the nonlinear effects on the primary mode are reduced.

The growth rates presented in figure 6.12(a-c) reflect what can be seen in the amplitude plots, although transients are not completely removed when using ILPSE2 or ILPSE3. The transients in figure 6.12(c) are a result of wavenumber averaging being too susceptible to the introduction as transients build up in the approximation of higher harmonics. The approximation deteriorates as growth rates are no longer a direct result of physi-

cal nonlinear forcing and instead originate from the incorrect introduction amplitude that is compensated through the growth rate. The result is that the first-order approximation of the amplitude at the stage before the introduction deteriorates and results in a subsequent miscalculation of the growth rate. In this case, when many harmonics are being introduced simultaneously at the inflow, an improvement can be made by ensuring that the introduction amplitude is independent of the estimated growth rate as shown in 6.12(b). The introduction of the fifth harmonic is accurate after a first-order approximation of the amplitude before the introduction stage as is seen in 6.12(c). In this case, the growth rates of other modes are not affected by the introduction amplitude and the first-order approximation closely models the amplitude before introduction.

Near the inflow, at $Re = 400$, in figure 6.12(b), the transients in the growth rates are severely reduced when the error build-up is prevented. The introduction of the fifth harmonic around $Re = 625$ is still gradual and is steady after only two spatial steps. The introduction amplitude, according to the correction in the step after introduction, was a slight overestimation and the solution of the second step is therefore accompanied by a slightly less unstable growth rate. This is expected as, in ILPSE2, the amplitude at the previous stage is estimated to be equal to the amplitude at the introduction stage. For a growing mode, this means A_{i-1} is overestimated, resulting in a overestimation of A_i. This reduced growth rate corrects the amplitude in that step. A similar, yet smaller error is made in the estimation of A_{i-1} with ILPSE3. The growth rate is changed in the subsequent step to correct the amplitude through nonlinear forcing. Afterward, the growth rate follows a smooth curve. This error is small in both cases, which allows the nonlinear forcing to correct it quickly. Its effect downstream of the introduction is hypothesized to be negligible as a result.

The results changed significantly when the ILPSE were used to introduce harmonics without assuming a zero amplitude. The results for this case with the introduction technique presented in this thesis are shown in figure 6.13 without the reference. The harmonics are now introduced using ILPSE2, i.e. at an equal amplitude for both stages, to reduce the error made by wavenumber averaging. An introduction error is present when using ILPSE3 in this case, as the threshold for introductions is 10^{-10}, causing most harmonics to be introduced at the inflow. The introduction amplitude is greater than harmonics introduced via ILPSE1, however, these modes are now stable at their introduction. The stable state of the modes results in a much smaller amplitude downstream of the introduction and presents a very different case for the evolution of all harmonics. Transients near the initial condition are no longer visible as the amplitude and growth are consistent.

In addition to the observation of mode introduction growth rates, the trend of growth rates of harmonics with respect to other modes in the system can be seen in figure 6.12(b) and (c). Despite the lasting effect of the introduction in 6.12(a), we see consistency in the growth rates downstream of the inflow. The trend, indicated by the arrows, shows that an unstable primary mode, results in even more unstable harmonics, a neutral primary mode results in all harmonics being neutral and a stable mode forces even more stable harmonics. In other words, the primary mode growth, through its forcing of the harmonics is the predominant factor in their evolution. Wavenumber averaging makes use of this for approximating the growth rate of a nonlinearly forced mode. This observation reinforces the idea of using wave number averaging for mode introductions and is the key to reducing the introduction transients.

6.1.3. Remarks

The evolution of the TS instability and its harmonics proved a valuable case for the investigation of mode introductions. From this case, we have seen the importance of the assumptions made in introduction schemes for results (far) downstream of the inflow. The user should be aware of the effects of mode introduction assumptions in the NPSE and use an appropriate technique for that specific case. This conclusion, in addition to the sensitivity to the grid as will be covered in section 6.4, makes the NPSE a more involved technique than to the OS or LPSE for transition prediction.

The NPSE are an initial value problem and every result presented in either the previous literature or this report, is a solution to a different problem. This makes it hard to compare the results, since they are all valid solutions. To create a more robust NPSE, however, the initial value should be correctly modelled. The NPSE are a powerful tool, although they are very dependent on the initial condition. This means introductions should be accurate in a physical sense, i.e. accounting for nonlinear forcing, nonparallel effects, growth rate and history of the mode.

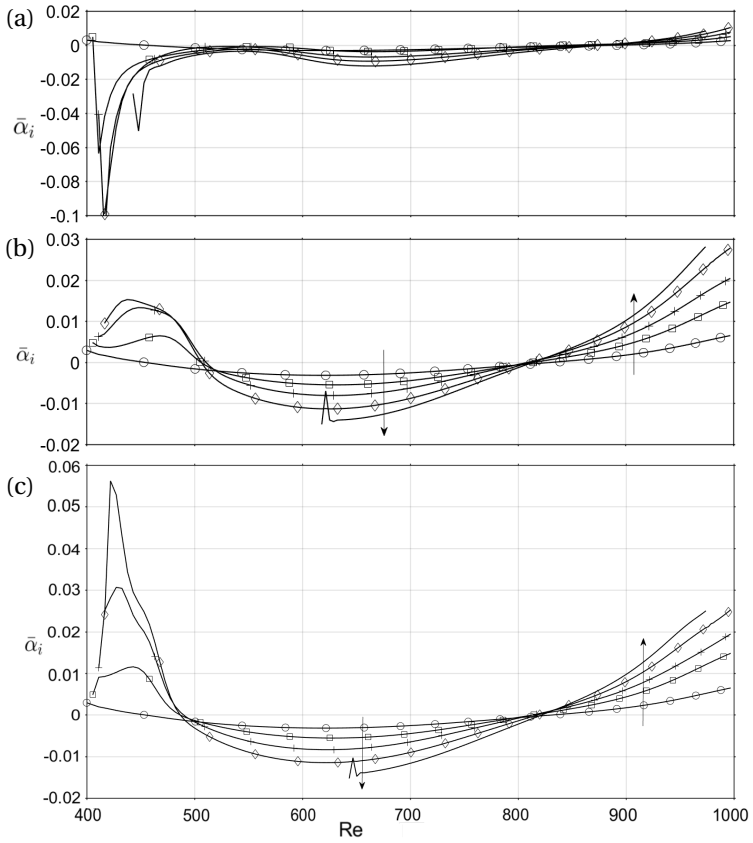

Figure 6.12: Growth rates of modes 1 (o), 2 (□), 3 (+), 4 (⋄) and 5 (-) using (a) ILSE1, (b) ILPSE2 or (c) ILPSE3 with arrows indicating the trend of growth rate for increasing β_r.

For primary mode introductions, the ILST provides excellent results. Following the primary mode introduction, harmonics can be introduced accurately via either ILPSE2 or ILPSE3 depending on the intensity of mode introductions in favor of ILPSE2 modes for high intensity given its reduced dependency on the results of wavenumber averaging.

Although the effects and importance of primary and forced mode introduction were investigated using only one case with a set nondimensional frequency F, global Reynolds number of $Re = 400$ and without a crossflow component, no assumptions were made that limit the conclusions to this case exclusively. The introduction of forced modes for different frequencies, Reynolds numbers or in a crossflow case, is governed by the same physics and equations. Consequently, the same conclusions hold for different Reynolds numbers, frequencies and spanwise invariant velocity profiles in general.

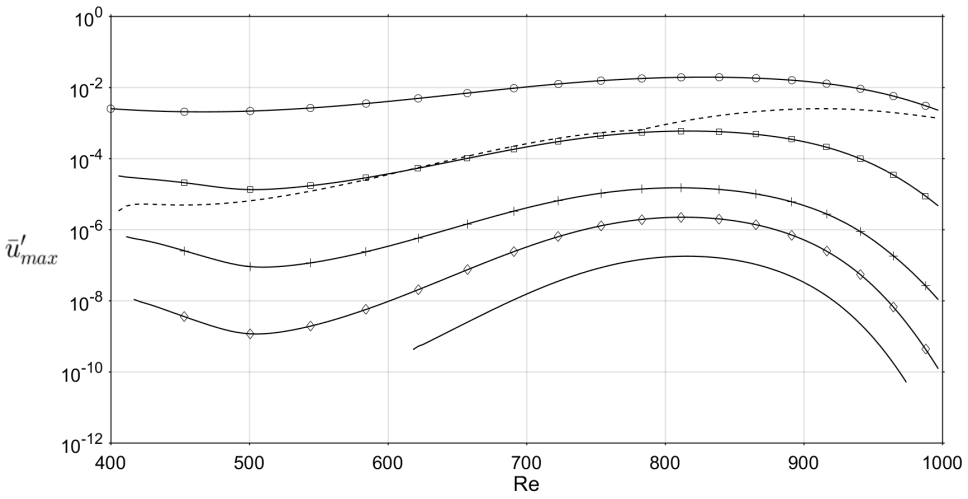

Figure 6.13: TS wave evolution of modes 1 (o), 2 (□), 3 (+), 4 (⋄) and 5 (-) and the mean flow distortion (–) accounting for nonlinear and nonparallel effects in forced mode introduction.

6.2. Crossflow instability case

The boundary layer that develops over the wing of an airliner is not a Blasius boundary layer and, instead, features a favorable pressure gradient and a crossflow component. In order for the NPSE to be of value to the industry, the application of the NPSE is to be validated for a crossflow boundary layer. Therefore, the NPSE were used to predict the nonlinear evolution of stationary CFI's in a crossflow boundary layer as presented in section 5.5.

The crossflow case was run using both the linear and nonlinear PSE codes. In the nonlinear code, the introduction of forced harmonics is performed using the first-order backward ILPSE introduction technique, i.e. ILPSE3. Results from the two codes should match perfectly initially if amplitudes are small. The LPSE thus serves as a reference for the linear growth of the primary mode. As the amplitude of the primary modes and that of the harmonics increases, the NPSE result should diverge from the linear result. The primary mode is initiated using ILST to provide a wavenumber and shape function. The comparison of linear and nonlinear primary mode evolution can be seen in figure 6.14.

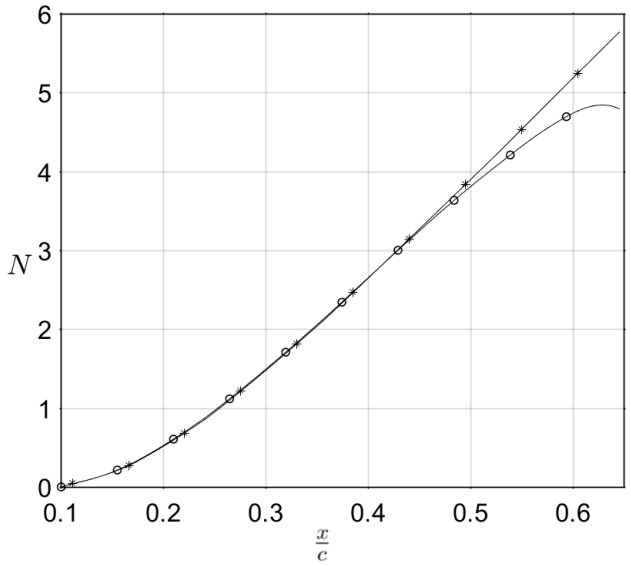

Figure 6.14: Crossflow instability primary mode N-factor growth from LPSE (*) and NPSE (O) with $\bar{A}_0 = 0.0035$.

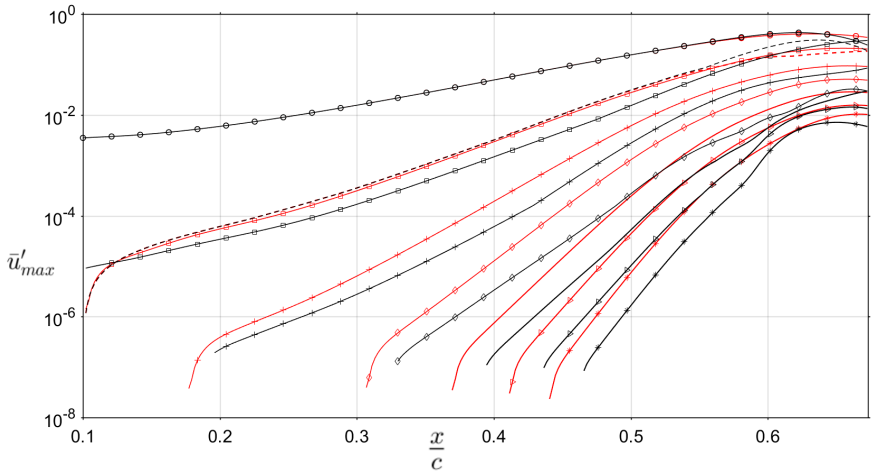

Figure 6.15: Perturbation growth of the primary mode with an initial amplitude $\bar{A}_0 = 0.0035$ (O), second harmonic (□), third harmonic (+), fourth harmonic (◇), fifth harmonic (-), sixth harmonic (<), seventh harmonic (>) and the mean flow distortion (–) using a zero amplitude (red) or fist-order backward approximation (black) introduction scheme for forced modes.

The primary mode grows linearly up to $\frac{x}{c} = 0.44$, after which the results deviate. At this point, the nonlinear interactions start to affect the primary mode's growth. The effect of the harmonics on the primary mode is a suppression of its growth compared to the linear case. The N-factor at this point is 3.1 which means that the mode has increased in amplitude just over 22 times to a peak nondimensional streamwise perturbation amplitude, $\bar{u}'_{max}$, of 0.0777. The nonlinear simulation was performed including seven harmonics and the mean flow distortion. Their growth compared to a simulation with the zero amplitude assumption, for forced mode introduction can be seen in figure 6.15.

The growth of higher harmonics follows the primary mode in both cases. The evolution of the primary mode is identical until the peak amplitude is reached. The amplitude of the harmonics is consistently lower in the case of forced mode introductions with ILPSE3 (black). The harmonics introduced by ILPSE3 are less unstable after their introduction due to a more physical approximation of their amplitude and do not experience the same overshoot of amplitude that the modes introduced from zero are subjected to. This prevents them from reaching the same amplitude that unstable modes forced from a lower amplitude would. Consequently, all higher harmonics are forced at a lower amplitude.

After $\frac{x}{c} = 0.6$ growth rates differ despite the consistency in N-factor growth rate prior to this point. The downstream effects of the forced mode introduction scheme become apparent afterward as the second mode appears more unstable and grows to overtake the primary mode. The reason for this is hypothesized to be the combined effect of the introduction scheme and the strength of the interactions as a function of amplitude. Introduction of harmonics with ILPSE3 results in a lower amplitude downstream that forces higher harmonics at lower amplitudes. Since the modes that force the second harmonic are growing with it, it does not have the ability to converge to the forced amplitude and remains too small. When the system saturates, the harmonic are allowed to converge or even overshoot via nonlinear interactions. As a result, it grows for longer than the primary mode and can even overtake it in amplitude. In other words, the ILPSE introduction accounting for the upstream history of the mode shows delayed transient effects of the harmonics. The growth of the third and fourth harmonic also show inconsistent behavior following the same hypothesis, albeit less strong than the secondary harmonic. A DNS comparison will have to be performed to validate the introduction schemes. This validation will be performed in section 6.3.

The introduction of higher harmonics shows a significant reduction in transient behaviour when consistency is maintained with the expected growth rate. The mean flow distortion, which could not benefit from the new introduction technique, still suffers from an error in the introduction. The numerical reason for this was explained in section 4.3.3. It is uncertain what its effect is in the ILPSE3 simulation since no tests could be performed with an improved mean flow distortion introduction. The growth of the mean flow distortion is initially identical for both simulations since its nonlinear forcing is dominated by the primary mode. The order of nonlinear interactions of higher harmonics with their complex conjugate are of a much lower order

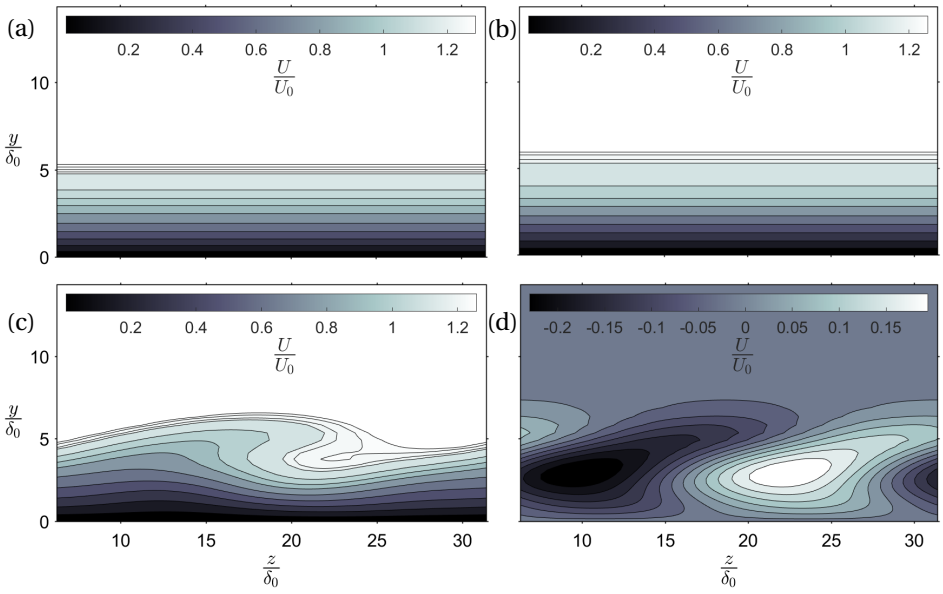

Figure 6.16: Streamwise velocity contours at $\frac{x}{c} = 0.5584$ of the (a) base flow, (b) mean flow, (c) mean flow and primary mode, (d) primary mode.

and consequently differences are minimal. This reinforces the hypothesis that the effect of introductions can show delayed effects as they become apparent far downstream of the introduction when amplitudes have increased. Primary mode growth is unaffected by the forced mode introduction scheme until $\frac{x}{c} = 0.6$. This indicates that strong nonlinear interactions only appear after this point. From this point onward, the growth of all harmonics start showing qualitative and quantitative differences.

Results after $\frac{x}{c} = 0.6$ follow the framework of the NPSE, although perturbation velocities approach the order of the base flow. This is no longer representative of physical behavior as the boundary layer is expected to have transitioned to a chaotic state by this point. Secondary instabilities were unable to enter this simulation and breakdown to turbulence could not occur. The simulation is confined to the limited spectral-domain as presented in table 5.2 for this case.

The contour plots depicted in figure 6.16 function as a qualitative check of the results. The simulation of crossflow instabilities was performed in a two-dimensional setting. A quasi three-dimensional flow field was recreated by evaluating the Fourier-ansatz at discrete spanwise locations that introduces a phase shift to the shape functions. This spanwise location is therefore arbitrary. The mean flow distortion is not oscillatory and thus does not show any periodicity in z. Note that the streamwise freestream value exceeds the normalization velocity as this case features an increasing streamwise velocity, see equation 5.2, and the contours are presented downstream of the inflow. At the streamwise location of $\frac{x}{c} = 0.5584$, nonlinear effects have started to be noticeable, as can be seen in figure 6.14. The effect of the perturbations on the instantaneous flow field is therefore strongly present. The mean flow distortion results in a growth of the boundary layer and the primary stationary crossflow mode induces a crescent in the flow that sweeps high-momentum flow downward and low-momentum flow upward. The isolated induced velocity from the primary mode is shown in figure 6.16(d).

The effect of other modes is present indirectly in the primary mode in terms of amplitude and shape. The primary mode was affected by their presence through wave-triad interactions. Direct effects on the flow, however, were not yet shown. Figures 6.17(a-h) show the isolated contours and the cumulative effect on the instantaneous flow field of the second up to the fifth harmonic. For higher harmonics, the amount of repetitions in spanwise direction increases as expected. The amplitudes of these harmonics appear too small to see any major differences in the contours. Their indirect effects are analyzed more closely in section 6.4, where the effect of the harmonics on the primary mode will be quantified through a convergence study.

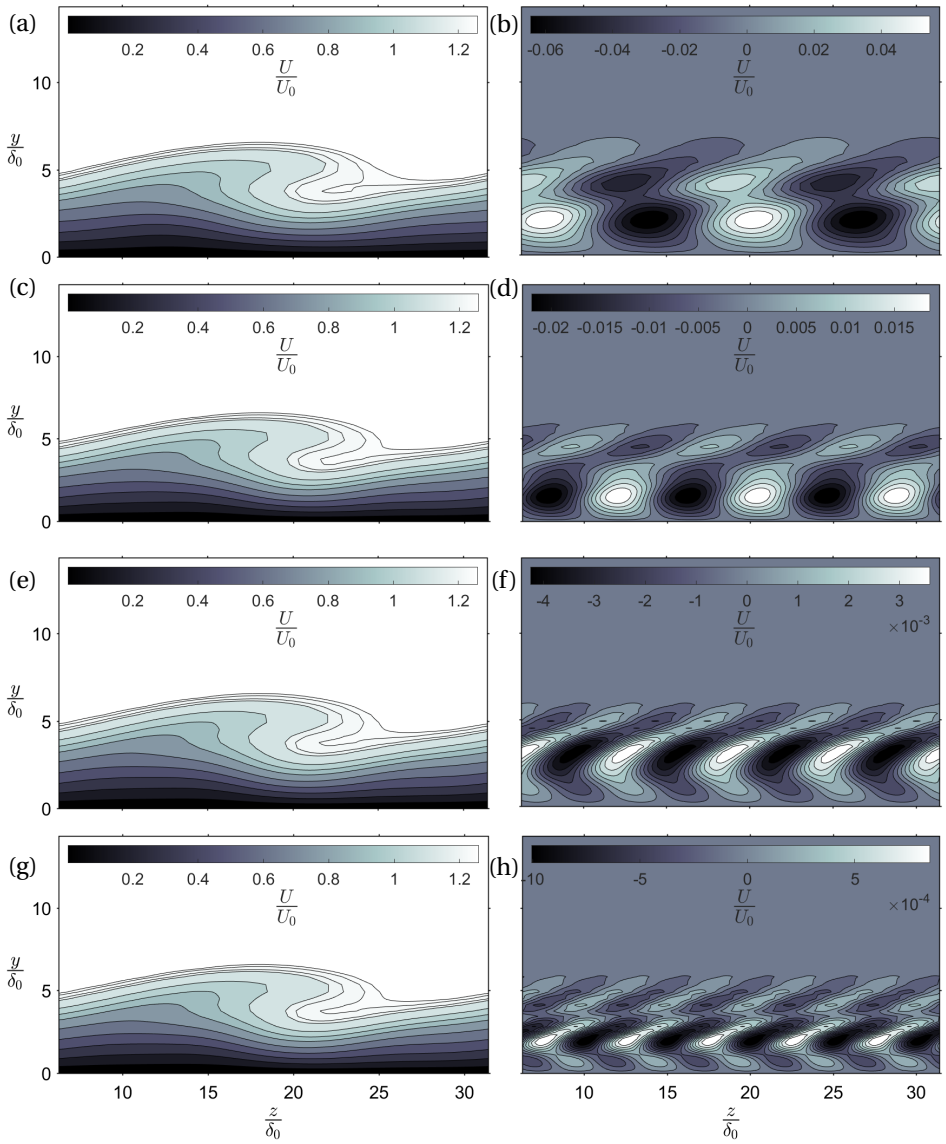

Figure 6.17: U-velocity contours looking downstream at $\frac{x}{c} = 0.5584$ of the mean flow and harmonics (a) 1-2 , (c) 1-3, (r) 1-4, (g) 1-5 and the isolated effect of modes (b) 2, (d) 3, (f) 4, (h) 5.

In appendix C, contours are shown at four discrete stations that show increasing deformation of the instantaneous flow field as the perturbations grow in amplitude. Initially, around $\frac{x}{c} = 0.4816$, the instantaneous flow field shows only minor wave-like motion. As we move downstream, a crescent is formed that shows the displacement of low-momentum flow upward and high-momentum flow downward. At the end of the computational domain, the crescent almost attaches to the boundary layer. This deformation is not expected in reality. It does, however, occur in our simulations as the NPSE framework limits the possibility of perturbations to the chosen spectral domain. The rise of secondary instabilities is therefore suppressed and the evolution of present harmonics can continue for longer.

The deformation of the instantaneous flow field as a function of the streamwise coordinate is presented in figure 6.18. Three views of the same isosurface in the instantaneous flow field can be seen that depict the surface characterized by the total streamwise velocity of $U = 0.99U_0$. The crescent is not visible until $\frac{x}{\delta_0} = 1600$, after which it rapidly develops. The formation of the crescent in the contour occurs in a short range of $\frac{x}{\delta_0} = [1400\ 1700]$ through the exponential growth of perturbations. The contour shows the increasing displacement of high-momentum and low-momentum flow in and out of the boundary layer respectively as was previously shown in figures 6.16 and 6.17.

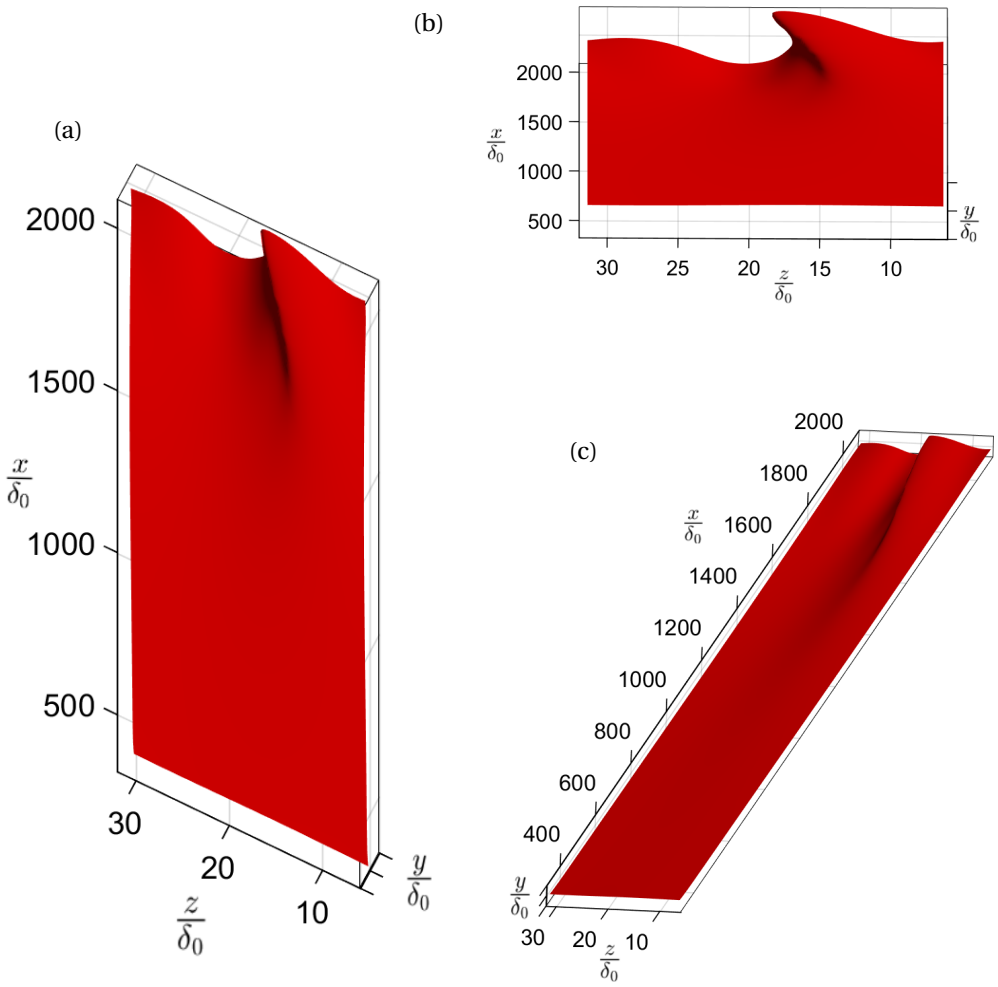

Figure 6.18: Streamwise velocity isosurface of $0.99U_0$ from (a) top view, (b) looking in streamwise direction and (c) elongated top view.

A nonlinear introduction technique was used for forced mode introductions that accounts for the preceding stage through the projected growth rate from wavenumber averaging. As mentioned before, the ILPSE mode introduction technique with a non-zero estimation for the previous stage cannot be used for the mean flow distortion. A noticeable initial growth can consequently be observed in this mode as its initial amplitude is underestimated. The oscillatory modes, that are accompanied by a wavenumber, can benefit from the backward-Euler approximation of growth and, consequently, their introduction follows a physical trend. The introduction of the harmonics follows a physical introduction as its amplitude and growth rate are consistent with each other and the growth of the primary mode.

The contour plots and isosurface show expected behavior and development of crossflow instabilities. The growing crescent shows the formation of a loosely disconnected high-velocity region that is the result of the superposition of different velocity fields, in the appendix figure C.8. Increasing the number of harmonics in the plot reduces this disconnect. The convergence studies in section 6.4 will show that results have converged sufficiently for stability analysis when five harmonics are accounted for in terms of amplitudes. The contours require more harmonics to attach the high-velocity region to the external flow. In reality, a disconnected high-velocity region could not occur as it could only have originated from the inward sweeping of high-momentum particles into the boundary layer. It is therefore expected that results in the later stages of the simulation should deviate from experiments or DNS.

6.3. DNS comparison

A DNS of the same flow was performed to provide a quantitative validation of the NPSE in a crossflow setting. In this comparison, the DNS base flow was used as a base flow for both the NPSE and DNS to rule out the effects of the boundary layer equation assumptions.

The total computational time for the NPSE was around 30 minutes on a personal laptop, whereas the NPSE required 4 days of computing time on a server. The NPSE is thus proven to be a viable tool for the prediction of nonlinear evolution of crossflow instabilities at a fraction of the time required to run a DNS.

Since the second harmonic and the mean flow distortion were not provided to the DNS at the inflow, they have to be forced from zero. This is equivalent to forced introduction using ILPSE1. A threshold of 10^{-7} was used in the NPSE to check the accuracy of higher harmonics introductions compared to a DNS that features a threshold of numerical accuracy. The comparison between DNS and NPSE results for the crossflow case can be seen in figure 6.19.

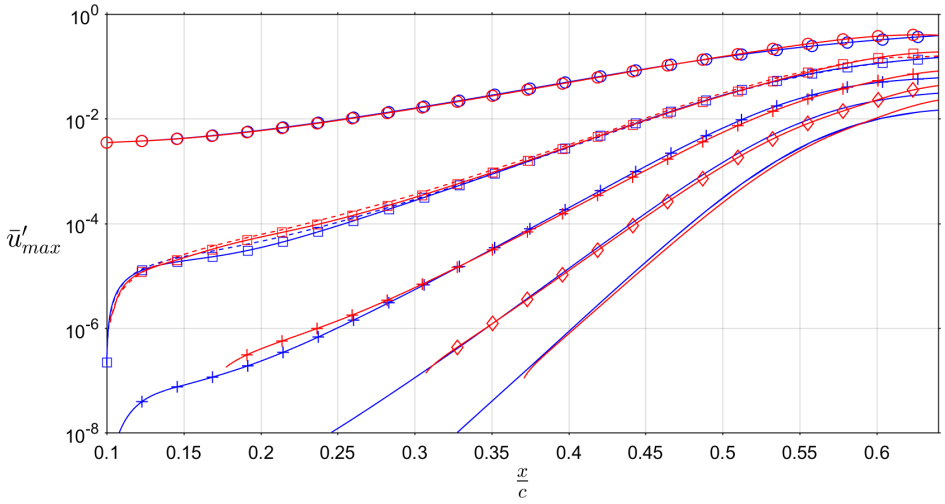

Figure 6.19: Nonlinear crossflow instability amplitude evolution comparison between DNS (blue) and NPSE (red) of the primary mode (O), second harmonic (□), third harmonic (+), fourth harmonic (⋄), fifth harmonic (-) and the mean flow distortion (–).

The evolution of all harmonics matches closely and the accuracy of the ILPSE3 introduction technique for forced modes can be seen in the higher harmonics. The initial condition of forced modes is accurately predicted for both the amplitude and growth. The estimation of growth of the second harmonic and mean flow distortion in the NPSE are slightly different from the DNS after the inflow. It is hypothesized that the mismatch here is the result of the parabolic nature of the NPSE that are solved via marching. The NPSE is more dependent on the initial condition as its errors can only be reduced via marching. This marching, however, is also the dimension in which the solution is found. The DNS is fully elliptic and features time marching schemes to reduce transients, allowing for upstream corrections of mode amplitudes. Consequently, the DNS is hypothesized to provide more accurate results and is less sensitive to the initial condition. The introduction of the third harmonic is affected slightly by this error in the second harmonic because its forcing is a direct result of interactions between the first and second harmonic. Further downstream, amplitudes match more closely and forced mode introduction provides accurate approximations of the introduction.

The DNS and NPSE show a difference in amplitudes sufficiently far away from the inflow. The NPSE predicts a consistently higher amplitude of all modes. The upstream correction of the mean flow distortion and second harmonic introduction found in the DNS is hypothesized to play a major role in differences far downstream. In addition, the strong nonlinear interactions between modes in the nonlinear regime, around $\frac{x}{c} = 0.6$, require a very fine discretization and enough harmonics in the system to be able to converge as will be shown in section 6.4. A lack of the aforementioned in the NPSE can also affect the results significantly.

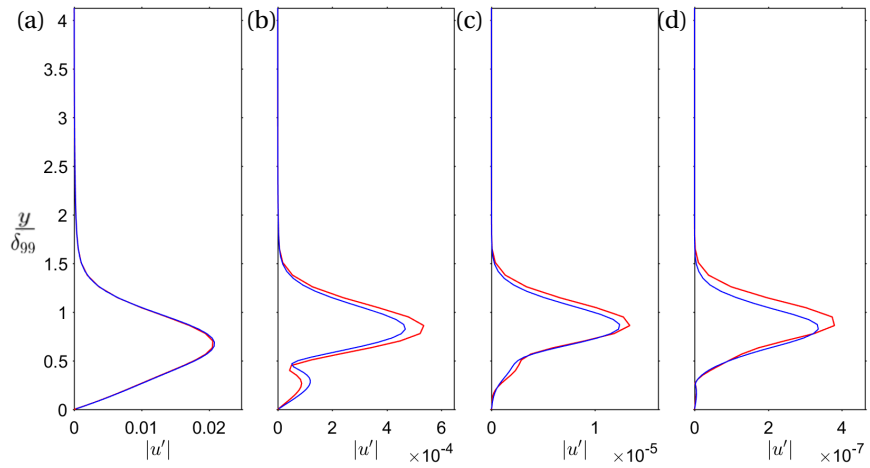

Figure 6.20: Absolute streamwise velocity perturbations from NPSE (red) and DNS (blue) for the (a) first, (b) second, (c) third and (d) fourth mode at $\frac{x}{c} = 0.3719$.

A comparison of the mode shapes from NPSE and DNS could provide valuable insight into the differences found in the amplitudes. The mode shapes, although not used directly for transition prediction, are an important wave property. The first four harmonics, aside from the mean flow distortion, are compared in figure 6.20 at a streamwise location of $\frac{x}{c} = 0.3719$. The wall-normal coordinate is nondimensionalized by $\delta_{99} = 12[mm]$, the boundary layer thickness at the DNS inflow for comparison with DNS.

Further downstream, the match deteriorates and the amplitude mismatch shows more clearly in the mode shapes that were not normalized for comparison purposes. Results near the end of the computational domain, where nonlinear interactions dominate the evolution of all modes, can be seen in figure 6.21. This comparison was performed at $\frac{x}{c} = 0.6122$, where the amplitudes of all modes, but even more so for higher harmonics, are estimated greater in the NPSE simulation. The primary mode, although similar in shape, shows a more defined deficit in the perturbation velocity around $\bar{y} = 1$ in the DNS. The NPSE estimates the peak value to be slightly greater and occur at greater $\bar{y}$ compared to the DNS. The convergence of higher harmonics is not guaranteed for the NPSE due to the information asymmetry for higher harmonics. Eight harmonics where used, while the DNS was able to capture up to thirteen reliably. In addition, the convergence of all modes deteriorates rapidly in the nonlinear regime as will be shown in section 6.4. It becomes increasingly difficult to numerically and physically converge the NPSE in the nonlinear regime. The DNS are therefore trusted over the NPSE results in this region.

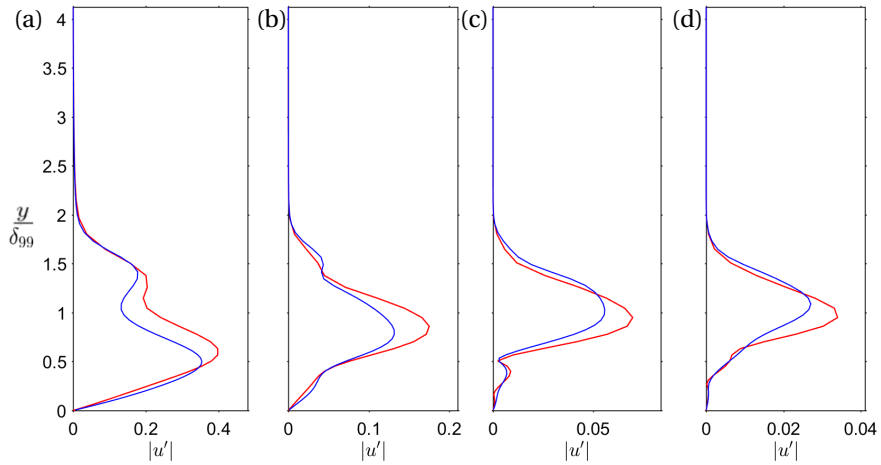

Figure 6.21: Absolute streamwise velocity perturbations from NPSE (red) and DNS (blue) for the (a) first, (b) second, (c) third and (d) fourth mode at $\frac{x}{c} = 0.6122$.

The sensitivity of stability analyses to the initial condition requires special care to match the inflow and boundary conditions. Since only the primary mode was presented to the DNS, the second harmonic and mean flow distortion have to come up from zero directly following the inflow plane. This can be approximated by forcing the second harmonic with a zero amplitude initially in the ILPSE to match the physics around the inflow of the DNS.

The instantaneous DNS flow field can be compared to the Fourier reconstruction of the NPSE simulation. Isolating one spanwise wavelength at streamwise locations of $\frac{x}{c} = 0.56$ and $\frac{x}{c} = 0.6122$ in figures 6.22 and 6.23 respectively. A structural difference is present in the lower branch of the crescent where high-momentum flow is swept into the boundary layer. The current NPSE code underpredicts this sweeping with respect to the DNS. This difference is increased in later stages and can be seen in the shape function comparison presented in figure 6.21 as well. The shape functions from the DNS provide a stronger second peak value around $\frac{y}{\delta_{99}} = 1.5$ in the absolute velocity perturbation profile.

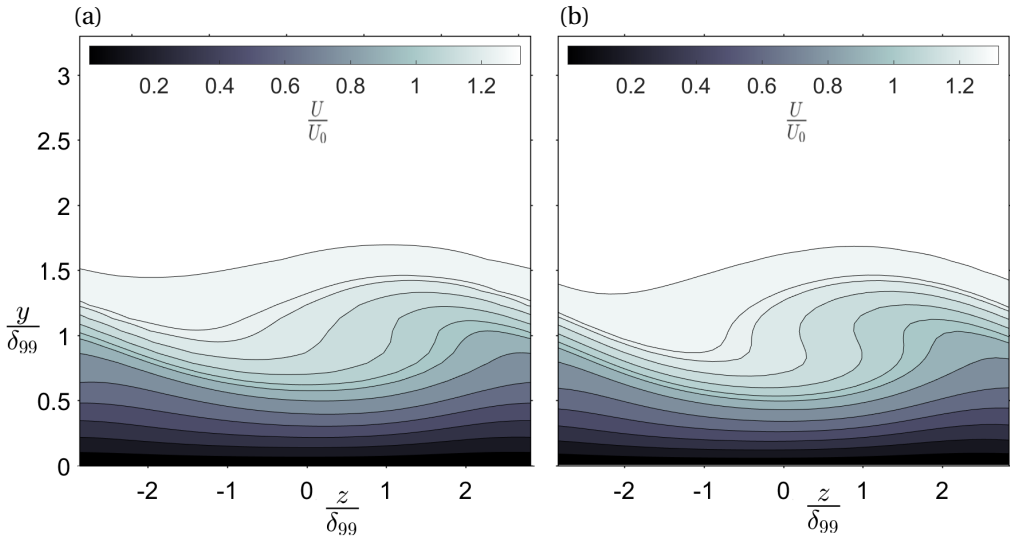

Figure 6.22: Streamwise total velocity contours at $\frac{x}{c} = 0.56$ from the (a) NPSE and (b) DNS.

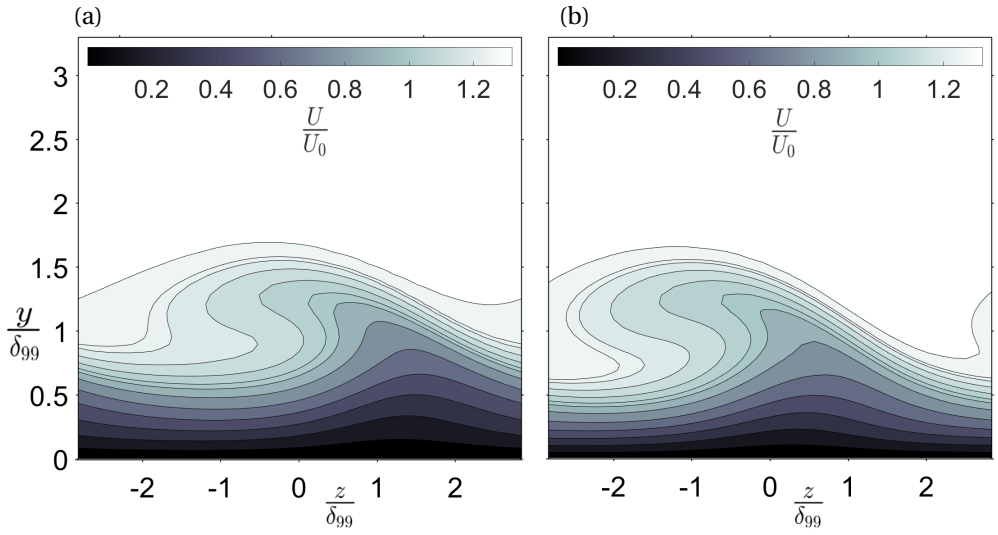

Figure 6.23: Streamwise total velocity contours at $\frac{x}{c} = 0.6122$ from the (a) NPSE and (b) DNS.

6.3.1. DNS inflow boundary condition

The initial condition in the NPSE following ILPSE3 is validated via a second DNS. In this DNS, the second harmonic is imposed on the inflow boundary following NPSE calculations as explained in section 5.2.1. The results for this new DNS and comparable NPSE simulation where all modes were introduced via ILPSE3 can be seen in figure 6.24.

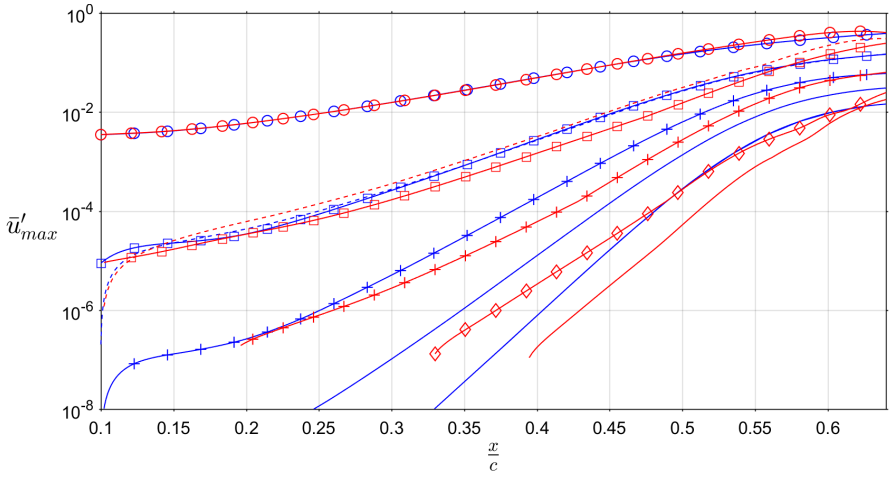

Figure 6.24: Nonlinear crossflow instability amplitude evolution comparison between DNS (blue) and NPSE (red) of the primary mode (O), second harmonic (□), third harmonic (+), fourth harmonic (◇), fifth harmonic (-) and the mean flow distortion (–) with the second harmonic imposed on the inflow in the DNS.

The initial transient found in the second and third harmonic, as well as the mean flow distortion, near the inflow in figure 6.19 are a result of the inflow plane suppressing them. The ILPSE3 has been proven multiple times to prevent initial transients in NPSE simulations. In the DNS, however, this appears less effective in doing so. The initial transient after the inflow in the DNS is hypothesized to be the effect of the mean flow distortion and higher harmonics. The mean flow distortion grows similarly in both cases following an initial transient that can be found in both cases. The third harmonic is present near the inflow in the DNS and was suppressed initially. The threshold of the NPSE suppresses this mode for longer, preventing its effect on the second harmonic. In the DNS, the effects of this introduction and the mean flow distortion are hypothesized to affect the second harmonic significantly, resulting in the transient near the inflow. Sufficiently far from the inflow boundary, results from this DNS compare up to the third decimal number in amplitude with the previous DNS results presented in figure 6.19. The NPSE results, however, differ greatly and present, again, the delayed transient behaviour in the strong nonlinear regime as was found in figure 6.15.

Despite offering a more physical prediction of second harmonic amplitude at the inflow, the ILPSE3 method results in smaller amplitudes for this mode and every mode forced thereafter downstream of the introduction. The forcing of the primary mode on the secondary mode is unable to force it enough to converge to the DNS amplitude. When introduced from zero, it overshoots initially and this allows it to converge to the same evolution as the DNS from this greater amplitude. It is hypothesized that this process, after overshooting, allows for a mode to converge to the correct relative amplitude in the NPSE and results in a close match downstream despite initial errors. In addition, the higher harmonics, whose forcing might be significant on the second harmonic, are not present and could be a factor in the second harmonic's inability to achieve the correct amplitude in the NPSE. Downstream of the inflow, the primary mode, and thus its forcing also grows in the marching direction, preventing the second mode from achieving the amplitude it might have converged to in an elliptic framework from a lower amplitude. This is in line with the conclusions from the TS case in section 6.1.2. This problem does not exist for higher modes as the first few modes are most important for this forcing, meaning that ILPSE3 can be used to force higher harmonics correctly.

The DNS is a boundary value problem that converges in time. It is therefore less dependent on the inflow boundary. Given that the DNS was able to converge to the same results downstream of the direct influence of the inflow, it is considered to be correct aside from possible outflow affects that were reduced via a buffer zone. Introducing the second harmonic from zero, while introducing the higher harmonics with ILPSE3,

leads to results that closely match the DNS results and are currently assumed correct. Further numerical and experimental research into the growth and presence of harmonics upstream of the inflow region is necessary to improve its physical representation.

6.4. Convergence

This section aims to verify the current solver through three separate convergence tests. For the NPSE convergence entails that a more refined discretization in x-direction or y-direction does not alter the resulting mode amplitudes. The number of harmonics simulated in the system is also hypothesized to affect the convergence. The harmonic convergence of the NPSE is therefore also studied. The base flow converges much faster than the stability calculations on that base flow. All simulations are therefore performed on the same grid for both the base flow and stability simulations.

6.4.1. Harmonic convergence

The number of harmonics captured in the system is hypothesized to affect the physical and possibly numerical convergence of the system. The numerical convergence refers to the ability of the solver to converge to any result for a discrete stage. And the physical convergence is the convergence towards the physical result as would be seen in reality.

There is per definition an imbalance at the highest harmonic in the system which is only nonlinearly forced by the interaction of lower harmonic modes. The interactions that play a role in these higher harmonics are of the same order as the interactions of even higher harmonics with complex conjugates. This mode will thus never be converged given that the neglected physics is still significant for that mode. Achieving converge thus means making sure the highest harmonic is of negligible amplitude to the primary mode.

The primary harmonic's amplitude evolution is most important for transition or stability analysis. Resulting from the asymmetry in the system that increasingly affects higher harmonics, the highest harmonic will never be converged. The goal is, therefore, to ensure that the highest harmonic is sufficiently small such that the primary mode is not significantly affected by it or its absence.

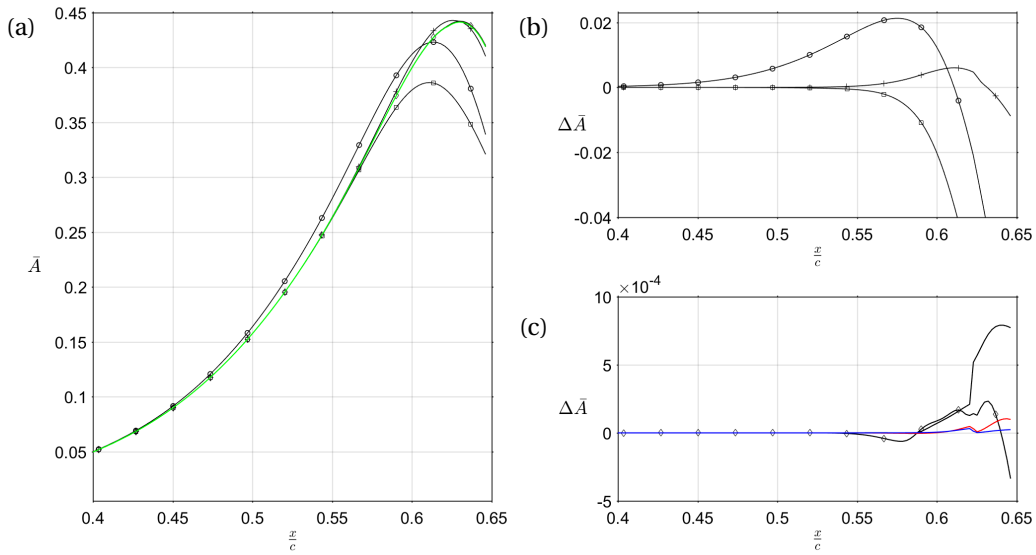

Figure 6.25: (a) Primary mode evolution for Ω = 1 (□), 2 (O), 3 (+), 8 green line. (b) Local amplitude difference w.r.t. Ω = 8 for Ω = 1 (□), 2 (O), 3 (+), (c) Local amplitude difference w.r.t. Ω = 8 for Ω = 4 (◇), 5 (black), 6 (red), 7 (blue).

To study the effect of the spectral domain, several simulations were run that incorporated up to eight harmonics. Every simulation reached a solution, although the results were significantly different. In figure 6.25, three graphs are presented that show the amplitude of the primary mode and the difference to the primary mode of the simulation with 8 harmonics. In figure 6.25(a), the results of simulations with over five harmonics can

no longer be differentiated between in the amplitude plot. The local difference with respect to the simulation that incorporated eight harmonics is shown in figures 6.25(b) and (c) and this clearly shows the difference becomes negligible for simulations with more than four harmonics. The most significant differences can be seen in the nonlinear regime where the importance of even the highest harmonics becomes clear. In this part of the simulation all modes have grown to considerable amplitudes and the effect of neglecting them becomes more apparent.

The amplitudes in figure 6.25 can be used to calculate an average absolute difference when a harmonic is added to explore the harmonic convergence rate. Introducing Δ, the average absolute difference between the amplitudes of the primary mode of two subsequent simulations. Convergence results are presented in figure 6.26.

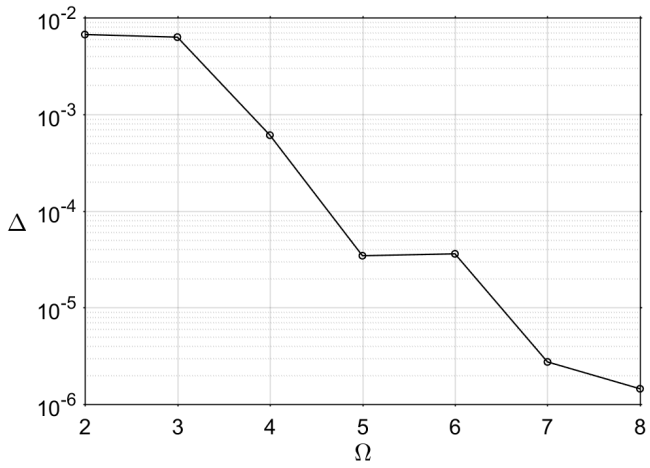

Figure 6.26: Average difference in primary mode amplitude for increasing spectral domains Ω.

The non-monotonic behavior of this convergence plot is hypothesized to be caused by the discrete nature of the evaluated quantity. Adding a harmonic is a discrete change in the system that can have a significant effect due to the interactions with all other modes in the system, including the primary mode. The general trend is therefore considered most important.

Figure 6.26 indicates a clear convergence trend and proves the need for enough harmonics in the system to be able to converge the results. The difference Δ decreases to the order of 10^{-6} for adding more harmonics after the seventh, which is a sufficiently low amplitude difference to be able to conclude the results have converged for stability analysis purposes. Although the NPSE is an extremely efficient way to predict the nonlinear stability of this base flow, incorporating more harmonics increases the computing time and memory needed to run a simulation. It is therefore advisable to run the first few simulations with fewer harmonics to test whether results converge numerically.

6.4.2. Grid convergence

The grid convergence is multifaceted as there are several numerical dependencies on the grid. The physical phenomena that are being modeled, e.g. the base flow and all harmonics, are of varying orders of magnitude and reside in different length scales. The code was built such that the base flow and stability analysis are generated using the same numerical grid. This does not affect the convergence since the base flow converges faster than the shape functions of the eigenmodes. The stability simulations are independently affected by y and x-discretization. Therefore, the convergence in respectively wall-normal and streamwise direction is examined separately.

Streamwise discretization

Research on the numerical instability resulting from residual ellipticity in the PSE framework was performed by Li and Malik [23]. This work showed that the stability problem is not well-posed due to the $\frac{\partial p}{\partial x}$ term for the mean flow distortion which causes the marching scheme to blow up for small step sizes. They offer

two solutions for the problem: dropping the $\frac{\partial p}{\partial x}$ term from the equations or enforcing a minimum step size $\Delta x_{\min} > |\alpha_r|^{-1}$.

It is noted by Li and Malik [23] that dropping the pressure term relaxes this condition by an order of magnitude and this can, therefore, be done if higher spatial accuracy is desired. They note that dropping this term should not significantly affect the results given that most of the physical pressure gradient is represented in the $i\alpha p$ term.

It was found for the current NPSE tool, that setting the $\frac{\partial p}{\partial x}$ directly to zero resulted in an ill-posed system of equations. It was, therefore, instead suppressed by a factor. For this study this factor was 500 in all cases. This suppression is a constant withina simulation, although the $\frac{\partial p}{\partial x}$ term is dependent on the spatial step size and the amplitude of the mean flow distortion. It was found that the numerical stability of the solver could, in some cases, depend on this factor and must be increased to be able to converge later stages. Further research must be done to determine the effect of this factor on the stability and possibly the results of the NPSE formulation. The most accurate streamwise discretization is thus given for $\Delta x_{\min} > |\alpha_r|^{-1}$.

For a too large spatial step size Δx the NPSE solver fails to converge numerically in the nonlinear regime. How far it would be able to reach into the nonlinear part of the simulation depends on the step size and is favorable for smaller step sizes. This region of stability analyses demands a high spatial resolution due to the increased strength of interactions that results in stronger gradients. An insufficiently small streamwise step size Δx results in extrapolation errors that affect both the accuracy and the numerical convergence of the solver.

As a result, convergence could not be shown for every possible step size. Any step size that would fail to converge over the entire domain is not incorporated in this study and the greatest nondimensional stepsize $\Delta\bar{X}$ given is the first step size for which the entire domain could be converged. Figure 6.27 shows the amplitude evolution for different streamwise spatial discretizations as well as the difference between the simulations and $nx = 275$ cases.

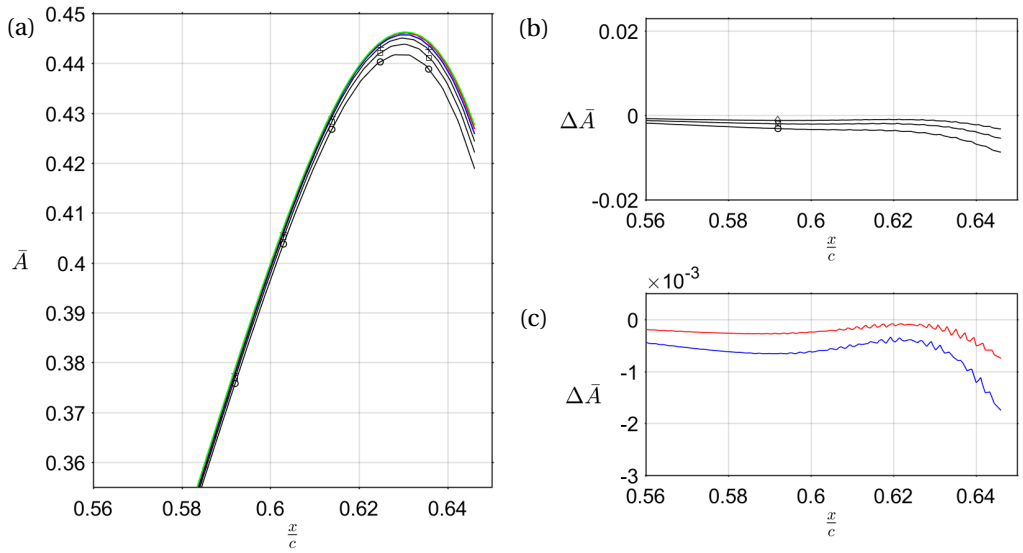

Figure 6.27: (a) Primary mode evolution, (b) Local amplitude difference w.r.t. nx = 275 and (c) Local amplitude difference w.r.t. nx = 275 for nx = 150 (□), 175 (O), 200 (+), 225 (blue), 250 (red), 275 (green).

The results are less sensitive to changes in streamwise discretization than the previously examined harmonic influence. Besides, for this case, the streamwise location of $\bar{A}_{max}$ is independent of this discretization. Differences are small and, although it should be a goal to minimize any influence of discretization technique, it is just as important that the results can converge numerically. These results show that streamwise accuracy can be sacrificed if it aids in converging the results. The results in the nonlinear regime should then be analyzed

with care, however. The differences between the $nx = 250$ and $nx = 275$ cases are at most of the order 10^{-3} which is within the required accuracy of transition prediction. The deviation from the most precise case increases with the streamwise location due to amplitude growth. This results in stronger nonlinear interactions and transients. Converging this rapidly changing region requires small spatial steps and an increased value of Δ can, therefore, be seen in this region.

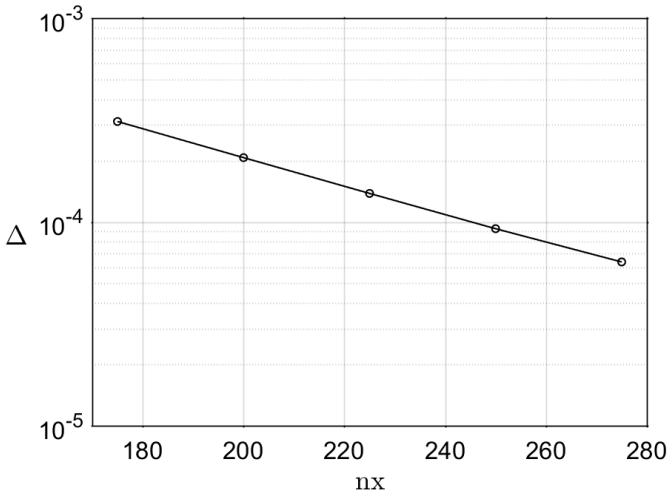

Figure 6.28: Average absolute difference in primary mode amplitude compared to having five fewer streamwise stations.

The difference Δ as a function of the streamwise discretization was plotted in figure 6.28 and shows a clear exponential numerical convergence. The domain of possible values for the streamwise discretization is very limited. A large number of streamwise stages is desired to be able to accurately describe the nonlinear regime and assure convergence. The spatial step size Δx is limited on the other end by the effect of residual ellipticity in the system. This results in a limited bandwidth of available x-discretizations. The differences in amplitudes between different discretizations are minimal, however, and an nx of 200 would already be accurate enough for transition prediction and DNS or experimental comparison.

Wall-normal discretization

The discretization in wall-normal direction is very critical as many different length scales are represented on this grid. Every higher harmonic resides in even smaller length scales, demanding a higher precision close to the wall. A spectral method using Chebyshev polynomials is exploited for the calculation of derivatives to increase accuracy.

Forced modes in this simulation are introduced using wavenumber averaging and ILPSE marching. This makes the use of ILST introduction techniques redundant, which are much more sensitive to wall-normal discretization due to the need to filter numerical noise in the resulting set of eigenfunctions from direct solutions. The current introduction technique significantly reduces the required y-discretization by generating the shape function from the nonlinear interaction of other represented modes. The nonlinear harmonics do not reside in smaller wall-normal length scales, in contrast to their linearly determined counterpart, see figures 6.20 and 6.21.

For all cases, the total domain height H was $0.02[m]$ and the Chebyshev midpoint was located at $y = 0.002[m]$, i.e. at 1% of the domain height. This domain height allowed all modes to decay to a very small number in the far freestream. To ensure that the convergence results were consistent, these values were not changed. This did, however, severely restrict the domain of possible ny values as the differentiation matrices appear unable to provide accurate results if nodes are too close to each other, resulting in the inability to converge the simulation. This should be kept in mind when analyzing the convergence plot and the limited domain for which convergence could be analyzed.

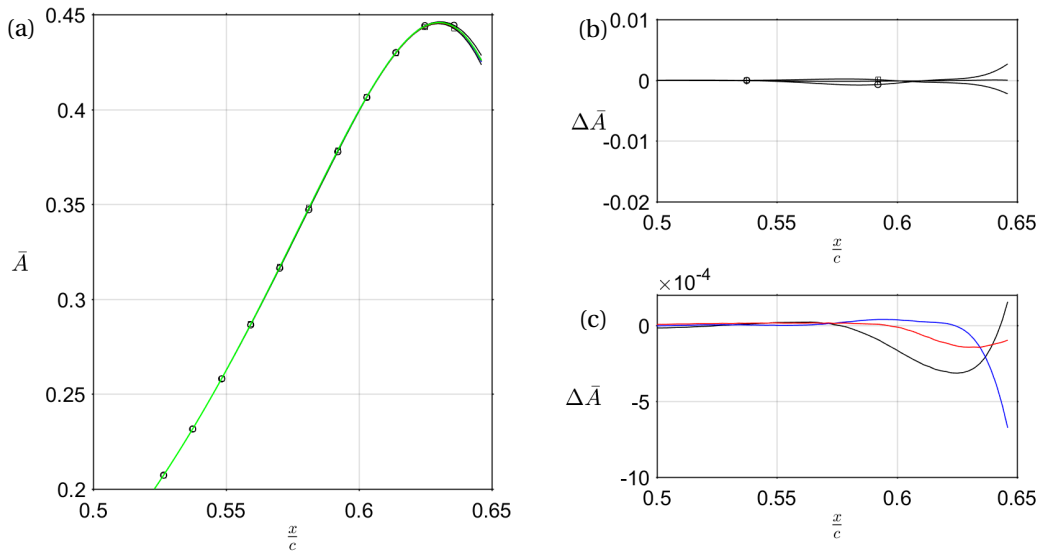

Figure 6.29: (a) Primary mode evolution, (b) Local amplitude difference w.r.t. ny = 70 and (c) Local amplitude difference w.r.t. results of ny = 70 for ny = 40 (□), 45 (O), 50 (+), 55 (blue), 60 (blue), 65 (red) and 70 (green).

The results of all simulations are comparable. The amplitude evolution is not very dependent on the discretization in y. The primary mode amplitude evolution is already accurate with only 40 collocation points. However, the shape of the mode requires a finer discretization for an accurate representation near the wall as will be shown in section 6.5.3 when considering the accuracy of the shape function representation. In fact, none of the simulations contained a smooth representation the shape functions using only the collocation points. A spline interpolation of the points, however, shows a perfect match of the shapes as will be shown in 6.5.3. This proves that, for the system, the shape functions are described accurately due to the use of spectral differentiation in wall-normal direction.

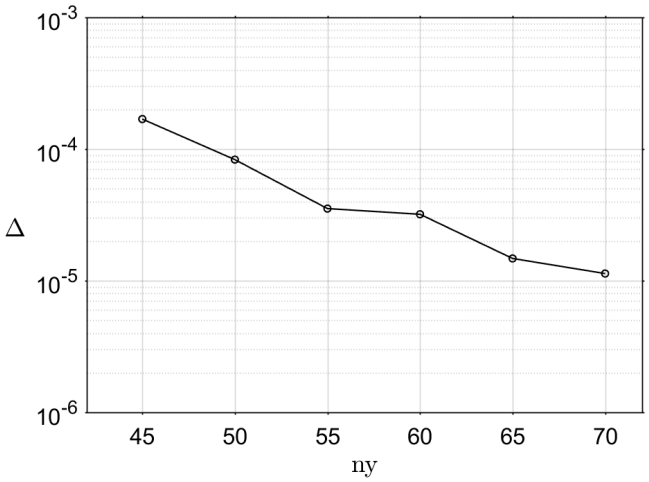

Figure 6.30: Average absolute difference in primary mode amplitude compared to having five fewer wall-normal nodes.

6.5. Numerical developments

This section comprises of updates and adjustments made to the current literature available on NPSE solvers that can affect its computational efficiency, numerical stability and accuracy.

6.5.1. Phase of harmonics

The perturbation shape functions, aside from the mean flow distortion, are complex and thus contain a phase. This phase is a function of the wall-normal direction y. Since the NPSE allows for interactions of these modes the relative phase of harmonics matters. As a consequence, attention must be paid to the introduction of the modes, especially if linear methods are used. Solving the eigenproblem in linear methods generally provides an arbitrary phase relative phase given that the other modes are not an input to the problem. The strength of the interaction between harmonics depends crucially on the phase relation to the other modes [30]. Ideally, the phase distribution would thus be determined by the nonlinear forcing directly at the introduction.

The exploitation of the ILPSE introduction technique enforces the correct relative phase of introduced modes through nonlinear forcing. The predominant factor for both the shape function of a mode and its growth is the nonlinear term. If it were neglected during the introduction, it would have to be manipulated to maximize the strength of the wave-triad interactions on this mode. This is a hard task given that the phase is a function of the wall-normal direction, which leaves many options. In the ILPSE introduction, no further adjustments thus need to be performed to the phase as nonlinear effects are not ignored.

To prove the importance and accuracy of the phase in nonlinear introductions for the NPSE, a test was performed. The introduction of the second harmonic in a crossflow simulation was artificially manipulated after finding the solution. A constant phase shift in wall-normal direction is applied to the mode, leading to

$$\bar{q}_{new} = \bar{q}e^{i\theta}, \tag{6.1}$$

where $\bar{q}_{new}$ is the phase-shifted shape function and θ is the phase. The phase shift was kept constant in the wall-normal direction as to not adjust the shape of the mode, only the phase. This was done for $\theta = [0\,\frac{1}{4}\,\frac{1}{2}\,\frac{3}{4}\,1]\pi$. It was not compared to ILST shape functions, since the nonlinear forcing is so strong for higher harmonics, that neither the shape nor the phase distribution showed any resemblance. The results for all of the simulations can be found in figure 6.31. Although the simulations were performed with 8 harmonics, the effects become clear from just the second harmonic and thus higher harmonics were not plotted. Applying the phase shift to every mode could result in a failure to converge after this introduction.

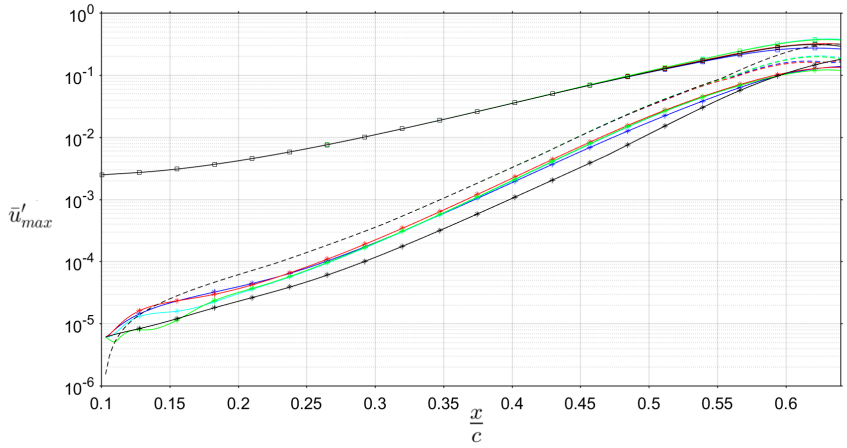

Figure 6.31: Effect of introduction phase for $\theta = 0\pi$ (black), $\frac{1}{4}\pi$ (blue), $\frac{1}{2}\pi$ (red), $\frac{3}{4}\pi$ (cyan), 1π (green) for the primary mode (□), mean flow distortion (–) and second harmonic (*).

Shortly after introduction with an arbitrary phase, strong transients can be seen. Peak amplitudes are plotted here, which are changing due to the shape manipulation. The error is corrected through nonlinear forcing of the unaffected primary mode in a few steps. The phase error might be present in NPSE simulations in the literature as well, e.g. [4, 8], given their use of linear techniques for forced mode introduction, however, it is probably hidden by the rapid growth caused by the zero amplitude assumption that causes much stronger transients. The mean flow distortion does not appear to be affected by the phase shift of the second harmonic as its forcing is of a significantly smaller order of magnitude. The mean flow distortion is still primarily affected by the primary mode. A delayed effect can be seen in the nonlinear regime where all results differ

greatly because of the phase shift, proving the importance of a nonlinearly determined phase distribution as performed in the ILPSE.

6.5.2. Crossflow forced mode introduction

The introduction of modes is a complex problem that has lead to many approximate solutions using a combination of linear, nonlinear, parallel and nonparallel techniques as can be seen in [4, 8, 14, 16]. In this thesis, we brought forward a novel nonlinear nonparallel method for mode introductions. Three different assumptions for mode introduction techniques are tested to evaluate the behavior and sensitivity of the NPSE to possible initial conditions within the ILPSE framework and find the effects further downstream of the introduction stage. All methods benefited from the addition of the mean flow distortion to the base flow to account for its effect on the introduction of nonlinearly generated harmonics.

Nonlinear introductions were generated via

1. ILPSE1, i.e. assuming $\bar{A}_{i-1} = 0$,

2. ILPSE2, i.e. assuming $\bar{A}_{i-1} = \bar{A}_i$,

3. ILPSE3, i.e. assuming $\bar{A}_{i-1} = \bar{A}_i e^{\bar{\alpha}_i \Delta\bar{x}}$.

An attempt was made to compare the results with a combination of ILST for $\bar{\alpha}$ and the ILPSE solver for $\hat{q}$ and the amplitude as well. However, the linear wavenumber estimate proved to be insufficient for ILPSE3 and resulted in convergence issues as all higher harmonics were linearly stable. The ILPSE introduction technique thus relies on an accurate estimate of the wavenumber to provide physical results. The introduction of

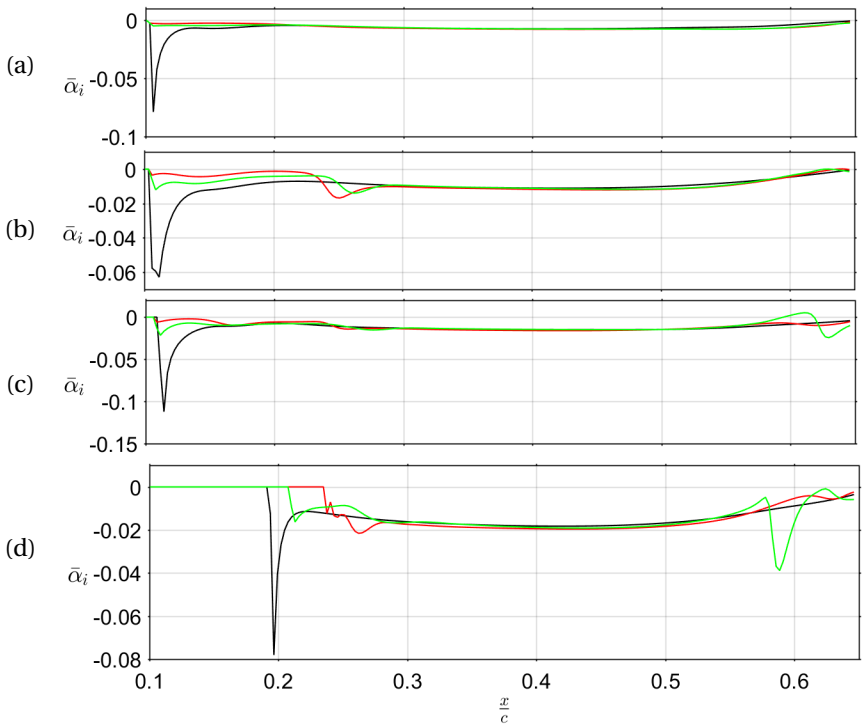

Figure 6.32: Growth rates for the (a) second harmonic, (b) third harmonic, (c) fourth harmonic and (d) fifth harmonic using methods 1 (black), 2 (green) or 3 (red).

modes requires a prediction of amplitude, shape function and complex wavenumber. Those specifications are dependent on each other through the effect of nonlinear forcing. This means that the miscalculation of any of the specifications will result in transient behavior as nonlinear forcing pushes the perturbation into a different state. Eventually, a perturbation will, therefore, approach an equilibrium, although this equilibrium

depends on the other modes in the system as well. If many modes are being introduced in close proximity, the equilibrium state is affected by the introductions and thus alters the final amplitude. This section aims to quantify this effect through the crossflow case. Wavenumber averaging gives the most accurate prediction of the nonlinear wavenumber of a forced mode and will be used in all cases for the introductions. The dependency of the method on this wavenumber is most pronounced in ILPSE3 as it is enforced via a first-order backward approximation of the amplitude prior to the introduction. The wavenumber α, however, is still present on the left-hand side of ILPSE1 and ILPSE2.

Using the ILPSE for mode introductions requires a wavenumber and an estimate of that mode's shape and amplitude at the previous stage. Previously that mode was neglected as it was below the threshold. The accuracy of the introduction can be directly read from the transients in this mode after the introduction. Any transient in an otherwise smooth simulation, especially in the linear regime, points to improper introduction. Therefore we will show the evolution of the amplitude and growth rate depending on the introduction.

The methods 1, 2 and 3 referred to in this section were introduced in section 4.3.2. The effects of the different mode introduction assumptions are visible in the growth rates shown in figure 6.32.

A strong transient can be found after the introduction when a zero amplitude is assumed initially. When the mode grows rapidly, as can also be seen in figure 6.33, the effective forcing term decreases and the growth rate stabilizes. A better assumption of the state according to the transient behavior of the mode before the introduction is given using methods 2 and 3. Both methods provide accurate mode introductions. The transient behavior of method 3 is less severe which is expected given the increased physical modeling. Further downstream, however, the behavior is more volatile and higher harmonics experience delayed transients. This is most likely caused by the amplitudes being smaller than what their forcing would indicate. However, since the marching direction is the only direction in which transients can be washed out, a mode cannot converge to the forced amplitude as this amplitude is growing as well. When the system saturates, the amplitudes can converge or even overshoot which leads to the transient behavior seen in 6.15.

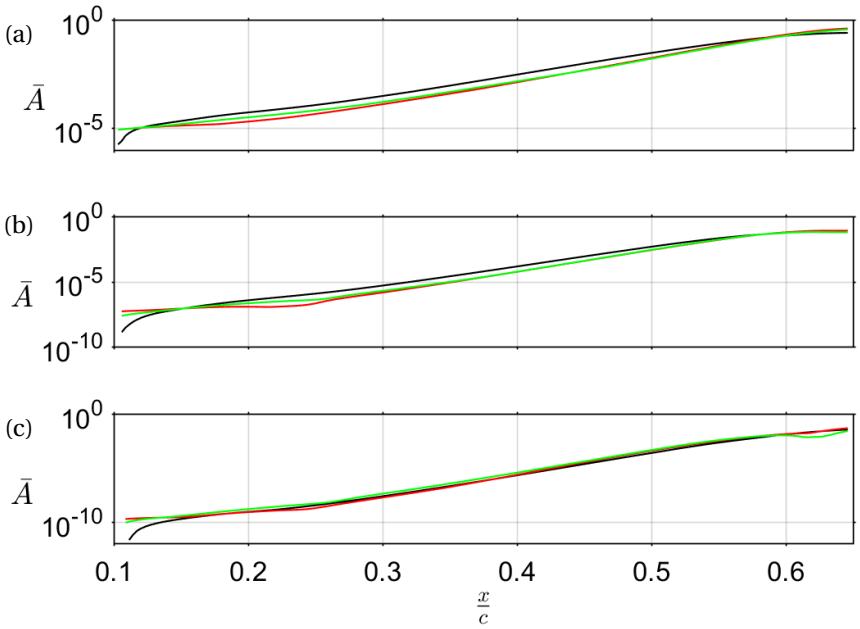

Figure 6.33: Amplitudes on a logarithmic scale for the (a) second harmonic, (b) third harmonic and (c) fourth harmonic after introduction with methods 1 (black), 2 (green) or 3 (red).

Method 3 appears to perform best in terms of reducing initial transients as a result of consistency in growth rate and amplitude due to increased physical modeling. The amplitudes were previously plotted on a log

scale to show the initial amplitudes better. The effect of the mode introduction scheme on the final amplitude of the modes is also significant and can be seen in figure 6.34. The differences in final amplitudes between modes introduced with method 2 and 3 are still noticeable, although they are much more in accordance compared to the first method.

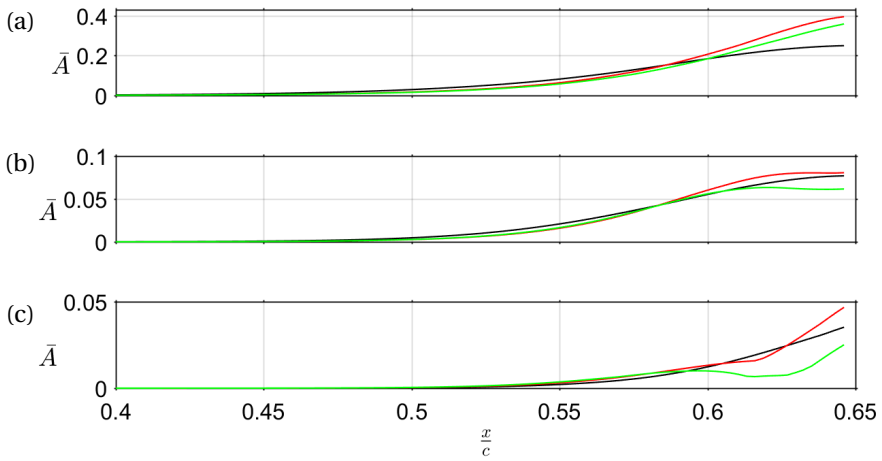

Figure 6.34: Amplitudes for the (a) second harmonic, (b) third harmonic and (c) fourth harmonic after introduction with methods 1 (black), 2 (green) or 3 (red).

Following the growth rate and amplitude plots, a method that introduces modes with a zero amplitude, i.e. ILPSE1, induces many transients that are found in [4, 8, 14, 15]. It can be considered incorrect as a result of this transient and also seen in previous results from the TS wave and crossflow simulations. Although, stating that this introduction is incorrect also downstream of the inflow contradicts the results found in the TS case and DNS comparison, where initial conditions as calculated through ILPSE1 for the second harmonic resulted in a close match with the reference despite the increased transient. It is therefore likely that transients in amplitude and growth rate are not an accurate measure of correctness in the NPSE framework downstream of the introduction stage. Introducing a mode from a zero amplitude results in an overshoot of the growth downstream of the introduction. This overshoot is compensated for by a reduced nonlinear forcing downstream resulting in a correct state of that harmonic. If undershoot occurs, the nonlinear forcing appears unable to perform this correction resulting in significantly different results downstream. As long as the overshoot occurs at a relatively small amplitude where nonlinear effects are insignificant for the primary mode evolution, results will not be affected downstream. For higher harmonics, introduction with ILPSE3 is preferred as the reduced transient causes accurate local prediction of the amplitude and growth of the harmonics.

6.5.3. Peak amplitude calculations

The initial shape function is normalized by the maximum value to achieve a partition of shape function and amplitude that allows for plotting consistency. The maximum is also used for post-processing corrections to growth rates and amplitudes. This maximum value generally does not coincide with the actual shape function peak for viable y-discretizations in NPSE simulations. This normalization thus undesirably alters the initial amplitude of the shape function. The shape of this function, however, is still known to the system due to the spectral nature of discretization in wall-normal direction. Artificially displacing the maximum to one (1) thus introduces an error if this maximum is not accurately approximating the apex of this shape. An example of this can be seen in figure 6.35(a) where the shapes were normalized based on the maximum value present in the shapes. The peak value is consistently one (1), as is enforced by normalization on the discretized shape. Performing a normalization without interpolation introduces an error of order 10^{-3} as can be seen in figure 6.35 (b). Interpolated normalization improves the method's accuracy by correctly determining the peak of a shape and normalizing for this value. We aim to improve the consistency of the introduction amplitudes and the resulting amplitude evolution plots by normalizing an interpolated peak value. This change also allowed the study in wall-normal convergence as values were not distorted by this much larger order error.

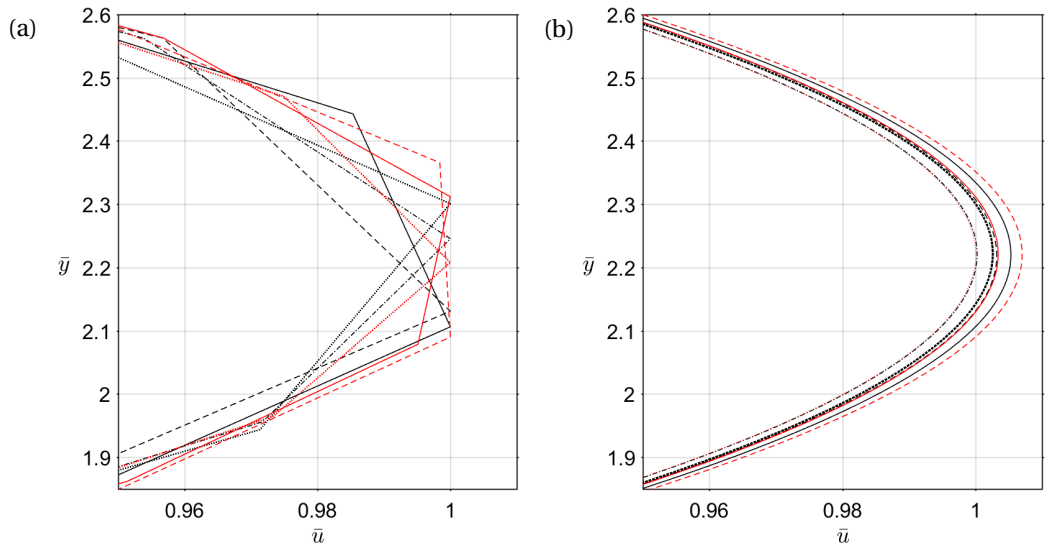

Figure 6.35: Normalized shape function peaks (a) and spline interpolation of these shape functions (b) with ny = 40 (black –), 45 (black :), 50 (black -), 55 (black .-), 60 (red –), 65 (red :) and 70 (red -).

When the shape functions are interpolated to calculate a maximum instead, results are consistent as every mode is introduced the same way. The plotted amplitude is then consistently the peak amplitude, rather than an approximation of that peak based on the nearest collocation point. The results of normalization after interpolation are shown in figure 6.36. The interpolated peaks coincide perfectly to ensure correct amplitudes of mode introductions and plotting consistency. This shape function interpolation is also performed when correcting for the amplitudes and growth rates as described in section 4.6.

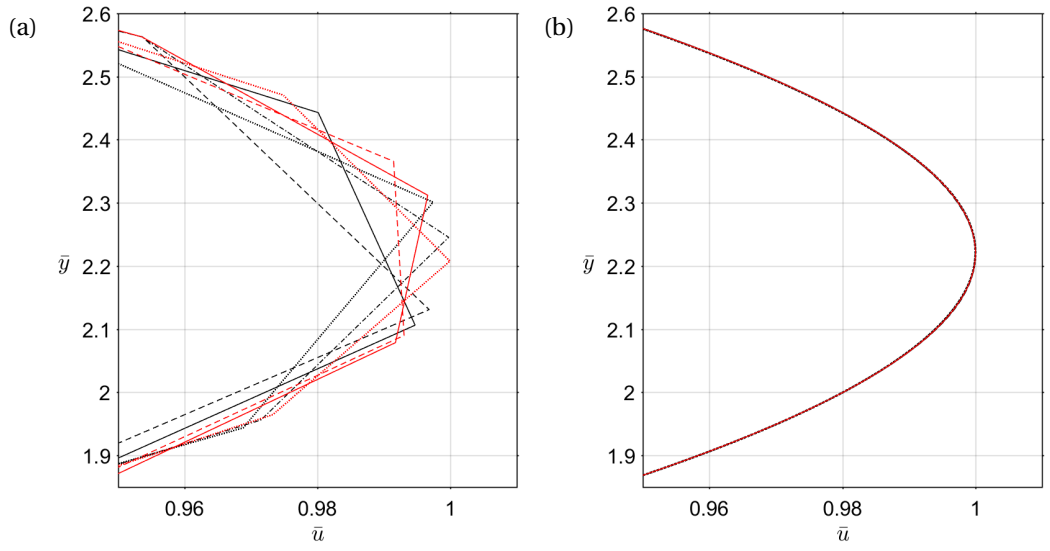

Figure 6.36: Correctly normalized shape function peaks (a) and Spline interpolation of these shape functions (b) with ny = 40 (black –), 45 (black :), 50 (black -), 55 (black .-), 60 (red –), 65 (red :) and 70 (red -).

7

Conclusion and recommendations

At the start of this thesis, two research questions and five sub-questions were posed alongside the aims for this project. This chapter gives a definitive answer to the research questions and summarizes the outcomes. Afterward, the recommendations for future work are set out.

7.1. Conclusion

The Nonlinear Parabolized Stability Equation solver is capable of accurately predicting the linear and nonlinear growth of crossflow instabilities in a swept flat plate boundary layer. In addition, a significant improvement was made on the current state-of-the-art in terms of mode introduction schemes for higher harmonics. For the NPSE tool, both a high and low-level architecture was presented. The NPSE solver was applied to a Blasius boundary layer case subjected to a TS primary instability characterized by the nondimensional frequency $F = 86(10^{-6})$ for validation. The sensitivity of the solver and the importance of mode introduction was proven here as the literature shows different results for this case, which appear to have been caused by the initial condition. Strong transients for all nonlinearly generated harmonics were seen in the reference results, which could be avoided with the novel technique presented in this thesis. Afterward, the NPSE were used to predict the nonlinear amplitude evolution of crossflow instabilities. A close match was found with DNS simulations sufficiently far from the outflow after the introduction scheme was matched numerically. At the end of the domain results start deviating which is accredited to the NPSE being subject to a coarser grid and the incorporation of fewer harmonics.

The convergence of the results was confirmed for the base flow, grid in streamwise and wall-normal direction and the number of harmonics supported by the system. Every convergence study showed stronger local differences in the nonlinear regime. The study into streamwise grid convergence was limited by the need for small spatial steps to converge the nonlinear regime while also requiring large spatial steps to avoid the effects of residual ellipticity present in the system. This conflicting demand for spatial step size prevents the solver from achieving an accuracy below $\mathcal{O}(10^{-4})$. This is the main limitation of the NPSE when simulating the evolution of the nonlinear regime due to rapid changes for all modes. Nevertheless, this accuracy is expected to be sufficient for transition prediction or correlation studies in future work.

What is a feasible high-level and low-level architecture of an NPSE solver?
A high-level architecture was presented that shows the generation of the initial condition, harmonic balancing registers and spectral differentiation matrices, followed by a marching nonlinear convergence loop. The convergence loop calculates the new forcing term and shape functions while redirecting all growth to the wavenumber. If the change of this wavenumber from one iteration to another is smaller than a predetermined convergence threshold, the loop advances to the next stage. The initial estimate of all modes for the following stage is generated using an extrapolation of the amplitude using the growth rate of the previous stage.

How can a filter be used to compare against an unrepresented mode's amplitude to determine its significance for computations?
A good indication of the nonlinear amplitude of an unrepresented mode is the forcing that other modes in the system would have on this mode. The filter is therefore based on nonlinear principles and determines the relevance of new modes based on the amplitude of the modes that would force this mode nonlinearly.
How can the initial condition be generated and what is its effect on the amplitude evolution?
NPSE simulations should start in the linear regime, i.e. a region where the primary mode is unaffected by other modes in the system, so that the initial condition can be generated linearly. This is a prerequisite since the harmonics are unknown. If the NPSE is initiated at finite amplitudes, the nonlinear interactions of modes are ignored and harmonics are introduced rapidly. This introduces errors at the inflow that will affect downstream results significantly. The initial condition is preferably generated using ILST, since the WNL direct solution is accompanied by uncertainty in the eigenvalues that significantly affect the introduction amplitude of forced modes and subsequent evolution of all modes.

How can newly forced modes be introduced while accounting for nonparallel and nonlinear effects?
The importance of mode introduction schemes was studied by varying the model that describes the history of the nonlinearly generated modes. Neglecting physics during the introduction of harmonics causes strong initial transients that are most noticeable in the amplitude and growth rates as the nonlinear forcing corrects the mode amplitude. The nonlinear terms that force these modes can be inaccurate when many modes are all introduced incorrectly in close proximity of each other. This results in a significant error downstream of the introduction. The second harmonics appears to require an overshoot at the initial condition to converge to the correct amplitude downstream of this inflow. The preferred method for higher harmonics is the newly introduced ILPSE3 that reduces all transients and uses wavenumber averaging followed by an ILPSE step. In this ILPSE, the growth rate is used to describe the amplitude prior to its introduction via a first-order backward Euler approach. The shape function change is of a much smaller order is assumed invariant in this model. This method could not be performed in this form for the mean flow distortion because the wavenumber for this mode is zero. Instead, the previous stage for this mode is assumed to be zero. This results in an underestimation of its amplitude initially and its effect on downstream results is currently unknown. The forcing of higher harmonics is performed on the mean flow, rather than the base flow to account for the effect of the mean flow distortion on this mode during its introduction. The mean flow distortion is added to the left-hand side, which is allowed as it follows the boundary layer equations.

Do the results of the NPSE solver compare to DNS results and what is the cause of possible discrepancies between the two? A DNS and NPSE simulation was performed on a DNS base flow. The DNS inflow boundary condition is perturbed by a local ILST mode. The DNS forces the harmonics and the mean flow distortion immediately after this inflow plane and an identical transient can be seen as an ILPSE1 mode introduction where a zero amplitude is assumed at the previous stage. Given the sensitivity of stability analyses, the mode introduction was adjusted in the NPSE to match the DNS in a numerical sense by introducing the second harmonic with ILPSE1, i.e. an assumed zero amplitude in the previous stage. After this numerical matching of the initial condition, the DNS and NPSE match closely for the linear and nonlinear domain. The match deteriorates near the outflow when saturation of the modes occurs. The NPSE has a limited spatial resolution due to residual ellipticity in the system. This means that a relatively coarse streamwise discretization had to be retained in the strongly nonlinear regime. A reduced accuracy that is the consequence of this coarse grid is hypothesized to affect the results. In addition, the NPSE simulation was run using only eight harmonics represented through 70 collocation points in wall-normal direction. The DNS was able to capture up to 13 harmonics reliably and had 112 cells in y-direction. This is also hypothesized to have affected the results as even the highest harmonics are of significant amplitude in this regime.

An additional simulation was performed where the second harmonic was also imposed at the inflow boundary of the DNS. This second harmonic was calculated via the ILPSE3 model in the NPSE and extrapolated upstream to the inflow plane. The DNS is not significantly affected by this change away from the direct influence of the inflow boundary and the presence of higher harmonics is visible in the second harmonic. The NPSE shows very different results following this introduction. This result shows that a zero amplitude initial condition for the second harmonic is necessary to converge to the correct amplitude sufficiently far from the inflow. Higher harmonics can be introduced via ILPSE3.

7.2. Recommendations

The NPSE, despite significant improvements over earlier iterations of stability analysis tools, have its limitations and improvements can be made concerning robustness, physical modeling and accuracy.

The application of the weakly nonparallel stability analysis could not be confirmed for crossflow instabilities due to an uncertainty found from its application to the TS case. Two eigenvalues resulted from the direct solution of the weakly nonparallel stability equations as shown also in [3] for a TS case. The nature of the two WNL results was significantly different and neither is expected to be correct. Further research must be done to filter the results or solve the equations sequentially to generate a solution to be used for the initial condition of the NPSE marching algorithm.

Forced mode introduction for the mean flow distortion is lacking a method to account for the history of this mode. An ILPSE method that assumed an equal amplitude of the introduction stage and the stage preceding introduction, would not require a growth rate for a first-order backward approximation of the amplitude. The system of the ILPSE became ill-posed in this case. Neglecting growth in the initial stage in combination with the assumption that the shape function did not change, results in the term $\frac{\partial q}{\partial x}$ to be exactly zero. For the mean flow distortion, the wavenumbers are also zero and this results in a singular left-hand side. Consequently, this mode is introduced from an amplitude of zero and a strong transient after introduction remains present. The effect of this error could be significant downstream, despite the other modes being introduced correctly which could result in a correction of the MFD. From experience with the second harmonic, however, which is also predominantly forced by the primary mode, we see that results can still differ greatly after the introduction. The introduction should be improved to ensure a minimal error at any point in the simulation. When the mean flow distortion can be introduced in the system without introduction error, its physical accuracy can be tested alongside the ILPSE introduction method for oscillatory modes presented in this thesis. This test could be the repeated simulation of one case, starting at different locations in the linear regime for the primary mode. If the mode introduction is physical, the downstream results should be consistent, i.e. the results should not depend on the (linear) starting location.

Two options are currently hypothesized to allow the mean flow distortion to be introduced correctly. The first method concerns a damping term in the ILPSE1 formulation that reduces the importance of the zero assumption prior to the introduction. This method can easily be tested in the current framework. The second method concerns a predictor-corrector method where the mean flow distortion is introduced from zero initially. Then, this result is used as the new estimate for the previous stage until the amplitude converges for the introduction stage. Small changes between the introduction stage and the preceding stage should prevent the system from becoming ill-posed as was seen when the streamwise derivative of this mode was neglected.

Concerning the mode introduction of oscillatory modes, an investigation into the absolute and relative importance of amplitude and wavenumber estimates should be performed. This means that introductions should be generated with varying amplitudes accompanied by a constant growth rate and vice versa. Since the goal is to provide a physical initial condition, experimental research into the forcing of higher harmonics in the linear region for the primary mode is necessary. The DNS suffers from similar problems at the inflow and cannot be used for this purpose. It is hypothesized that the NPSE can be manipulated for backward marching. Or inverse marching, i.e. the backward extrapolation of results from a forward marched solution. This means that introduction errors could be washed out using repetitive alternating backward and forward marching. Whether the equations are well-posed for this purpose is currently unknown. The numerical scheme would have to be adjusted significantly to test this. If the NPSE are able to perform this marching technique, the NPSE could correct introduction errors in an elliptical fashion, similar to a DNS.

During the NPSE simulation, convergence is checked by calculating the maximum difference between all wavenumbers between iterations and only the maximum of these values is considered for the criterion. This means that all modes are reconsidered in the next iteration until the highest harmonic is converged. The primary mode, however, converges rapidly compared to the highest harmonic. In addition, the highest harmonic suffers from information asymmetry per definition of the spectral domain and is the hardest to converge. Its convergence dominates the threshold comparison. An adjustment could be made that locks converged modes temporarily or permanently and only iterates unconverged modes, possibly resulting in a significant decrease in simulation time. An example would be a (repetitive) convergence cascade from the primary mode to the highest harmonic.

During the development of the NPSE tool, the $\frac{\partial p}{\partial x}$ term could not be set directly to zero as is suggested by Li and Malik [23]. Instead, the term was suppressed by a factor 500 to ensure numerical convergence. The effects of this factor were not analyzed given that setting it to zero was proven to have no significant effects according to Li and Malik [23]. An investigation should be done into the effects of this factor for accuracy and numerical convergence. Besides, the reason why setting the $\frac{\partial p}{\partial x}$ term to zero directly resulted in an ill-posed system of equations, should be found as it might be indicative of a difference between the two codes.
The DNS suffered from inaccurate mode introduction too when imposing only the primary mode at the inflow. The importance of the nonlinear introduction of harmonics was shown on multiple occasions for both TS and CFI simulations. The DNS, however, was able to converge to the same result when the second harmonic was imposed on the inflow as well. It is a boundary value problem, and not an initial value problem, that is fully elliptic and can correct (partly) for introduction errors in time. Still, the initial condition showed a transient. Further research into DNS inflow conditions for transition analyses should be performed.

Bibliography

[1] Anderson, J. D. (2001). Fundamentals of aerodynamics. Boston: McGraw-Hill.

[2] Anderson Jr, J. D. (2005). Ludwig Prandtl's boundary layer. Physics Today, 58(12), 42-48.

[3] Bertolotti, F. P. (1991). Linear and nonlinear stability of boundary layers with streamwise varying properties(Ph. D. Thesis).

[4] Bertolotti, F. P., Herbert, T., & Spalart, P. R. (1992). Linear and nonlinear stability of the Blasius boundary layer. Journal of fluid mechanics, 242, 441-474.

[5] Bippes, H., & Lerche, T. (1997). Transition prediction in three-dimensional boundary-layer flows unstable to crossflow instability. Washington, D.C: AIAA.

[6] Boiko, A. V., Dovgal, A. V., Grek, G. R., & Kozlov, V. V. (2011). Physics of Transitional Shear Flows: Instability and Laminar–Turbulent Transition in Incompressible Near-Wall Shear Layers (Vol. 98). Springer Science & Business Media.

[7] Casacuberta, J., Groot, K. J., Ye, Q., & Hickel, S. (2019). Transitional Flow Dynamics Behind a Micro-Ramp. Flow, Turbulence and Combustion, 1-20.

[8] Chang, C.-L., Malik, M. R., Erlebacher, G., & Hussaini, M. Y. Linear and nonlinear PSE for compressible boundary layers, Linear and nonlinear PSE for compressible boundary layers (1994). Hampton, VA: National Aeronautics and Space Administration, Langley Research Center.

[9] Criminale, W. O., Jackson, T. L., & Joslin, R. D. (2019). Theory and computation of hydrodynamic stability. Cambridge, United Kingdom: Cambridge University Press.

[10] Crouch, J. D. (1992). Localized receptivity of boundary layers. Physics of Fluids A: Fluid Dynamics, 4(7), 1408–1414. doi: 10.1063/1.858416

[11] Goldstein, M. E. (1985). Scattering of acoustic waves into Tollmien-Schlichting waves by small streamwise variations in surface geometry. Journal of Fluid Mechanics, 154, 509-529.

[12] Groot, K. J. (2018). BiGlobal Stability of Shear Flows: Spanwise & Streamwise Analyses (Doctoral dissertation, Delft University of Technology).

[13] Hallbäck, M., Henningson, D. S., Johansson, A. V., & Alfredsson, P. H. (Eds.). (2013). Turbulence and Transition Modelling: Lecture Notes from the ERCOFTAC/IUTAM Summerschool Held in Stockholm, 12–20 June, 1995 (Vol. 2). Springer Science & Business Media.

[14] Haynes, T. S., & Reed, H. L. (2000). Simulation of swept-wing vortices using nonlinear parabolized stability equations. Journal of Fluid Mechanics, 405, 325-349.

[15] Herbert, T. (1997). Parabolized stability equations. Annual Review of Fluid Mechanics, 29(1), 245-283.

[16] Herbert, T. (1993) Parabolized Stability Equations. AGARD: Special Course on Progress in Transition Modelling, AGARD-R-d793(4), 4-17 – 4-21.

[17] Hickel, S., Egerer, C. P., & Larsson, J. (2014). Subgrid-scale modeling for implicit large eddy simulation of compressible flows and shock-turbulence interaction. Physics of Fluids, 26(10), 106101.

[18] Ingen (van), J. (2008). The eN Method for Transition Prediction. Historical Review of Work at TU Delft. 38th Fluid Dynamics Conference and Exhibit. doi:10.2514/6.2008-3830

[19] Kotsonis, M. (2018). Laminar Wing Project. Unpublished report, Delft University of Technology, The Netherlands.

[20] Kerschen, Edward J. (1993). Boundary Layer Receptivity Theory. Proc. 3rd. Congr. Fluid Mech. Cairo. 21. 20. 10.1115/1.3120795.

[21] Klebanoff, P. S., Tidstrom, K. D., & Sargent, L. M. (1962). The three-dimensional nature of boundary-layer instability. Journal of Fluid Mechanics, 12(1), 1-34.

[22] Kovasznay, L. S. G. (1962). Ludwig Prandtl: Gesammelte Abhandlungen zur angewandten Mechanik, Hydro und Aerodynamik. Edited by W. T OLLMIEN , H. S CHLICHTING , H. G ORTLER and F. W. R IEGELS . Springer-Verlag, 1961. 1620 pp. in 3 vols. DM. 273, paper covers; DM. 288, linen. Journal of Fluid Mechanics, 14(04), 635. doi: 10.1017/s0022112062241493

[23] Li, F., & Malik, M. R. (1996). On the nature of PSE approximation. Theoretical and Computational Fluid Dynamics, 8(4), 253-273.

[24] Liepmann, H. W. (1943). Investigations on laminar boundary-layer stability and transition on curved boundaries (No. NACA-WR-W-107). CALIFORNIA INST OF TECH PASADENA.

[25] J. S. Luo & H. Zhou.John Trevor Stuart. (1987, February 24). On the generation of Tollmien-Schlichting waves in the boundary layer of a flat plate by the disturbances in the free stream413Proceedings of the Royal Society of London. A. Mathematical and Physical Sciences. https://doi.org/10.1098/rspa.1987.0119

[26] Malik, M., Li, F., & Chang, C. (1994). Crossflow disturbances in three-dimensional boundary layers: Nonlinear development, wave interaction and secondary instability. Journal of Fluid Mechanics,268, 1-36. doi:10.1017/S0022112094001242

[27] Mack, L. M. (1984). Boundary-Layer Linear Stability Theory. In Boundary-Layer Linear Stability Theory. Ft. Belvoir: Defense Technical Information Center.

[28] J.M. McDonough, Introductory Lectures on Turbulence, Physics, Mathematics and Modeling, University of Kentucky, Departments of Mechanical Engineering and Mathematics, 2007.

[29] Meersman, John & Hader, Christoph & Fasel, H. (2018). Hypersonic Boundary-Layer Transition: Comparison of the Fundamental Resonance Breakdown for a Flared and Straight Cone at Mach 6. 10.2514/6.2018-3851.

[30] Monkewitz, P. A. (1988). Subharmonic resonance, pairing and shredding in the mixing layer. Journal of Fluid Mechanics, 188, 223-252.

[31] Nair, M. T., & Singh, A. (2018). Linear Algebra. Singapore: Spinger Nature. doi: https://doi.org/10.1007/978-981-13-0926-7_2

[32] Oliviero, N. B., & Reed, H. L. (2015). EPIC: A New and Advanced Nonlinear Parabolized Stability Equation Solver (Unpublished master's thesis). Texas A&M University.

[33] Örley, F., Pasquariello, V., Hickel, S., & Adams, N. A. (2015). Cut-element based immersed boundary method for moving geometries in compressible liquid flows with cavitation. Journal of Computational Physics, 283, 1-22.

[34] Paredes, P., Hanifi, A., Theofilis, V., & Henningson, D. S. (2015). The Nonlinear PSE-3D Concept for Transition Prediction in Flows with a Single Slowly-varying Spatial Direction. Procedia IUTAM, 14, 36–44. doi: 10.1016/j.piutam.2015.03.021

[35] Pope, S. B. (2015). Turbulent flows. Cambridge: Cambridge University Press.

[36] Riedel, H., & Sitzmann, M. (1998). In-flight investigations of atmospheric turbulence. Aerospace Science and technology, 2(5), 301-319.

[37] Ruban, A. I. (1984). On the generation of Tollmien-Schlichting waves by sound. Fluid Dynamics, 19(5), 709-717.

[38] Saric, W. S., & Reed, H. L. (2003). Crossflow instabilities: theory and technology. In Crossflow instabilities: theory and technology. Reston: AIAA.

[39] Saric, W. S., Reed, H. L., & White, E. B. (2003). Stability Andtransition Ofthree-Dimensionalboundarylayers. Annual Review of Fluid Mechanics, 35(1), 413–440. doi: 10.1146/annurev.fluid.35.101101.161045

[40] H. Schlichting (Deceased), & Gersten, K. (2018). Boundary-Layer Theory. Berlin: Springer Berlin. doi:10.1007/978-3-662-52919-5

[41] Schmid, P. J., & Henningson, D. S. (2012). Stability and transition in shear flows (Vol. 142). Springer Science & Business Media.

[42] Schubauer, G. B., & Skramstad, H. K. (1948). Laminar-boundary-layer oscillations and transition on a flat plate (No. NACA-909). NATIONAL AERONAUTICS AND SPACE ADMINISTRATION WASHINGTON DC.

[43] Serpieri, J. (2018). Cross-Flow Instability: Flow diagnostics and control of swept wing boundary layers. https://doi.org/10.4233/uuid:3dac1e78-fcc3-437f-9579-048b74439f55

[44] U.S.Cong. (1999). Crossflow stability and transition experiments in swept-wing flow (J. R. Dagenhart, Author) [Cong. Rept.]. Hampton, VA: National Aeronautics and Space Administration, Langley Research Center.

[45] Westerbeek, S. H. J. (2019, April 4). Boundary Layer Transition: A Literature Study. Unpublished course work for AE4020. Delft.

[46] White, F.M. and Corfield, I. (2006) Viscous Fluid Flow. Vol. 3, McGraw-Hill, New York.

[47] D. Zuck, Osborne Reynolds, 1842-1912, AND THE FLOW OF FLUIDS THROUGH TUBES, BJA: British Journal of Anaesthesia, Volume 43, Issue 12, December 1971, Pages 1175–1182, https://doi.org/10.1093/bja/43.12.1175

A

NPSE system of equations

$$\mathbb{L} = \begin{bmatrix} \mathrm{DEL} + \frac{\partial \bar{U}}{\partial x} & \frac{\partial \bar{U}}{\partial \eta} & 0 & i\bar{\alpha} \\ \frac{\partial \bar{V}}{\partial \bar{x}} & \mathrm{DEL} + \frac{\partial \bar{V}}{\partial \eta} & 0 & D_1 \\ \frac{\partial \bar{W}}{\partial \bar{x}} & \frac{\partial \bar{W}}{\partial \bar{\eta}} & \mathrm{DEL} & i\bar{\beta} \\ i\bar{\alpha} & D_1 & i\bar{\beta} & 0 \end{bmatrix} \tag{A.1a}$$

$$\mathbb{M} = \begin{bmatrix} \bar{U} - \frac{2i\bar{\alpha}}{Re} & 0 & 0 & I \\ 0 & \bar{U} - \frac{2i\bar{\alpha}}{Re} & 0 & 0 \\ 0 & 0 & \bar{U} - \frac{2i\bar{\alpha}}{Re} & 0 \\ I & 0 & 0 & 0 \end{bmatrix} \tag{A.1b}$$

$$\mathbb{N} = \begin{bmatrix} -\frac{i}{Re} & 0 & 0 & 0 \\ 0 & -\frac{i}{Re} & 0 & 0 \\ 0 & 0 & -\frac{i}{Re} & 0 \\ 0 & 0 & 0 & 0 \end{bmatrix} \tag{A.1c}$$

$$\bar{r} = \begin{bmatrix} -i\bar{\alpha}\bar{u}^2 - \bar{u}\frac{\partial \bar{u}}{\partial \bar{x}} - \bar{v}\frac{\partial \bar{u}}{\partial \eta} - i\bar{\beta}\bar{w}\bar{u} \\ -i\bar{\alpha}\bar{u}\bar{v} - \bar{u}\frac{\partial \bar{v}}{\partial \bar{x}} - \bar{v}\frac{\partial \bar{v}}{\partial \eta} - i\bar{\beta}\bar{w}\bar{v} \\ -i\bar{\alpha}\bar{u}\bar{w} - \bar{u}\frac{\partial \bar{w}}{\partial \bar{x}} - \bar{v}\frac{\partial \bar{w}}{\partial \eta} - i\bar{\beta}\bar{w}^2 \\ 0 \end{bmatrix} \tag{A.1d}$$

B

Scripts and high-level architecture

B.1. High-level architecture

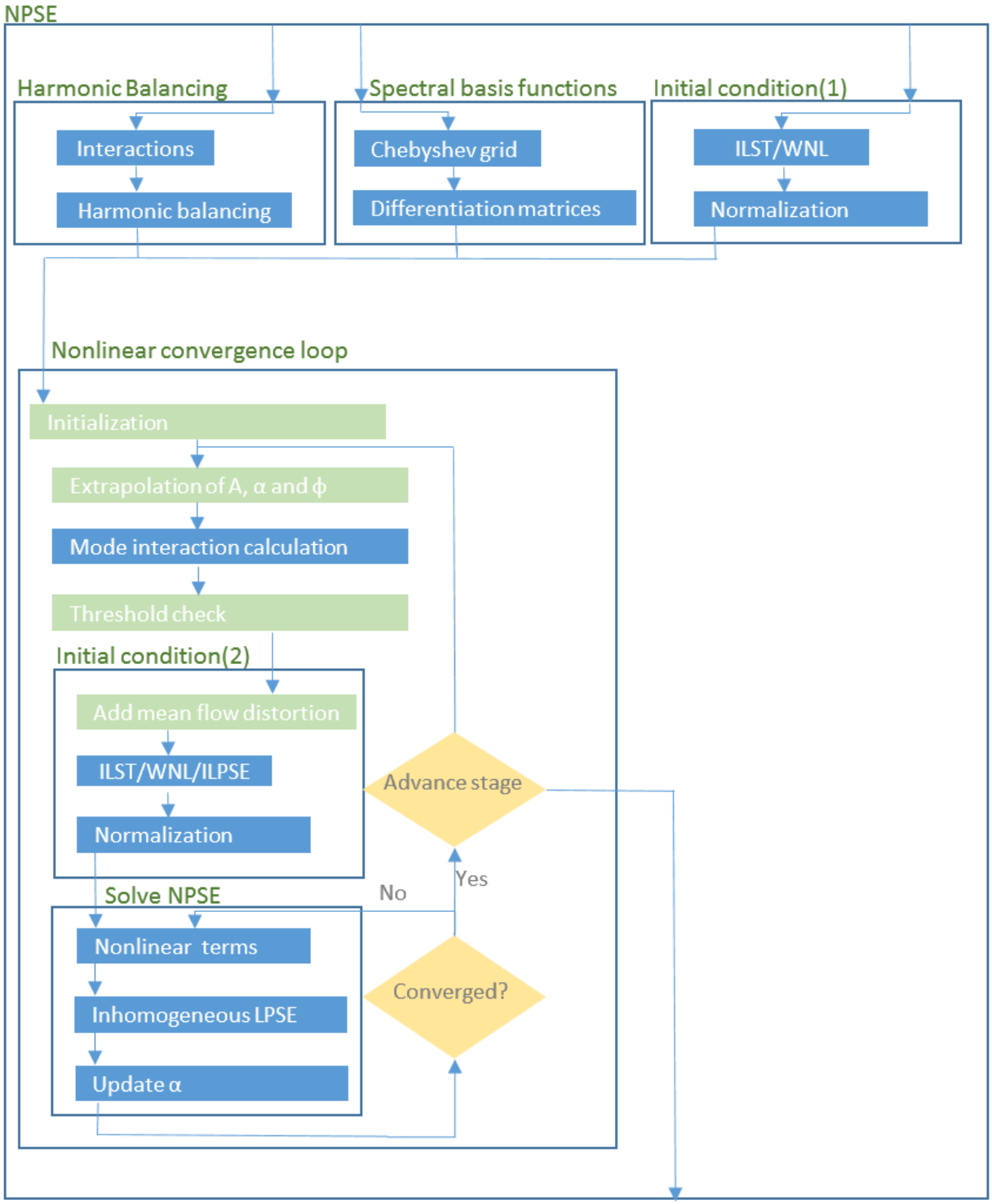

Figure B.1: High-level architecture of the NPSE solver.

B.2. Mint.m

```
function [Nmat, Mmat, Modevec] = Mint(N,M)
% mint (Mode INTeractions) is a script that sets up a matrix containing the
% modes affected by the interactions of all currently represented modes

% Outputs Mmat and Nmat are mode numbers for beta and omega respectively.
% Output Modevec is the mode vector [m(1:2M+1);n(1:2M+1)] for every mode
% counter l_{m,n}.

%% mint
%M = 1; %Testvalue
%N = 1; %Testvalue
L = (2*N+1)*(2*M+1); %Counter

%initialize basic building blocks (m,n)
M1 = -M:1:M; %First loop through M
N1 = -N.*ones(1,2*N+1); %N is the second entry
Nvec = [];
Mvec = [];
for i = 1:2*M+1 %Append matrix to simulate subscript counting, M -> N
    Mvec = [Mvec M1];
end
for i = 1:2*N+1 %Append matrix adding 1 each time to simulate subscript counting, M -> N
    Nvec = [Nvec N1+i-1];
end
Modevec = [Mvec;Nvec];

%initalize matrices
Nmat = zeros(2*N+1);
Mmat = zeros(2*N+1);

for i = 1:L
    for j = 1:L
        Nmat(i,j) = Nvec(i)+Nvec(j);
    end
end
for i = 1:L
    for j = 1:L
        Mmat(i,j) = Mvec(i)+Mvec(j);
    end
end
end % end of function
```

B.3. HBalancing.m

```
function [ HB ] = Hbalancing(M, N, Mmat, Nmat, Modevec )
%Hbalancing creates multiplication matrices that will be used to calculate
%the source terms for the ILPSE solver
%% Inputs
%   M is the number of beta modes
%   N is the number of omega modes
%   Mmat contains the m part of the modes affected by the mode interactions
%   Nmat contains the n part of the modes affected by the mode interactions
%   Modevec contains the m and n part of the modecounter l

%% Outputs
%   HB is a collection of [2M+1]x[2N+1] matrices of size [2M+1]x[2N+1]
%   where every matrix is a binary matrix that serves as a registry for the
%   source amplitudes that affect that respective mode. (Harmonic
%   Balancing)

L = (2*N+1)*(2*M+1);
for i = 1:L
% Read desired combination of m,n for mode i (mode l)
m=Modevec(1,i);
n=Modevec(2,i);
A = Mmat == m;    %A tells us which entry has the correct mode for m
B = Nmat == n;    %B tells us which entry has the correct mode for n
HB(:,:,i) = A.*B; %Simulates LOGIC AND, given that both are required.
end

end % end of function
```

B.4. RHS.m

```
function [ f ] = NLT(f,i,RunJ,RunSource,u,v,w,p,alpha,D1,HB,A,Amat,x_md,ny)
%NLT Calculates the nonlinear terms for every mode at stage i

iu = sqrt(-1);
global betavec nf

for j = RunJ
    dudx(:,j) = (u(:,j,i)-u(:,j,i-1))/(x_md(i)-x_md(i-1));
    dvdx(:,j) = (v(:,j,i)-v(:,j,i-1))/(x_md(i)-x_md(i-1));
    dwdx(:,j) = (w(:,j,i)-w(:,j,i-1))/(x_md(i)-x_md(i-1));
end

%Reset/initialize momentum sums
xmom = zeros(ny,nf);
ymom = zeros(ny,nf);
zmom = zeros(ny,nf);

for j = [RunJ, RunSource];%set up nonlinear terms interaction shape function
    if j ~= 0

[gharray, jkarray] = find(HB(:,:,j)); %Finds mode interaction needed

%Delete gh and jk that are unrepresented modes
gharray = ismember(gharray,RunJ).*gharray;
jkarray = ismember(jkarray,RunJ).*jkarray;
[INT,~] = size(nonzeros(gharray.*jkarray)); %If both modes are nonzero loop
R = find(gharray.*jkarray ~=0); %contain entries of nonzero interactions
%Delete zero's from arrays
gharray = gharray(R);
jkarray = jkarray(R);

for j2 = 1:INT
    % Determine interacting modes
    gh = gharray(j2); %This alpha
    jk = jkarray(j2);

    %x-momentum source terms
```

```
    uu      = u(:,gh,i) .* u(:,jk,i);
    ududx   = u(:,gh,i) .* dudx(:,jk);
    vdudy   = v(:,gh,i) .* (D1*u(:,jk,i));
    wu      = w(:,gh,i) .* u(:,jk,i);

    %y-momentum source terms
    uv      = u(:,gh,i) .* v(:,jk,i);
    udvdx   = u(:,gh,i) .* dvdx(:,jk);
    vdvdy   = v(:,gh,i) .* (D1*v(:,jk,i));
    wv      = w(:,gh,i) .* v(:,jk,i);

    %z-momentum source terms
    uw      = u(:,gh,i) .* w(:,jk,i);
    udwdx   = u(:,gh,i) .* dwdx(:,jk);
    vdwdy   = v(:,gh,i) .* (D1*w(:,jk,i));
    ww      = w(:,gh,i) .* w(:,jk,i);

    beta  = betavec(gh);

xmom(:,j) = xmom(:,j) +Amat(gh,jk)*(-iu*alpha(gh,i).*uu-ududx-vdudy-iu*beta*wu);
ymom(:,j) = ymom(:,j) +Amat(gh,jk)*(-iu*alpha(gh,i).*uv-udvdx-vdvdy-iu*beta*wv);
zmom(:,j) = zmom(:,j) +Amat(gh,jk)*(-iu*alpha(gh,i).*uw-udwdx-vdwdy-iu*beta*ww);
end

if A(j) ~= 0 %Means mode is not newly introduced
    %Note that, if A(j) = 0, the amplitude is thus contained in q and f
    xmom(:,j)=xmom(:,j)/A(j);
    ymom(:,j)=ymom(:,j)/A(j);
    zmom(:,j)=zmom(:,j)/A(j);
end

f(:,j,i) = [xmom(2:ny-1,j); ymom(1:ny-1,j); zmom(2:ny-1,j); zeros(ny,1)];

end
end

end % end of function
```

B.5. ILPSE.m

```
function [phi,u,v,w,p,ampltd] =
     solver_ILPSE(i,j,u,v,w,p,Re,Ur,Vr,Wr,dxUr,dxVr,dxWr,dyUr,dyVr,dyWr,x_md,y_md,ny,y_max,y_i,f,alpha,y,D1,D2,phi)
% Executes ILPSE (Inhomogeneous Linear Parabolized Stability Equation)
% simulation at stage i, given the mean flow (Ur,Vr,Wr). The fields are to
% be given such as to go from the free-stream to the wall as the (row-)index
% increases. The size of the v-vector here is one larger than u and v due
% to the need for a Neumann BC for the mean flow distortion for v. To have
% a uniform size of phi the Dirichlet BC is also implemented in the regular
% problem.

global nf omegavec betavec

omega = omegavec(j);
beta  = betavec(j);
% The PSDMs will generally pop up with the size (N-2)x(N-2), accordingly
% define the identity and zero column and row
I     = eye(ny-2);
Zc    = zeros(ny-2,1);
Zr    = zeros(1,ny-2);

%Make a new array phisub and RHS for manipulating size
RHS = f(:,j,i);
phisubo = phi(:,j,i-1);
phisub = phi(:,j,i);

%% Calculate base flow components
iu=sqrt(-1);
stabon = false;
    % Interpolate base flow components and create diagonal matrix form
      U = diag(interp1(y_md, Ur(:,i),y(2:ny-1),'spline'));
```

```
30      dxU = diag(interp1(y_md,dxUr(:,i),y(2:ny-1),'spline'));
31      dyU = diag(interp1(y_md,dyUr(:,i),y(2:ny-1),'spline'));
32
33        V = diag(interp1(y_md, Vr(:,i),y(2:ny-1),'spline'));
34      dxV = diag(interp1(y_md,dxVr(:,i),y(2:ny-1),'spline')); % note that this term is order 1/Re^2
35      dyV = diag(interp1(y_md,dyVr(:,i),y(2:ny-1),'spline'));
36
37        W = diag(interp1(y_md, Wr(:,i),y(2:ny-1),'spline'));
38      dxW = diag(interp1(y_md,dxWr(:,i),y(2:ny-1),'spline'));
39      dyW = diag(interp1(y_md,dyWr(:,i),y(2:ny-1),'spline'));
40
41         %Interpolate base flow components and create diagonal matrix form
42      %Including freestream values for MFD calculations
43      Uf   = diag(interp1(y_md, Ur(:,i),y(1:ny),'spline'));
44      dxUf = diag(interp1(y_md,dxUr(:,i),y(1:ny),'spline'));
45      dyUf = diag(interp1(y_md,dyUr(:,i),y(1:ny),'spline'));
46
47        Vf = diag(interp1(y_md, Vr(:,i),y(1:ny),'spline'));
48      dxVf = diag(interp1(y_md,dxVr(:,i),y(1:ny),'spline')); % note that this term is order 1/Re^2
49      dyVf = diag(interp1(y_md,dyVr(:,i),y(1:ny),'spline'));
50
51        Wf = diag(interp1(y_md, Wr(:,i),y(1:ny),'spline'));
52      dxWf = diag(interp1(y_md,dxWr(:,i),y(1:ny),'spline'));
53      dyWf = diag(interp1(y_md,dyWr(:,i),y(1:ny),'spline'));
54
55      If     = eye(ny);
56      Zcf    = zeros(ny,1);
57      Zrf    = zeros(1,ny);
58
59         % Compile common convection-diffusion terms
60         Del = -iu*omega*I + iu*alpha(j,i)*U + iu*beta*W + I*(alpha(j,i)^2 +
               beta^2)/Re+V*D1(2:end-1,2:end-1)-D2(2:end-1,2:end-1)/Re;
61         Delf = -iu*omega*If + iu*alpha(j,i)*Uf + iu*beta*Wf + If*(alpha(j,i)^2 + beta^2)/Re+Vf*D1-D2/Re;
62         Delf2 = Delf(1:end-1,1:end-1);
63
64      % Define A in A*q + B*(q-qp)/dx + C*q*dalpha/dx = 0
65      %u         ve   v               w      pe  p pw
66  A = [Del+dxU dyUf(2:end-1,2:end-1) 0*I   iu*alpha(j,i)*If(2:end-1,:)
67  dxVf(2:end-1,2:end-1) Delf(2:end-1,2:end-1)+dyVf(2:end-1,2:end-1) ...
                                              0*If(2:end-1,2:end-1) D1(2:end-1,:)
68             dxW       dyWf(2:end-1,2:end-1)   Del  iu*beta*If(2:end-1,:)
69      If(:,2:end-1)*alpha(j,i)*iu D1(:,2:end-1) If(:,2:end-1)*beta*iu If(:,:)*0];
70
71
72          % Define B in A*q + B*(q-qp)/dx + C*q*dalpha/dx = 0
73  B = [U-I*(2*alpha(j,i)*iu)/Re If(2:end-1,2:end-1)*0 I*0 If(2:end-1,:) [0 Zr 0]
74      If(2:end-1,2:end-1)*0   Uf(2:end-1,2:end-1)-If(2:end-1,2:end-1)*(2*alpha(j,i)*iu)/Re ...
                                    If(2:end-1,2:end-1)*0 If(2:end-1,:)*0
75      I*0         If(2:end-1,2:end-1)*0 U-I*(2*alpha(j,i)*iu)/Re           If(2:end-1,:)*0
76      If(:,2:end-1)       If(:,2:end-1)*0     If(:,2:end-1)*0   If(:,:)*0];
77
78
79
80        % Define C in A*q + B*(q-qp)/dx + C*q*dalpha/dx = 0
81  C = [-I*(iu/Re) If(2:end-1,2:end-1)*0      I*0       If(2:end-1,:)*0
82  If(2:end-1,2:end-1)*0 -If(2:end-1,2:end-1)*(iu/Re) If(2:end-1,2:end-1)*0 If(2:end-1,:)*0
83      I*0         If(2:end-1,2:end-1)*0 -I*(iu/Re) If(2:end-1,:)*0
84      If(:,2:end-1)*0 If(:,2:end-1)*0 If(:,2:end-1)*0       If(:,:)*0];
85
86
87          if j== round(nf/2) %MFD
88
89             %u       ve   v                    w      pe  p pw
90  A = [Del+dxU   dyUf(2:end-1,1:end-1)  0*I   iu*alpha(j,i)*If(2:end-1,:)
91      dxVf(1:end-1,2:end-1) Delf(1:end-1,1:end-1)+dyVf(1:end-1,1:end-1) ...
            0*If(1:end-1,2:end-1) D1(1:end-1,:)
92      dxW       dyWf(2:end-1,1:end-1)   Del  iu*beta*If(2:end-1,:)
93      If(:,2:end-1)*alpha(j,i)*iu D1(:,1:end-1) If(:,2:end-1)*beta*iu If(:,:)*0];
94
95
96          % Define B in A*q + B*(q-qp)/dx + C*q*dalpha/dx = 0
```

```
B = [U-I*(2*alpha(j,i)*iu)/Re If(2:end-1,1:end-1)*0 I*0 If(2:end-1,:)/500
     If(1:end-1,2:end-1)*0 Uf(1:end-1,1:end-1)-If(1:end-1,1:end-1)*(2*alpha(j,i)*iu)/Re ...
          If(1:end-1,2:end-1)*0 If(1:end-1,:)*0
     I*0        If(2:end-1,1:end-1)*0 U-I*(2*alpha(j,i)*iu)/Re           If(2:end-1,:)*0
     Zr                    0 Zr               Zr                 [0 Zr 0]
     If(2:end,2:end-1)      If(2:end,1:end-1)*0     If(2:end,2:end-1)*0   If(2:end,:)*0];


C = zeros(size(B));

        end

        % Determine dalpha/dx
      dx  =   x_md(i) - x_md(i-1);
        dax = (alpha(j,i) - alpha(j,i-1))/dx;

        if j ~= round(nf/2);
        % Right-hand side Dirichlet BC
        RHS(ny-1)  =[];
        phisub(ny-1)=[];
        phisubo(ny-1)=[];

        % Form LHS matrix and RHS vector of Inhomogeneous LPSE
        Ml = A + B/dx + C*dax;
        Mr = B/dx*phisubo + RHS;

        %Set up LU decomposition
        [MlL,MlU] = lu(Ml);

        % Solve problem
        phisub = MlL\Mr;
        phisub = MlU\phisub;

        %recreate phi with BC
        if j ~= round(nf/2)
        phi(:,j,i) = [phisub(1:ny-2); 0; phisub(ny-1:end)];
        else
        phi(:,j,i) = phisub;
        end

        % Calculate new maximum amplitude after spline interpolation
        utest = [0 ;phi(2:ny-1,j,i); 0];
        y_mdInt = linspace(10,y_md(end),1000);
        u1int = interp1(y_md,abs(utest),y_mdInt,'spline');
        [ampltd, ymax(1)] = max(abs(u1int));

        if j == round(nf/2)
        alpha(j,i) = 0; %Mode is not oscillatory and thus has no alpha.
        ampltd = 1;
        end

    u(:,j,i) = [0 ;   phi(1          :   ny-2    ,j,i); 0];
    v(:,j,i) = [      phi(ny-2    +1  : 2*(ny-2)+1 ,j,i); 0];
    w(:,j,i) = [0 ;   phi(2*(ny-2) +2 : 3*(ny-2)+1 ,j,i); 0];
    p(:,j,i) =        phi( 3*(ny-2)+2 : 4*(ny-2)+3 ,j,i);

end
```

C

Crossflow velocity contours

C.1. Linear regime

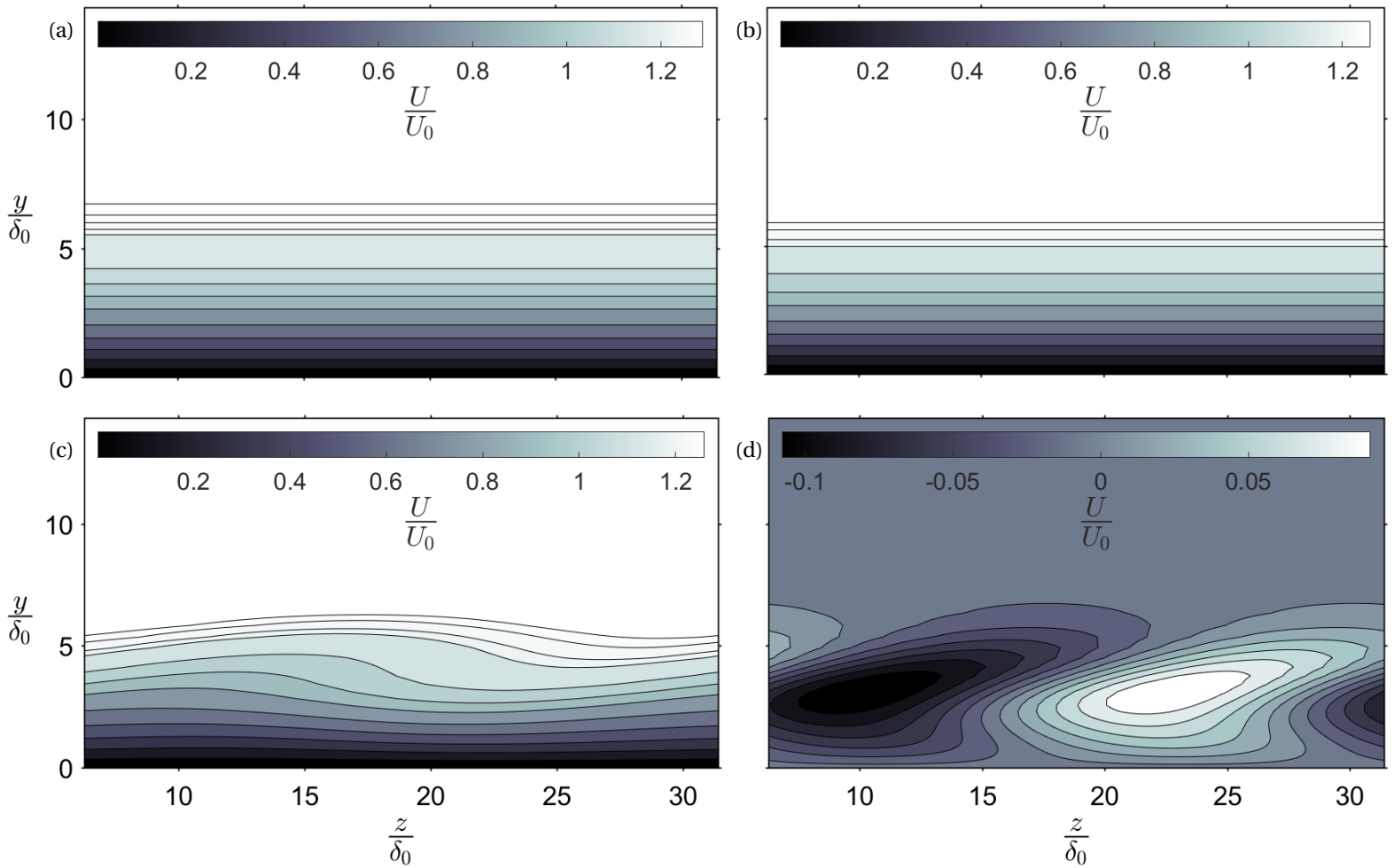

Figure C.1: U-velocity contours at $\frac{x}{c} = 0.4816$ of the (a) base flow, (b) mean flow, (c) mean flow and primary mode, (d) primary mode.

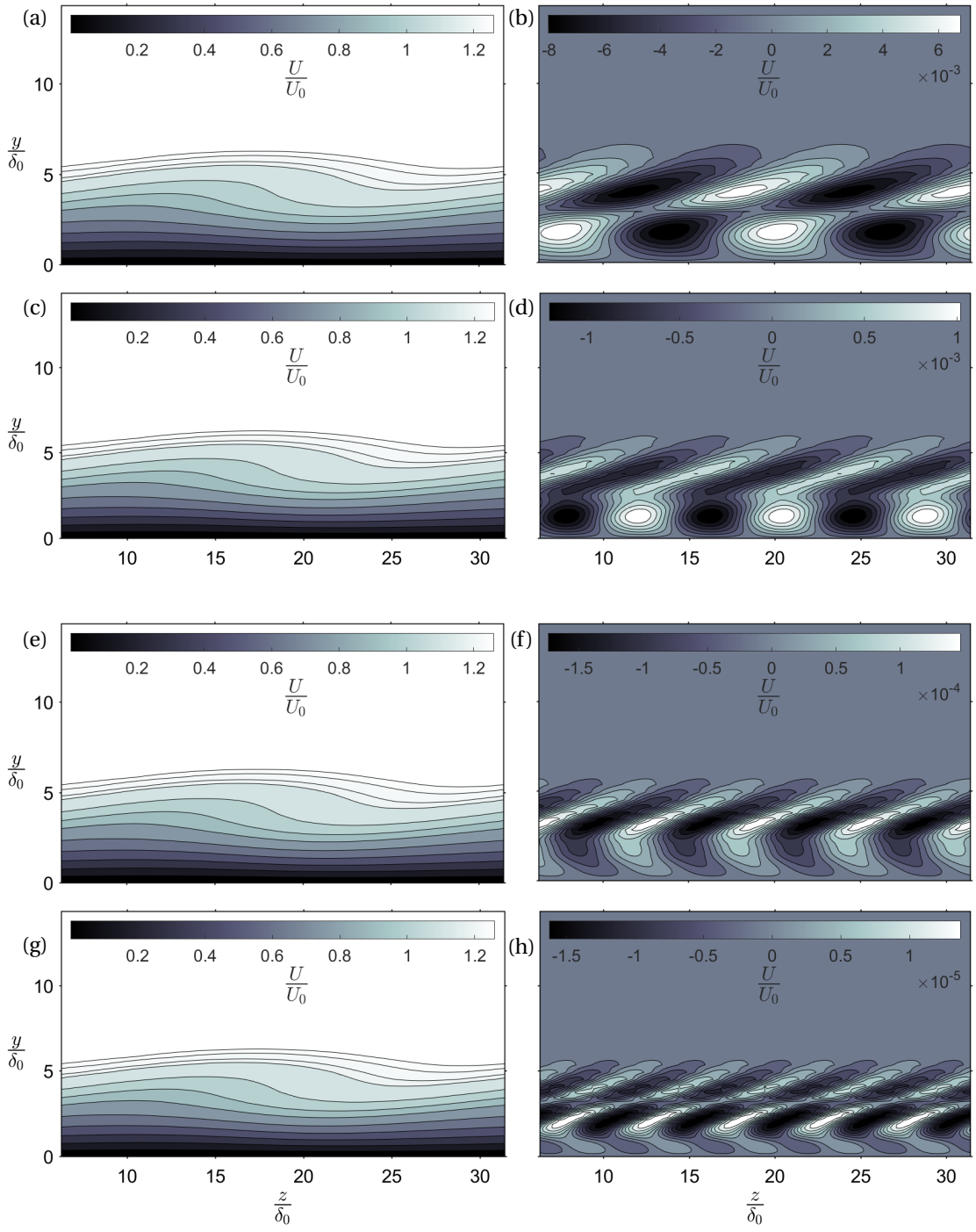

Figure C.2: U-velocity contours at $\frac{x}{c} = 0.4816$ of the mean flow and harmonics (a) 1-2 , (c) 1-3, (r) 1-4, (g) 1-5 and the isolated effect of harmonics (b) 2, (d) 3, (f) 4, (h) 5.

C.2. Weakly nonlinear regime

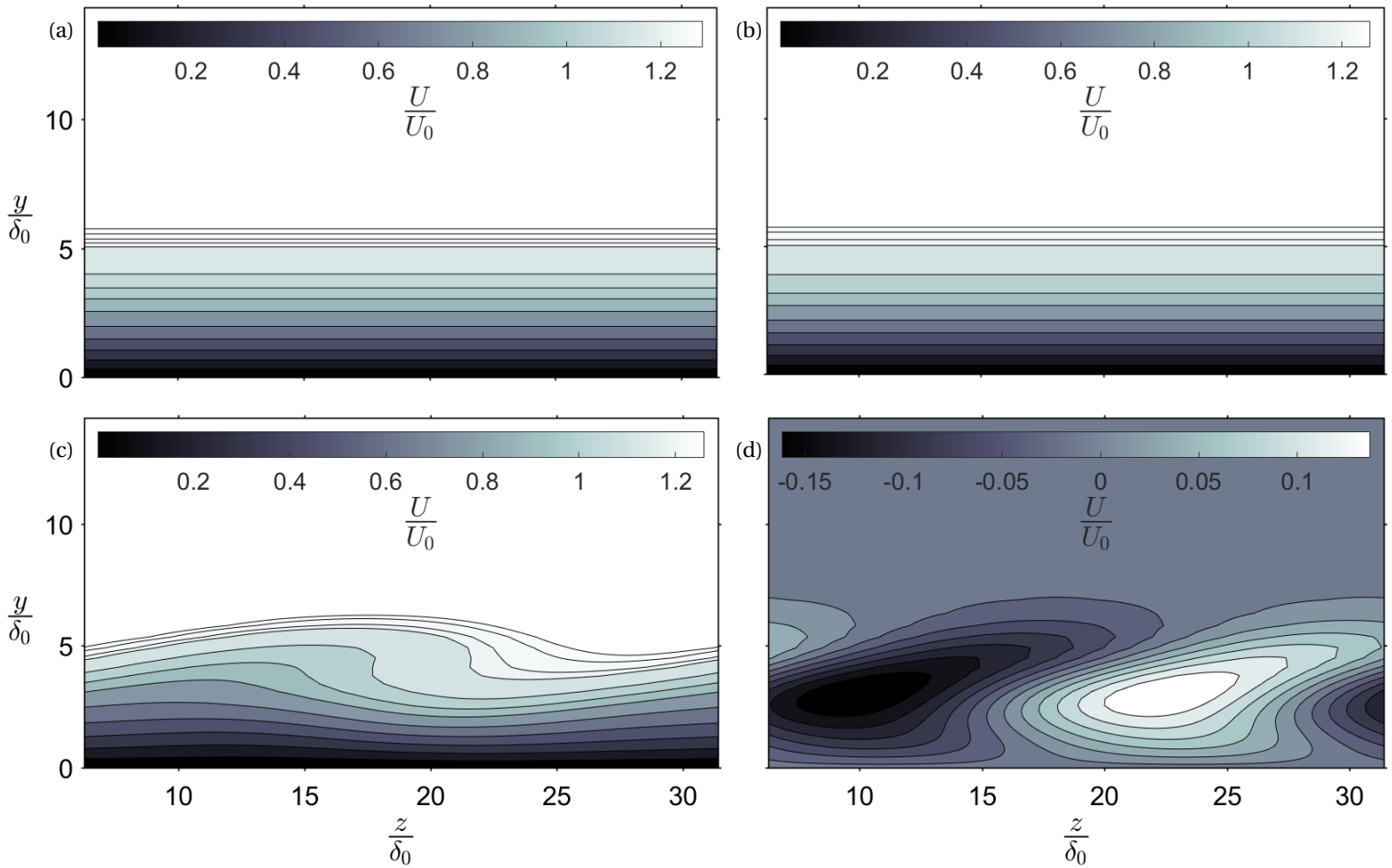

Figure C.3: U-velocity contours at $\frac{x}{c} = 0.5227$ of the (a) base flow, (b) mean flow, (c) mean flow and primary mode, (d) primary mode.

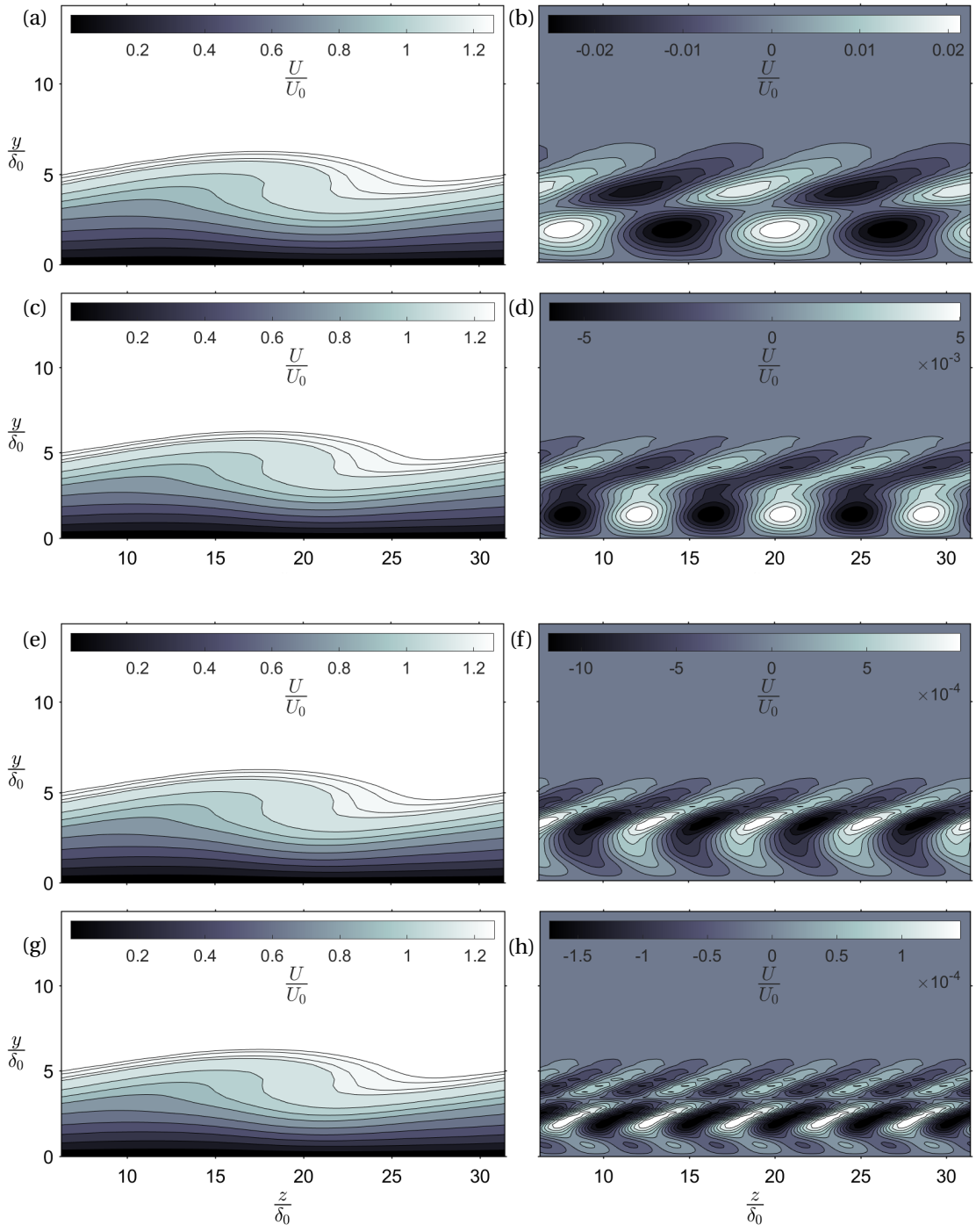

Figure C.4: U-velocity contours at $\frac{x}{c} = 0.5227$ of the mean flow and harmonics (a) 1-2 , (c) 1-3, (r) 1-4, (g) 1-5 and the isolated effect of harmonics (b) 2, (d) 3, (f) 4, (h) 5.

C.3. Nonlinear regime

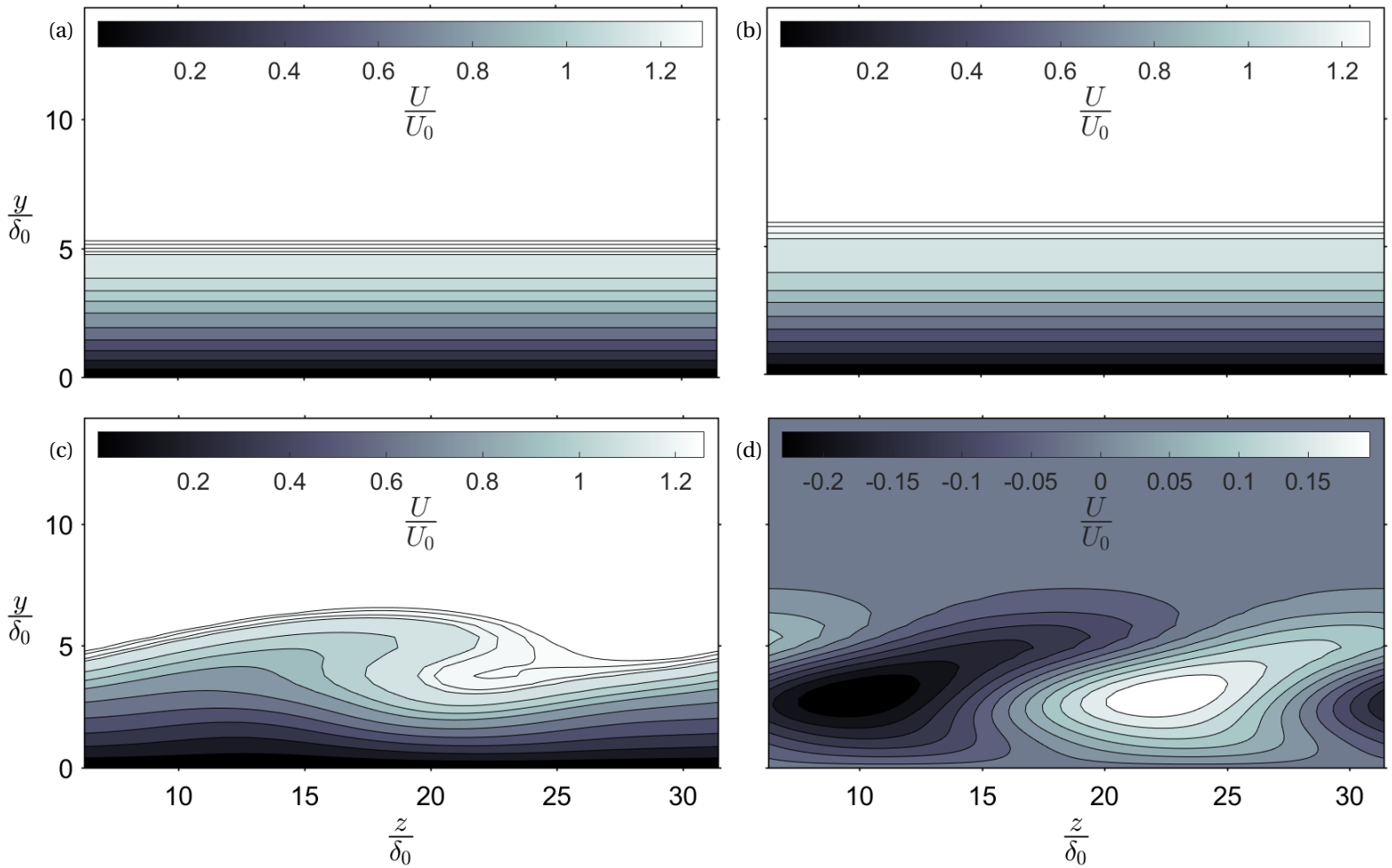

Figure C.5: U-velocity contours at $\frac{x}{c} = 0.5584$ of the (a) base flow, (b) mean flow, (c) mean flow and primary mode, (d) primary mode.

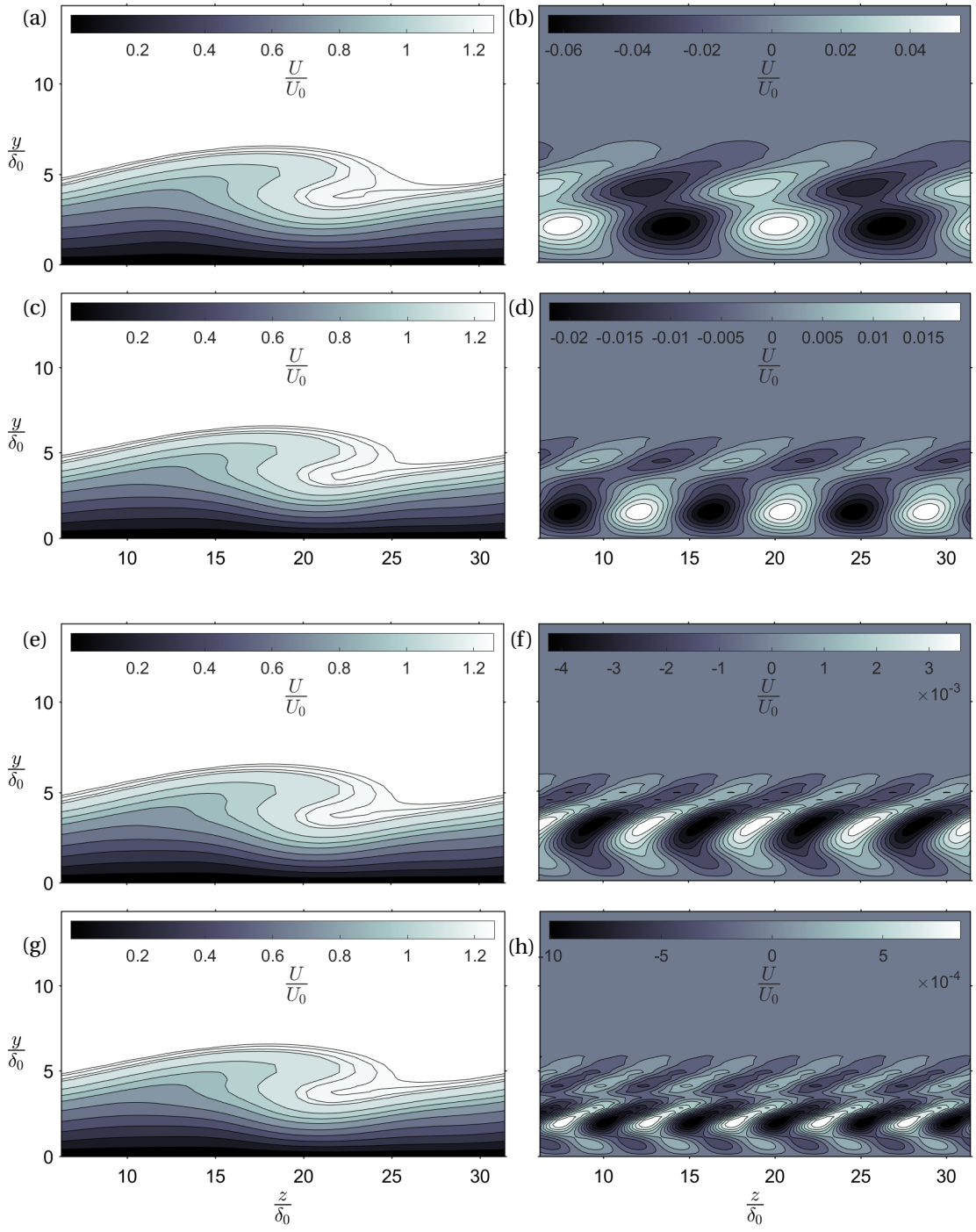

Figure C.6: U-velocity contours at $\frac{x}{c} = 0.5584$ of the mean flow and harmonics (a) 1-2 , (c) 1-3, (r) 1-4, (g) 1-5 and the isolated effect of harmonics (b) 2, (d) 3, (f) 4, (h) 5.

C.4. Far Nonlinear regime

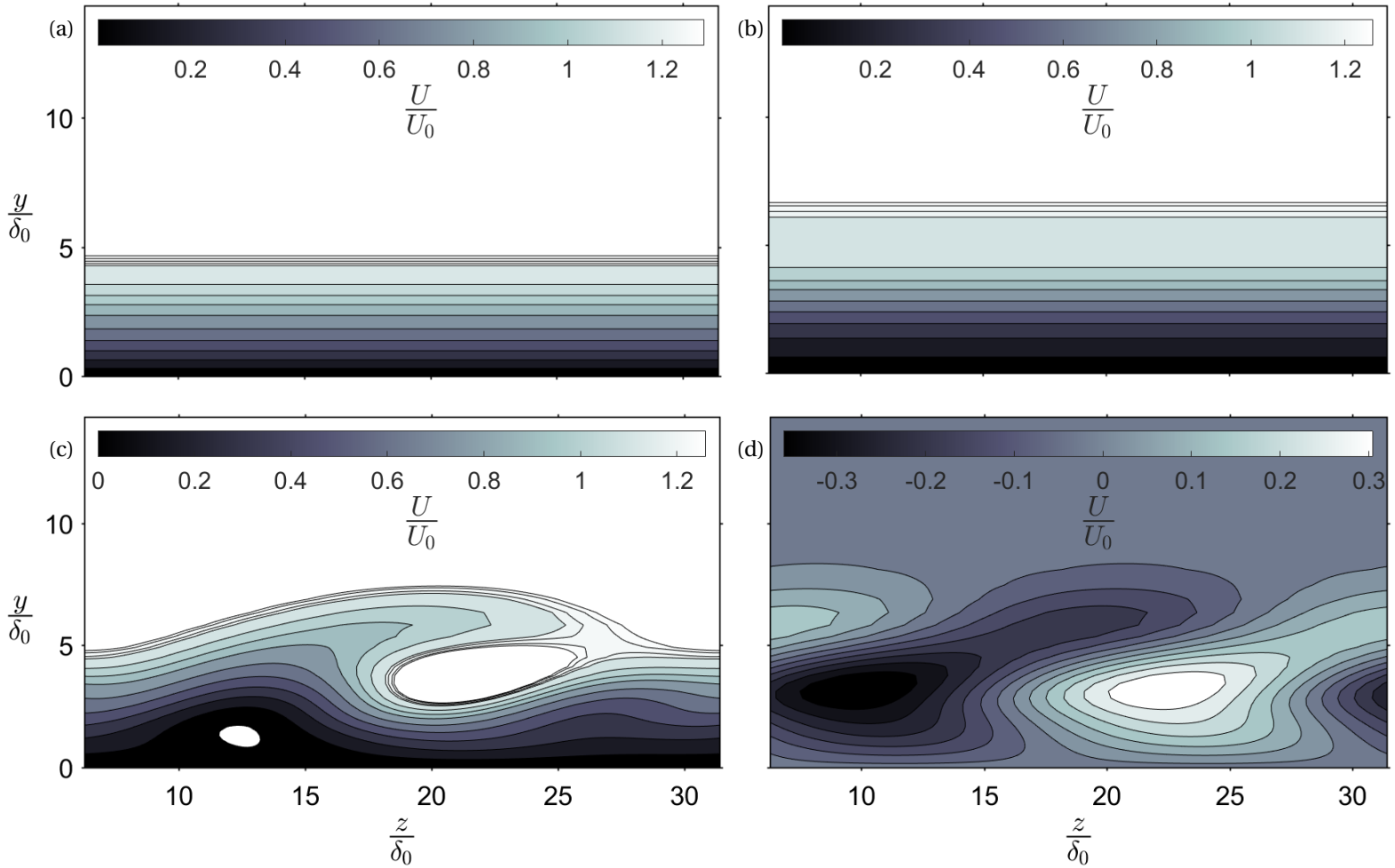

Figure C.7: U-velocity contours at $\frac{x}{c} = 0.6324$ of the (a) base flow, (b) mean flow, (c) mean flow and primary mode, (d) primary mode.

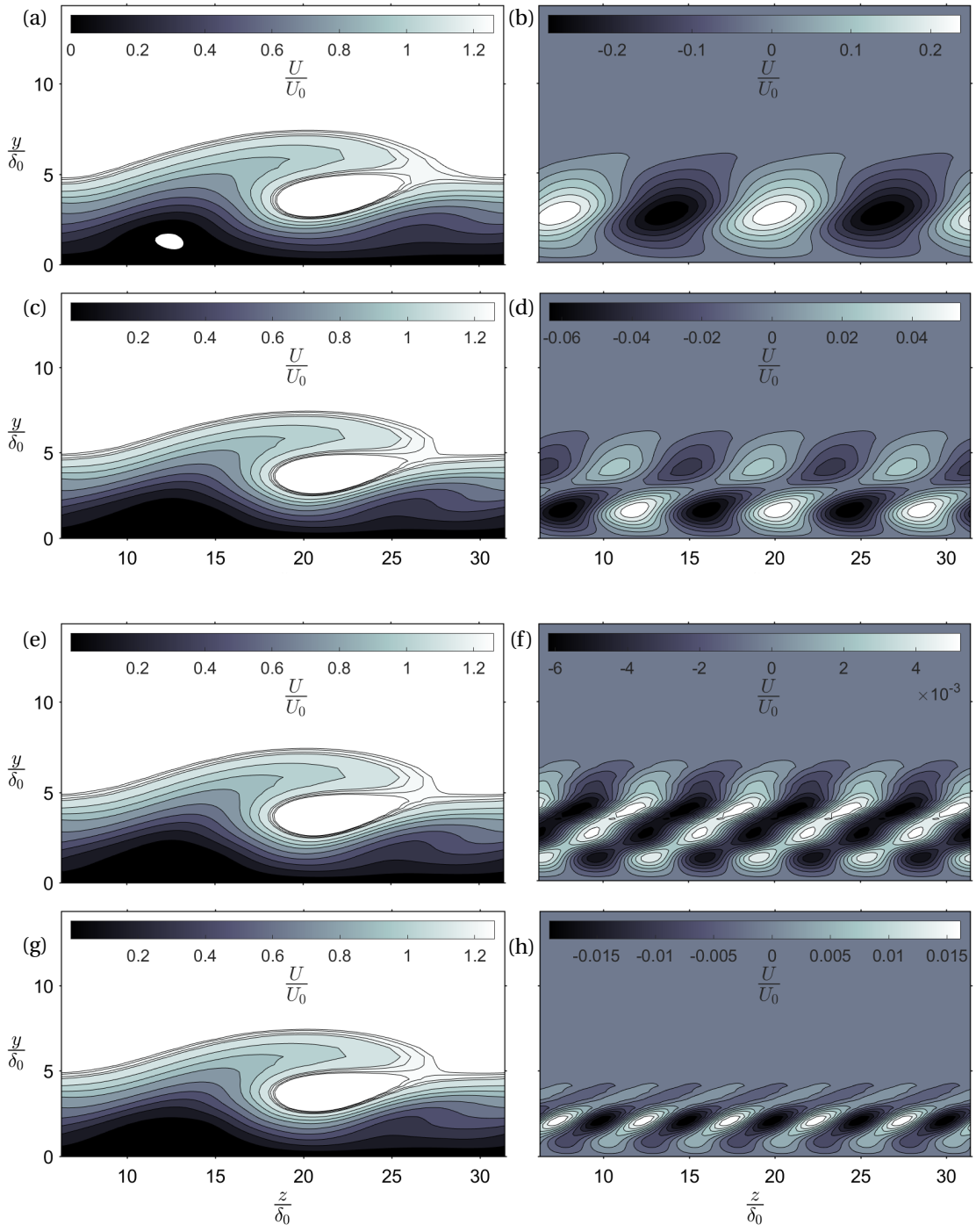

Figure C.8: U-velocity contours at $\frac{x}{c} = 0.6324$ of the mean flow and harmonics (a) 1-2 , (c) 1-3, (r) 1-4, (g) 1-5 and the isolated effect of harmonics (b) 2, (d) 3, (f) 4, (h) 5.